GAP-2007-128

Bergische Universität Wuppertal

Study of the performance of the Pierre Auger Observatory and search for primary cosmic ray photons

Viviana Scherini
PhD Thesis
26 November 2007

al nonno Aldo
ci vediamo al passo dello Stelvio

Abstract

Astroparticle physics is now entering the very exciting phase in which the efforts to enhance the detection capabilities of our instruments begin to turn out into clear answers. In this context the Pierre Auger Observatory (PAO) has been conceived to study the extensive air showers produced by the primary cosmic rays at energies above 10^{18} eV in their interaction with the Earth's atmosphere, in order to solve the mystery of the origin and nature of the highest energy particles.

The PAO design combines the most advanced detection techniques and the largest exposure, to provide high data quality together with unprecedented statistics. In addition, two experimental sites, one nearly completed in the southern hemisphere and the other to be built in the northern one will achieve full sky coverage, and the largest exposure ever.

The PAO collaboration benefits from the contribution of about 300 scientists from 17 countries. The Wuppertal group is highly involved in physics analysis and the study and monitoring of the detector performance. Moreover its tasks involve hardware development and testing. More than half of the 11 000 optical modules for the fluorescence detector telescopes have been qualified with a highly automatised test setup. Details on the experimental requirements and test results are presented in Section 4.3, (see [24]).

The performance of the fluorescence detector (FD) reconstruction algorithm has been studied at different selection levels with dedicated simulations. In Chapter 5 the FD trigger efficiency and the geometry resolutions are calculated. A realistic estimate of the hybrid resolution of the physics observables (depth of shower maximum and energy) is also given, see [108]. This work includes the extension of the reconstruction capabilities to the highest energies covered by the FD dynamic range [136].

Discrimination of different primaries is based on their expected shower features, for instance the depth shower maximum, X_{max} . In Chapter 6 the composition sensitivity of other parameters connected to the shape of the longitudinal shower profile is evaluated in order to achieve an enhancement of the separation power between photon and hadron primaries [139].

No claim for photon observation at the highest energies has been reported so far. For this work an update of the first limit to the fraction of photons in cosmic rays above 10 EeV [119], based on the measurement of X_{max} has been performed, see Section 7.2, reported in [21]. Finally, limits above 2, 3.16, 5 and 10 EeV are derived using the Pierre Auger hybrid data sample Jan 2004–July 2007, see Section 7.3. The expected impact of a photon contamination of this order on the measurement of the inelastic proton-air cross section is briefly discussed in Section 7.4.

Our limits confirm the ones derived by ground-based experiments at higher energies and they strongly constrain the non-acceleration models invoked to explain the origin of the ultra high energy cosmic rays, thus favoring astrophysical scenarios.

recuerde, la vida es color de rosa
el cielo es azul
y el espacio esta lleno de luz

Aterciopelados

Contents

1 UHECR physics 1
1.1 Introduction . . . 1
1.2 Energy spectrum and composition . . . 2
1.3 Origin of UHECR . . . 4
1.3.1 Astrophysical sources . . . 4
1.3.2 Fermi acceleration . . . 6
1.3.3 Alternative models: top-down models and Z-bursts . . . 8
1.4 Propagation . . . 10
1.4.1 Effects of the magnetic fields . . . 10
1.4.2 Energy losses and GZK process . . . 11
1.4.3 Lorentz invariance violation . . . 15

2 UHECR detection 17
2.1 Physics of extensive air showers . . . 18
2.2 Photons as EAS primaries . . . 20
2.2.1 The Landau-Pomeranchuk-Migdal effect . . . 21
2.2.2 The preshower effect . . . 21
2.2.3 Photonuclear cross section . . . 22
2.3 EAS detection techniques . . . 23
2.3.1 Fluorescence telescopes . . . 23
2.3.2 Surface detector arrays . . . 25
2.3.3 Radio and acoustic detection . . . 26

3 Overview of experimental results 29
3.1 Spectrum and composition . . . 30
3.2 Limits to photons and neutrinos . . . 34
3.3 Inelastic proton-air cross section . . . 35
3.4 Anisotropy studies . . . 36

4 The Pierre Auger Observatory 39
4.1 The Pierre Auger Observatory: a hybrid detector . . . 39
4.1.1 The surface array (SD) . . . 40
4.1.2 The fluorescence detector (FD) . . . 42
4.1.3 Atmospheric models and monitoring devices . . . 45
4.2 Details of the hybrid reconstruction . . . 48
4.3 Photomultipliers qualification tests . . . 52

5 Performance of the Fluorescence Detector reconstruction algorithm 57
5.1 Generation parameters 58
5.2 Trigger efficiency 59
5.3 Monocular geometry resolution 61
5.4 X_{max} and energy resolution 61
5.5 Extension to the highest energies 66
  5.5.1 Saturation in the high gain channel 66
  5.5.2 Saturation recovery 70
  5.5.3 Treatment of light collection inhomogeneities 72
  5.5.4 Impact of quality cuts 74

6 Simulation study of shower profiles from ultra-high energy cosmic rays 77
6.1 Composition sensitivity of the shower profile 78
  6.1.1 CORSIKA profile and Gaisser-Hillas fit 79
  6.1.2 Other trial functions and PCA analysis 80
6.2 Separation power after full detector simulation 83

7 Upper limit to the photon fraction in cosmic rays 87
7.1 Deriving an upper limit 88
  7.1.1 Small data sample: probabilistic method 88
  7.1.2 Large data sample: statistical method 89
  7.1.3 General considerations on the derived limits 90
  7.1.4 Acceptance correction 91
7.2 Update of the hybrid limit above 10 EeV 92
  7.2.1 Data sample 92
  7.2.2 Reconstruction requirements 93
  7.2.3 Photon candidate distributions 94
7.3 Upper limit above 2 EeV 96
  7.3.1 Detector efficiency study 96
  7.3.2 Photon candidates 97
  7.3.3 Conclusions: upper limits above 2, 3.16, 5, and 10 EeV 105
7.4 Impact of a photon contamination on the measurement of the p-air inelastic cross section 106

Summary and outlook 109

Appendices

A Fluorescence detector electronics: the virtual channel 113
A.1 The virtual channel working principle 113
A.2 Implementation in the simulation-reconstruction framework 114

B Cuts and candidates 117

Bibliography 123

Chapter 1

UHECR physics

1.1 Introduction

Soon after their discovery by V. Hess in 1912 [73], cosmic ray have assumed a leading role in astronomy and elementary particle physics. The systematic study of reactions induced by cosmic radiation, lead for instance to the discovery of the positron, the muon and the pion.

Moreover, we can consider cosmic rays as messengers from the Galaxy and beyond, leading our way to the understanding of the Universe. Especially the ultra-high energy cosmic rays (UHECR), at energies above 10^{18} eV, could open a new challenging window for astronomy, as they should point back directly to their production sites. In addiction, at energies not reachable in man-made accelerators, they could represent an alternative to extend our knowledge of fundamental interaction physics.

The existence of events above 10^{20} eV has been established in different experiments since the first observation by Linsley in his pioneering work of 1966 [95]. The nature and origin of these particles is instead still unknown, no astrophysical object has yet been clearly identified as a source.

Progress has been made in understanding the mechanisms which could lead to the acceleration at these extraordinary energies. Models of the cosmic rays propagation, including the effects of interaction with the background radiation and the influence of Galactic and extragalactic magnetic fields, have been successfully developed. Alternative new physics scenarios invoking the decay or annihilation of exotic particles, or violation of Lorentz invariance, have been also proposed and can be experimentally tested.

1.2 Energy spectrum and composition

To understand the origin and nature of the highest energy cosmic rays we begin with the analysis of their overall energy spectrum. The cosmic ray spectrum extends over 11 decades in energy with a flux which follows a power law $E^{-\alpha}$ and spans more than 30 orders of magnitude.

The flux falls, at a rate of about 3 orders of magnitude per energy decade, from about one particle per m^2 per second at around 100 GeV to one particle per km^2 per year above 10 EeV. Fig. 1.1 shows the all-particle differential energy spectrum, i.e. number of particles per m^2 sr s GeV, from [45]. At low energies the index α is about $2.6 \div 2.7$. At energies around $3 \cdot 10^{15}$ eV the first feature, the so called *knee*, shows up with a steepening of the spectrum described by an index ~ 3. A further steepening, the *second knee*, at an energy of $\sim 5 \cdot 10^{17}$ eV, with index ~ 3.3 is reported in [32][101]. At energies of $\sim 10^{19}$ eV, the so called *ankle*, a very pronounced flattening, with index ~ 2.7, appears [1].

While, up to these energies, cosmic rays are believed to be mainly of Galactic origin, the interpretation of the ankle is that a new population of CRs with extragalactic origin begins to dominate the more steeply falling Galactic population. However, the description of this transition is model dependent and high quality experimental data are still needed in order to discriminate among different scenarios.

For a complete review of the observation and theoretical models for the interpretation of the knee see [79]. Regarding the highest energy range, we recall briefly two different interpretations of the transition region of the spectrum, between the knee and the ankle, with the consequent predictions on the cosmic rays composition.

The standard model for the origin of cosmic rays is based on the assumption that Galactic cosmic rays are accelerated in young supernovae remnants (SNR). Since the maximum energy achievable depends on the rigidity of the particles, this model predicts that the different components will have a spectrum with a cutoff at an energy proportional to charge. Based on this assumption and the observation of the proton knee, the end of the Galactic spectrum is estimated at $5 \div 8 \cdot 10^{16}$ eV, the cutoff energy for iron.

If the extragalactic component becomes dominant only at the ankle, an additional acceleration mechanism must be introduced to account for the energies above that limit. In this energy region, the composition must be dominated by heavy nuclei.

The standard interpretation for the ankle is that the flat extragalactic component crosses the steep Galactic spectrum, generating this feature just above the intersection energies, see for instance [75]. The spectrum of the extragalactic component is consistent with the slope originating from acceleration in strong or ultra relativistic shocks. The main problem is to explain a predominantly heavy composition up to 10^{19} eV. A model invoking an extragalactic component with mixed composition could then be the favored solution [3].

An alternative and appealing explanation, the pair production dip model, has been very recently proposed [5], based on the predictions reported in [29]. Assuming an extragalactic proton component, the dip is obtained naturally from the interaction with the cosmic microwave background (e^+e^- pair production). The transition to the extragalactic component is expected to occur at lower energies, at around 10^{18} eV (second knee), and the composition to be proton dominated in this range.

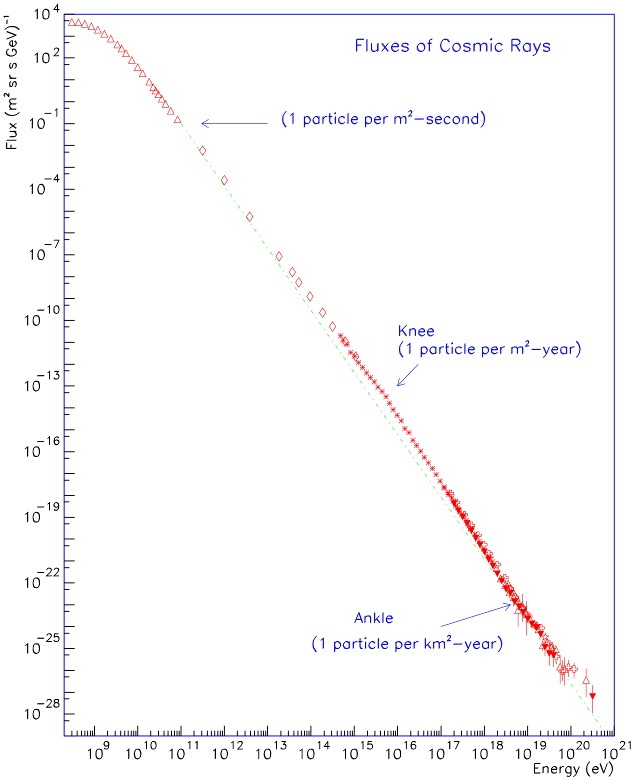

Figure 1.1: Differential energy spectrum of cosmic rays. Approximate integral fluxes are indicated: one particle per m^2 second at $\sim$ 100 GeV, one particle per m^2 year at the knee ($\sim 3 \cdot 10^{15}$ eV), and one particle per km^2 year at the ankle ($\sim 5 \cdot 10^{18}$ eV). From [45].

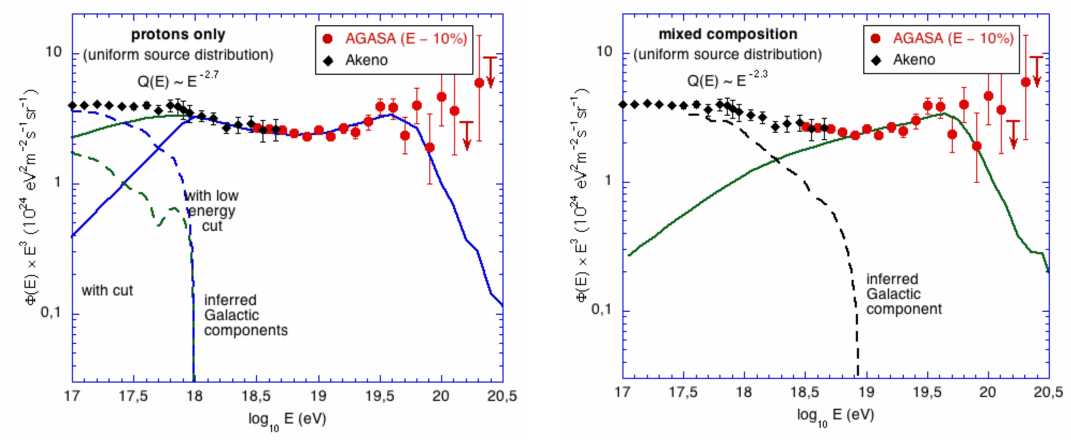

Figure 1.2: Cosmic rays flux $\times E^3$ for the two most favored models of the dip-ankle interpretation, (left) dip-model assuming pure proton composition [5] and (right) extragalactic component with mixed composition [3], compared to data from Akeno [100] and AGASA [146].

1.3 Origin of UHECR

The question on the possible sources of the ultra high energy cosmic rays is one of the most challenging in the astroparticle field. On the theory side, models have been proposed to solve this question. We will briefly summarise here the three possible scenarios: the astrophysical acceleration (bottom-up), the non-acceleration (top-down) and a hybrid combination of the previous two.
On the experimental side searches for signifcant anisotropies in arrival directions of UHE cosmic rays have been made in many experiments, both on large and small angular scales. The arrival direction distribution is found to be rather isotropic over a broad energy range. An excess from the Galactic center, and clustering of events at small angles suggesting correlations with astrophysical objects like for instance BL Lacs, have been claimed but still wait for confirmation. The ongoing searches from the Pierre Auger Observatory [124] are expected to give soon unambiguous answers.

1.3.1 Astrophysical sources

As pointed out in Section 1.2 the regular shape of the spectrum over its wide energy range may suggest a common acceleration mechanism, which could take place in different astrophysical sources. Many models and sources have been proposed, which could accelerate charged particles, hadrons especially, up to the extremely high energies, but none of them is yet experimentally confirmed.
Knowing the differential flux it is possible to estimate the energy density in cosmic rays. Integrating the flux over energy and assuming an isotropic and uniform distribution in space, the energy density is $\rho_{cr} \simeq 1$ eV cm^{-3}, comparable with starlight (~ 0.6 eV cm^{-3}) and magnetic field energy density (~ 0.3 eV cm^{-3}). To keep up with this, the Galactic sources must pump $V_G \rho_{cr}/\tau \sim 10^{41}$erg/s, where V_G is the Galactic volume and $\tau \sim 10^6$ years is the confinement time in the Galaxy. This value is comparable with the kinetic energy release in supernovae explosions. We obtain about the same required power to keep up with the flux at the highest energies, with densities of the order 10^{-8} eV cm^{-3} calculated over the volume of the local super-cluster and an escape time of 10^8 years.
There are basically two kinds of acceleration mechanisms considered in connection with CR acceleration: the direct acceleration of charged particles by electromotive force (emf) and the stochastic acceleration in a magnetized plasma (Fermi acceleration). For a review of the conventional acceleration scenarios see [8][36].
While for the case of the direct acceleration the emf is associated with compact objects like rotating neutron stars, the statistical acceleration applies to the case of moving magnetized plasma. Both of the models must face the problem of fitting the power law spectrum and having to provide the required power overcoming energy losses.
The maximum energy of a particle being accelerated can be estimated by requiring that the gyro-radius is contained in the acceleration region. We then have:

$$\left(\frac{E_{max}}{\text{EeV}}\right) = \frac{1}{2} Z \beta \left(\frac{B}{\mu\text{G}}\right) \left(\frac{R}{\text{kpc}}\right) , \tag{1.1}$$

where Z is the charge of the particle B is the magnetic field strength and R the size of the accelerating region. This holds for strong shocks and very inclined B with respect

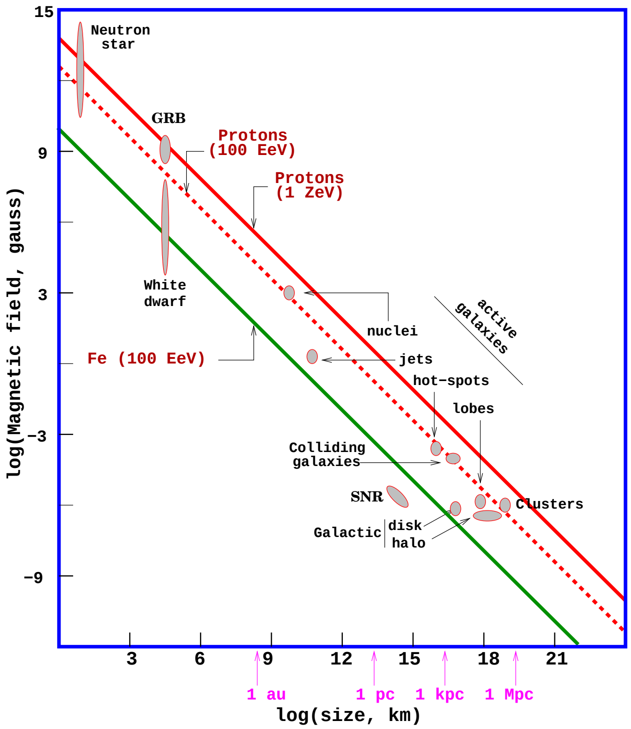

Figure 1.3: Hillas plot: size and magnetic field strength of possible astronomical objects which could be particle source and acceleration candidates. Objects below the diagonal lines cannot accelerate particles to the indicated energies. From [8].

to the shock normal, and for relativistic particles. The condition also applies to direct acceleration scenarios, as for neutron stars, in which the emf is connected to a rapidly moving magnetic field.

Fig. 1.3 shows that to achieve a given maximum energy, one must have acceleration sites that have either a large magnetic field or a large size of the acceleration region. Only a few astrophysical sources connected with active galaxies and hot spots of radio-galaxies, gamma ray bursts and compact objects like neutron stars, seem to satisfy the conditions necessary for acceleration of protons up to 10^{20} eV (red dashed line). The characteristics of these objects are summarised below.

- *Active Galactic Nuclei (AGN):* AGN are one of the most favored sources for cosmic rays at the highest energies [74][127]. AGNs are powered by the accretion of matter onto a supermassive black hole of $10^6 \div 10^8$ solar masses. Typical values in the central engine are R$\sim 10^{-2}$ pc, and B$\sim$ 5 G, which make possible the containment of protons up to 10^{20} eV. The main problem here is the large energy loss in a region of high field density, which would limit the maximum energy achievable for protons and forbid the escape for heavy nuclei. Neutrons could eventually escape the central region and then decay to protons with maximum energy around 10^{18} eV. Another solution is that the acceleration occurs in AGN jets where particles are injected with Lorentz factors larger than 10, and where energy losses are less significant.

- *Radio-galaxies hot spots:* Fanaroff-Riley II galaxies are the largest known dissipative objects (non-thermal sources) in the Universe. Jets from the central black-hole of an active galaxy end at a termination shock where the interaction of the jet with the intergalactic medium forms radio lobes and localized regions of intense synchrotron emission, known as "hot spots". For typical hot-spot conditions B $\sim 300\ \mu$G and $\beta \sim 0.3$. Assuming that the magnetic field of the hot spot is limited to the observable region (~ 1 pc), one obtains E$_{max} < 5 \cdot 10^{20}$eV.
- *Clusters of galaxies:* galaxy clusters are reasonable sites to consider for ultra-high energy cosmic rays acceleration, since particles with energy up to 10^{20} eV can be contained by cluster fields ($\sim 5\mu$G) in a region of size up to 500 kpc. However, losses due to interactions with the microwave background during the propagation inside the clusters limit UHECRs in cluster shocks to reach at most 10 EeV.
- *Gamma Ray Bursts (GRBs):* collapse of massive stars or mergers of black holes or neutron stars could explain the origin of the detected bursts of gamma rays up to GeV energies. The observed gamma-rays are emitted by relativistic electrons via synchrotron radiation and inverse Compton scattering. Acceleration of electrons and protons to the highest energies is then necessary. The duration of the detected GRB signal extends over 5 orders of magnitude ($10^{-3} \div 10^{2}$ s) with an energy release up to 10^{51} erg/s. This is consistent with the luminosity required for cosmic rays above 10^{19} eV, but the large estimated GRBs distances (up to z=5) cannot account easily for the UHECR flux.
- *neutron stars:* for direct acceleration in compact objects, for example in rotating neutron stars or pulsars, the relation 1.1 becomes E$_{max} = \omega/cZB_s {r_{ns}}^2$, where ω is the pulsar angular velocity, B$_s$ the surface magnetic field and r$_{ns}$ the neutron star radius. If B$_s \sim 10^{12}$ G, r$_{ns} \sim 10$ km, and $\omega \sim 200$ Hz (values refer to the Crab pulsar), this is equivalent to an electromagnetic force of $\sim 10^{18}$ V.

1.3.2 Fermi acceleration

In 1949 Fermi proposed an efficient mechanism to accelerate relativistic particles through their interaction with moving magnetized gas clouds [57]. The original theory can be adapted to the case of shock accelerations in astrophysical objects, where the required extremely high energies could be possibly reached.

In Fig. 1.4, left panel, a sketch of the process occurring in moving magnetized cloud is shown. A particle of energy E_1 and momentum p_i enters a massive moving gas cloud with angle θ_1 with respect to the cloud velocity V, and scatters on its magnetic irregularities. In the rest frame of the cloud there's no change in energy, as the particle scatters collision-less on the magnetic field moving with the cloud. The net energy gain is obtained applying the Lorentz transformations between the laboratory frame and the cloud frame (primed). In the cloud frame the particle energy is:

$$E_1^{'} = \gamma\ E_1(1 - \beta \cos\theta_1)\ , \tag{1.2}$$

where $\beta = V/c$ and γ refer to the cloud. In the laboratory frame the particle energy after escaping the cloud is:

$$E_2 = \gamma E_2^{'}(1 + \beta \cos\theta_2^{'})\ . \tag{1.3}$$

Since $E_2^{'} = E_1^{'}$ and substituting 1.2 in 1.3 the relative energy change in the laboratory frame results:

$$\frac{\Delta E}{E} = \frac{E_2 - E_1}{E_1} = \frac{1 - \beta\cos\theta_1 + \beta\cos\theta_2^{'} - \beta^2\cos\theta_1\cos\theta_2^{'}}{1-\beta^2} - 1 \ . \tag{1.4}$$

Due to the random nature of the scattering occurring in the cloud, the average value of $\cos\theta_2^{'}$ is zero. The collision probability depends on the relative velocity of the cosmic ray particle with respect to the moving cloud. Since $\beta \ll 1$, averaging on the solid angle we have $< \cos\theta_1 >= -\beta/3$, which, substituted in 1.4 gives:

$$\frac{\Delta E}{E} = \frac{E_2 - E_1}{E_1} = \frac{1 + \frac{1}{3}\beta^2}{1-\beta^2} - 1 \simeq \frac{4}{3}\beta^2 \ . \tag{1.5}$$

The average energy change is thus positive, but small since it is of the second order in β (and $\beta \ll 1$).

A more efficient acceleration, of the first order in β, is thought to take place in regions of strong shocks, as for example in supernovae and AGN jets. During a supernova explosion several solar masses of material are ejected at a speed $V_p \sim 10^4$ km/s, i.e. much faster than the speed of sound in the interstellar medium (ISM) which is 10 km/s. A strong shock wave propagates then radially through the ISM. The shock velocity V_s depends on the velocity V_p of the material ejected, and on the compression ratio R as $V_s = R/(R-1)V_p$. In Fig. 1.4, right panel, a sketch of the process is shown. A cosmic ray particle is scattered in the magnetic irregularities of the ISM and eventually crosses the shock front. Independently on which side of the shock the particle is, the plasma on the other side is approaching it at speed V_p. So that at each crossing of the front there is a net energy gain, and the process is more efficient.

The average value of $\cos\theta_2^{'}$ is now 2/3 determined from the probability of a crossing the shock from downstream to upstream. The same motivation gives an average value of -2/3 for $\cos\theta_1$ (crossing from upstream to downstream). Substituting in 1.4 we have then:

$$\frac{E_2 - E_1}{E_1} = \frac{1 + \frac{4}{3}\beta + \frac{4}{9}\beta^2}{1-\beta^2} - 1 \simeq \frac{4}{3}\beta \ , \tag{1.6}$$

which is now of the first order in $\beta = V_p/c$.

The probability for a particle to be lost downstream is $P_{loss} = \rho_{cr}\ V_s/R$, where V_s/R is the velocity of the particles flowing away downstream in the rest frame of the shock. The probability for a relativistic particle moving with speed v, to cross the shock is instead

$$P_{cross} = \rho_{cr}\frac{1}{2}\int_{-V_s/v}^{1} (V_s + v\cos\theta)\ \mathrm{d}(\cos\theta) \ \simeq \ \rho_{cr}\frac{v}{4} \ . \tag{1.7}$$

The probability to escape from the acceleration region is then obtained dividing Eq. 1.6 by Eq. 1.7, thus $P_{esc} \approx 4V_s/Rv$. Given P_{esc}, we can derive the number of particles which may be accelerated to an energy above E. This is in general proportional to the probability for the particle to remain in the region after n cycles:

$$N(\geq E) \propto (1 - \mathrm{P_{esc}})^n \ , \tag{1.8}$$

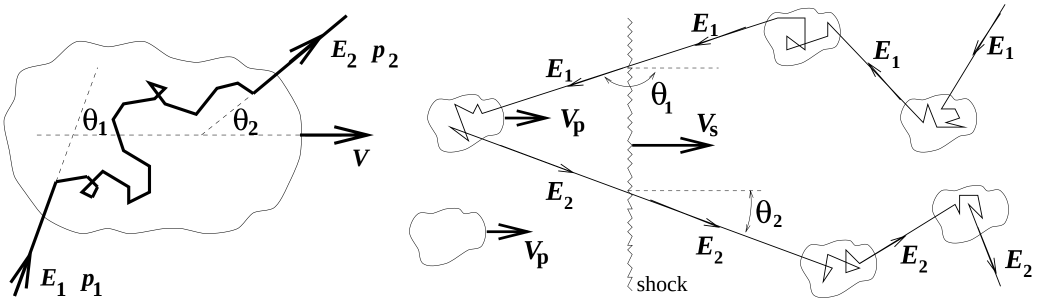

Figure 1.4: Left: sketch of the second order Fermi acceleration mechanism occurring in a moving magnetized cloud. Right: first order Fermi acceleration occurring in strong plane shocks. From [126].

After each acceleration cycle the particle acquires an amount of energy proportional to the initial energy E_0. The energy obtained after n collisions is:

$$E = E_0(1+\zeta)^n \ , \tag{1.9}$$

where ζ is the relative energy gain factor $\Delta E/E$. The number n of cycles to reach an energy E is thus

$$n = \frac{\ln(E/E_0)}{\ln(1+\zeta)} \ . \tag{1.10}$$

Solving Eq. 1.8 in logarithm gives then:

$$\ln N(\geq E) = A + \frac{\ln{(E/E_0)}}{\ln(1+\zeta)} \ \ln(1-\mathrm{P_{esc}}) = B - (\alpha - 1) \ \ln E \ , \tag{1.11}$$

where

$$\alpha = 1 - \frac{\ln{(1-\mathrm{P_{esc}})}}{\ln(1+\zeta)} \approx \frac{R+2}{R-1} \ . \tag{1.12}$$

Thus we naturally obtain an integral energy spectrum described by a power law, with index $-(\alpha-1)$, and for the differential spectrum an index $-\alpha$, which for the strong shock case (R=4) gives E^{-2}. The second important consequence is that the maximum achievable energy depends on the time spent in the acceleration region. After the time t, the particle reaches an energy of:

$$E \leq E_0(1+\zeta)^{(t/\mathrm{T_{esc}})} \ . \tag{1.13}$$

1.3.3 Alternative models: top-down models and Z-bursts

An alternative to acceleration models, introduced to explain the highest energy cosmic rays, are the so called *top-down models*, which involve the decay or annihilation of exotic particles. These so called X-particles, basically decay in quarks and leptons. The quarks produce jets of hadron, mainly pions and a few percent of nucleons. The pions decay then to photons, muons, neutrinos (anti neutrinos) and electrons (positrons).

The general characteristic of these models is a photon domination of the spectrum at the highest energies. The spectra of the produced CR are determined by the physics of QCD

fragmentation, and they are expected to be harder than obtained in the astrophysical scenarios.
In order to detect the produced EHECR, the X-particle must be super-massive ($> 10^{11}$ GeV). The density and the rate of decay must be large enough to account for an observable cosmic rays flux. Moreover, to avoid energy loss during the propagation from the source, the decays must take place within a limited distance (~ 100 Mpc).
We recall here briefly the super-heavy dark matter model (SHDM), and the Topological Defect model (TD). For a detailed review see [31].

- *TD:* the Grand Unification Theory predicts, in the early stage of the Universe evolution, the formation of topological defects like magnetic monopoles, strings, cosmic necklaces and domain walls, as a result of symmetry breaking phase transitions. The TDs can be thought of being constituted by a trapped super-massive X-particle which then decays to his constituent fields. Super heavy gauge and higgs bosons, decay into jets of hadrons, mostly pions. Pions in the jets subsequently decay into photons, electrons, and neutrinos. The highest energies are not a challenge for these models, since the symmetry breaking scales are typically 10^{21} eV and the typical X-particle masses are between 10^{22} and 10^{25} eV. Some tuning of the rate of X-particle production is instead required to fit the observed UHECR flux without conflicting with the diffuse gamma ray flux observed at lower energies.

- *SHDM:* in this scenario super heavy metastable relic particles (MSRP), as the so called cryptons or the wimpzillas, were produced in the early stages of the Universe, and now form a significant part of the cold dark matter clustering in the galaxy halos. The contribution to the UHECR would be dominated by the clustering in the halo of our Galaxy. A signature of these models would then be a clear excess of UHECR events from the galactic center.

In the *Z-burst model* ultra-high energy (UHE) neutrinos coming from remote sources annihilate at the Z-resonance with relic background neutrinos. The Z bosons then decay,

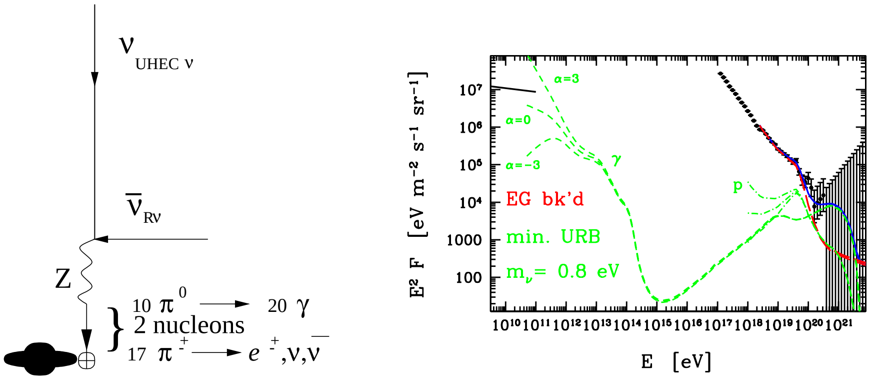

Figure 1.5: Left: sketch of the Z-burst process resulting from the resonant annihilation of a EHE energy cosmic neutrino on a relic (anti-)neutrino. Right: the available UHECR data and the best fit from Z-bursts. From [59].

producing secondary protons, neutrinos and photons as sketched in Fig. 1.5. The Z-resonance occurs when the energy of the incoming neutrino, in the rest frame of the relic neutrino, is

$$E_{res} = \frac{m_Z^2}{2m_\nu} = 4 \cdot 10^{21} eV (\frac{eV}{m_\nu}) \tag{1.14}$$

As pointed out in [59] no astrophysical source is yet known to meet the requirements for the Z-burst hypothesis. Especially no extremely high energy photons should be produced at the source together with the UHECR neutrinos, otherwise too many low energy photons are predicted. Current limits top the neutrino flux in the energy range $10^{21} \div 10^{23}$ are also strongly constraining this scenario, see for instance [67].

1.4 Propagation

1.4.1 Effects of the magnetic fields

During propagation from their sources to the Earth, cosmic rays are deflected by magnetic fields. The field intensity is determined measuring the rotation of the polarization plane of the radiation emitted from extragalactic sources like pulsars or radio sources. A regular intergalactic field is strongly constrained to values lower than 10^{-9} G. Galaxy cluster may have a stronger field coherent on the Mpc scale.

The magnetic field in our Galaxy is known to have a regular large scale structure. The typical value of the galactic magnetic field is a few μG, approximately uniform over scales of the order of a few kpc. The magnetic field lines follow the spiral arms. Different models are built depending on the sign of the field in the arms and on the symmetry with respect to the galactic plane.

In Fig. 1.6 the trajectories of nuclei with E/Z = 1 (solid lines) and 10 EeV (dotted lines) in the BSS-S galactic magnetic field model, are sketched, from [70]. Dashed lines indicate the spiral arms. At rigidity of the order 1 EeV the nuclei are trapped in the spiral structure of the magnetic fields and follow helicoidal trajectories around the galactic field lines.

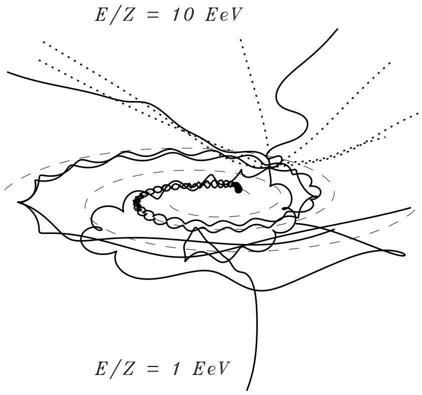

Figure 1.6: Examples of trajectories of nuclei with E/Z = 1 EeV (solid lines) and 10 EeV (dotted lines) in the galactic magnetic fields (BSS-S model) from [70].

The gyro-radius, for a proton at 1 EeV in a field of ∼ 3μG is about 300 pc, namely the thickness of the Galactic disc. The motion of nuclei with rigidity E/Z above 10 EeV is instead not significantly affected by the magnetic field since the gyro-radius for a particle of that energy is of the same order as the traveled distance. In this case the information on the incoming direction is conserved and the correlation with sources can in principle be established.

The key quantity to determine the angular deflection from the incoming cosmic ray path, as a function of the traveled distance and primary energy, is the particle Larmor radius, $\mathrm{r}_L \simeq E/(Z \cdot B_\perp)$. Where Z is the charge of the particle and $B_\perp$ is the magnetic field component perpendicular to the particle momentum.

If the magnetic field is constant over the traveled distance d, we have:

$$d\theta(E,d) \simeq \frac{d}{r_L} \simeq 0.52^\circ \cdot \mathrm{Z} \cdot \left(\frac{E}{10^{20}\ \mathrm{eV}}\right)^{-1} \cdot \left(\frac{B}{10^{-9}\ \mathrm{G}}\right) \cdot \left(\frac{d}{\mathrm{Mpc}}\right) \quad . \tag{1.15}$$

This means a deviation of less than 1° for a proton of energy ∼ 10^{20}eV in a magnetic field of ∼ μG on a distance ∼ kpc, or equivalently with field ∼ nG over a distance of the order of the Mpc. In the realistic case the coherence length and spread of the magnetic fields must be taken into account. We then have:

$$d\theta(E,d) \simeq 0.8^\circ \cdot \mathrm{Z} \cdot \left(\frac{E}{10^{20}\ \mathrm{eV}}\right)^{-1} \cdot \left(\frac{B}{10^{-9}\ \mathrm{G}}\right) \cdot \left(\frac{d}{10\mathrm{Mpc}}\right)^{1/2} \cdot \left(\frac{\lambda}{\mathrm{Mpc}}\right)^{1/2} \quad . \tag{1.16}$$

An average time delay, with respect to linear propagation, proportional to $d\theta(E)^2$ is expected. For an analytical treatment see [31] and [158].

1.4.2 Energy losses and GZK process

At the highest cosmic ray energies, not only the propagation through the intergalactic magnetic fields, but also the interactions of primaries with the background radiation fields like the cosmic microwave background (CMB), infrared background (IR) and radio background (RB), must be taken into account. After the discovery of the CMB by Penzias and Wilson [107], Greisen [69], Zatsepin and Kuz'min [162] predicted that, due to photopion production on the CMB, the spectrum of cosmic rays protons would show a cutoff at about $5 \cdot 10^{19}$eV. The main involved processes for protons in this energy range are the following:

$$\begin{aligned} p + \gamma_{CMB} &\rightarrow p + \pi^0 && (1.17) \\ &\rightarrow n + \pi^+ && \\ &\rightarrow p + e^+ + e^- \ . && (1.18) \end{aligned}$$

In the laboratory frame, the center of momentum energy squared is:

$$s = m_p^2 + 2\mathrm{E_p}\epsilon\,(1 - \beta\cos\theta)\ , \tag{1.19}$$

where ϵ is the energy of the photon and β is the proton speed (c=1).

The threshold energy for a proton to produce a pion on the photons of CMB in a head-on collision is:

$$E_{th} = \frac{m_\pi}{4\epsilon}(2m_p + m_\pi) \simeq 6.8 \cdot 10^{16} (\frac{\epsilon}{eV})^{-1} \text{ eV} , \tag{1.20}$$

which, dealing with average photon energies of $\sim 6 \cdot 10^{-4}$ eV, leads to $\sim 10^{20}$ eV, but can be smaller since the microwave spectrum extends to higher energies ($\sim 10^{-3}$ eV).
The energy dependence of the mean free path of the proton is:

$$\frac{1}{\lambda_{p\gamma}} = \frac{1}{8 \, \beta \, \mathrm{E}_\mathrm{p}^2} \int_{\epsilon_{th}}^{\infty} \frac{n(\epsilon)}{\epsilon^2} \, \mathrm{d}\epsilon \int_{s_{min}}^{s_{max}} (s - m_p^2) \, \sigma_{p\gamma}(s) \, \mathrm{ds} , \tag{1.21}$$

where $n(\epsilon)$ is the photon number density per energy, s_{min} and s_{max} are the squares of minimum and maximum energies in the center of mass system. The mean free path for a proton can be estimated as ≈ 8 Mpc, where $n \approx 400$ cm^{-3} is the CMB photon density, and $\sigma_{p\gamma} \approx 10^{-28}$ cm^2 is the process cross section at the threshold energy. The neutron decay length is about 1 Mpc at 10^{20} eV, so that on these length scales it decays before interacting.
The energy loss per interaction is $\sim 20\%$, thus giving an attenuation length of the order of some tenths of Mpc, beyond which the proton energy falls below the GZK threshold. This bring us to the conclusion that the sources of the highest energy observed events must be within a sphere of that size.
At lower energies the dominant process is the Bethe-Heitler pair production (Eq. 1.18) with a threshold energy, for the case of face to face collision, equal to:

$$E_{th} = \frac{m_e(m_p + m_e)}{\epsilon} \simeq 4.8 \cdot 10^{14} (\frac{\epsilon}{eV})^{-1} \text{ eV} \approx 4.8 \cdot 10^{17} \text{ eV} . \tag{1.22}$$

At higher energies this process is less significant as its inelasticity is $\sim 0.1\%$, much smaller compared to the energy loss for the pion photoproduction (Eq. 1.17). The mean free path, given a cross section of the order 10^{-25} cm^2, is in this case about ~ 1 Gpc.
At lower energies the attenuation length tends to become constant and equal to the energy loss due to the expansion of the universe, ~ 4 Gpc.
In Fig.1.7 left panel, the interaction length (dashed line) and attenuation length (thick solid line) for pion photo-production by nucleons on CMB, and estimated RB, is plotted as a function of energy. The attenuation length for pair production is also shown (thin solid line).
Nuclei of mass A undergo photo-disintegration and pair production, both on the CMB and on IR, according to the following relations:

$$\begin{aligned} A + \gamma_{CMB,IR} \rightarrow &\quad (A-1) + N \qquad (1.23) \\ \rightarrow &\quad (A-2) + 2N \qquad (1.24) \\ \rightarrow &\quad A + e^+ + e^- \end{aligned}$$

Since the energy is shared between nucleons, the threshold energy for the processes increases. The inelasticity is lower of a factor $\sim 1/A$ while the cross section increases with Z^2. This means that the loss length, in case of heavy nuclei, will be smaller (~ 1 Mpc) with respect to protons, but at a higher energy.

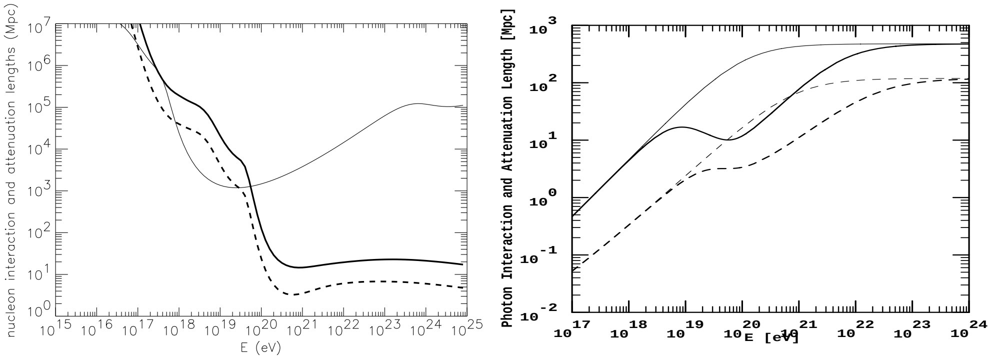

Figure 1.7: Left: nucleon interaction length (dashed line) and attenuation length (solid line) for photo-pion production, and proton attenuation length for pair production (thin solid line) in the combined CMB and estimated RB. Right: for pair production and double pair production from gamma rays on CMB, RB and low energy background photons. From [31].

The dominant interaction for the case of gamma rays is pair production (PP) on the cosmic background photons:

$$\gamma + \gamma_{CMB,RB} \rightarrow \quad e^+ + e^- \ . \tag{1.25}$$

with threshold energy:

$$E_{th} = \frac{m_e^2}{\epsilon} \simeq 2.6 \cdot 10^{11} (\frac{\epsilon}{eV})^{-1} \text{ eV} \approx 2.6 \cdot 10^{14} \text{ eV} \ . \tag{1.26}$$

In Fig.1.7 right panel, the interaction length (dashed line) and attenuation length (solid line) for pair production on CMB (thin lines), RB and total low energy background, is plotted as a function of energy. As for the nucleon case photons of energies $\sim 10^{20}$ eV cannot reach us from distances beyond some tenths on Mpc, the uncertainty is due to the estimation of the absorbing radio background.

The electrons (and positrons) undergo inverse Compton scattering (ICS) producing a photon which carries most of the initial energy and can produce a secondary electron-positron pair. This leads to the development of an electromagnetic cascade which finally produces photons with energies below the PP threshold. At this point, the interaction between photons and infrared background (IR) dominates, ending up at ~ 100 GeV.

The production of high energy neutrinos is associated to proton acceleration for instance in active galactic nuclei and jets [144], and in gamma ray bursts [159]. As already mentioned the main energy loss process is pion photo-production on the background radiation at the source and during cosmic ray propagation.

Neutrinos originate from the decay of charged pions, and the subsequent generated muons. Their energy spectrum is expected, in case of AGN, to mirror the proton spectrum having a cutoff above energies of the order 10^{18} eV.

This flux suffers from a negligible attenuation by the interaction with the background radiation, thus even if it originates in extremely distant sources, is expected to be detectable. Moreover neutrinos are not deflected by magnetic fields, so that they keep their original direction. A new generation of neutrino telescopes is now in operation, and soon km^3 detectors will be built, thus opening a new window for astronomy at the highest energies.

Photon flux from GZK processes

The GZK processes displayed in Eq. 1.17 produces a flux of neutrinos and photons. The cosmogenic neutrinos have been extensively studied soon after the discovery of CMB and represent an expected complementary source of signals for the neutrino telescopes.
The GZK photons are produced in the decay of the neutral pions, with an energy of about 10% of the original proton. Their flux depends strongly on the sources distribution, on the initial super GZK proton flux and on the maximum proton energy.
During propagation they suffer from energy loss due to pair production on the radio background; the e^+ and e^- in turn produce synchrotron radiation in the extra galactic magnetic fields. The uncertainty on the photon flux, due to the incomplete knowledge of the background, is about one order of magnitude.
Indicative values for the GZK photon fraction in cosmic rays are 0.03 % and $1 \div 3$ % at 10^{19} eV, and between a few percent to even 50 % at $2 \cdot 10^{20}$ eV, assuming a proton energy spectrum of index $\alpha = -2.7$ and $\alpha = -1.5$ respectively. A detailed study has been recently published in [63].
In Fig. 1.8 the fraction of photons in the total UHECR flux above a threshold energy, normalised to the AGASA spectrum (left panel) and to the HiRes spectrum (right panel), is plotted. The pink region show the range of GZK photon fractions expected if only nucleons are produced at the sources. Predictions from ZB, TD, SHDM, along with experimental upper limits from AGASA and Haverah Park are also shown.
For the case of the HiRes spectrum, at energies around a few 10^{19} eV, the minimum fraction predicted from Top-Down models is comparable to the maximum expected from GZK photons. At higher energies the Top-Down flux is instead more than one order of magnitude larger, while is comparable to the GZK flux for the AGASA spectrum.
Large exposure experiments like the Pierre Auger Observatory [124] could allow in the near future the observation of this UHE photons and open a new astronomy window. Even in case of non observation, placing an upper limit on the flux of GZK photons would give complementary information about the UHECR proton component.

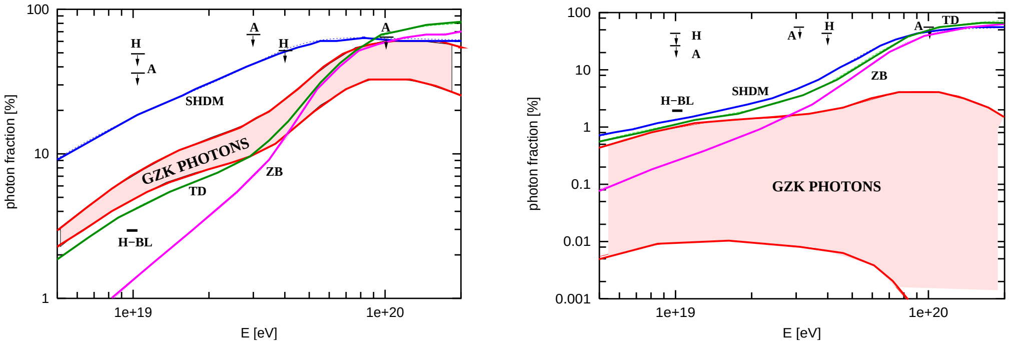

Figure 1.8: Photon fraction in percentage of the total UHECR flux above the energy E normalised to the AGASA spectrum (left panel) and to the HiRes spectrum (right panel). The pink regions show the range of GZK photon fractions expected if only nucleons are produced at the sources. Predictions from ZB, TD, SHDM, along with experimental upper limits from AGASA and Haverah Park are also shown. From [63].

1.4.3 Lorentz invariance violation

At the highest energies there might be a departure from strict Lorentz invariance as suggested in [44]. A term connected to Lorentz invariance violation (LIV) would increase the energy threshold for the formation of the Δ resonance in the GZK process (see Eq. 1.17).

$$4\epsilon \geq (c_{\Delta} - c_p)E + \frac{(m_{\Delta}^2 + m_p^2)}{E} \ , \tag{1.27}$$

where $\delta = (c_{\Delta} - c_p)$ is the Lorentz invariance violating factor, ϵ is the CMB photon energy and E the proton energy.
If $\delta \neq 0$ the equation becomes quadratic in E and it's solvable for $\delta \leq \epsilon/E_{th}$ that is the energy threshold of the process in the Lorentz invariant case.
At the critical value $\delta^* = \epsilon/E_{th} \sim 10^{-25}$ the energy threshold value is doubled. This term brings then to suppression or forbids the inelastic collisions of nucleons with microwave background photons. Therefore the energy spectrum of UHECRs may extend above 10^{20} eV without the predicted GZK cutoff and with the sources of these particles at cosmological distances.
Since the departure from Lorentz invariance is too small to be detected at accelerator energies, an experimental confirmation, by cosmic rays experiments, that GZK processes occur at the expected thresholds, would allow to put strong constraints on such effects.
Regarding the electromagnetic sector, the key process is the pair production by high-energy gamma-rays on the CMB (see Eq. 1.25). This could be highly suppressed or forbidden in the LIV scenario, where the energy thresholds are affected by dispersion factors as:

$$\omega^2 = k^2 \pm \xi_n k^2 (k/M_{Pl})^n \ , \tag{1.28}$$

where ω and k are the component of the photon quadrimomentum, $M_{Pl} \simeq 10^{19}$ GeV is the Plank mass. Non zero dispersion terms would lead to a significant higher fraction of gamma-rays in the cosmic ray flux, at energies around $\sim 10^{19}$ eV, that should be detectable.
Current limits to the photon fraction in the ultra-high energy cosmic ray flux can already significantly constraint the LIV dispersion factors to $\xi_1 < 2.4 \cdot 10^{-15}$ and $\xi_2 < 2.4 \cdot 10^{-7}$, several order of magnitude lower values compared to previous limits [61].

Chapter 2

UHECR detection

Due to the low flux, of the order of one particle per m^2 per year at energies above 10^{15} eV, direct detection of cosmic rays becomes unpractical. The effective area of the detectors, mainly space based, is too low to compensate the steeply falling spectrum.
The first experimental observation of what he named the “extensive cosmic-ray showers”, has been claimed by Pierre Auger in 1939 [13]. He and his collaborators detected coincident signals in counters increasingly displaced at different altitudes, and proved the existence of penetrating primary particles of an energy of the order 10^{15} eV.
Since then, the increasing interest and a parallel development of the experimental techniques allowed the detection and study of the highest energy cosmic particles. Large arrays of detectors, fulfilling the requirements on the aperture and the efficiency, have been designed to sample the particle densities on ground. Moreover, the longitudinal development of the EAS, can be observed by detecting air-fluorescence light produced by the passage of shower particles through the atmosphere. A new generation of detectors exploits the emission of coherent signals in the radio frequencies, or acoustic waves during EAS development.
The combination of different techniques in a single project, allowing independent measurements and detector cross calibration, represents the key solution to overcome experimental uncertainties and increase the measurements accuracy.
In this chapter we recall some general characteristics of extensive air showers, in particular section 2.2 is focused on photons as EAS primaries, then we present the experimental techniques to detect ultra-high energy cosmic rays.

2.1 Physics of extensive air showers

When they enter the top of the Earth atmosphere, ultra-high energy cosmic rays induce, by interaction with air nuclei, a cascade of secondary particles, namely an extensive air shower (EAS). The cascade develops traversing the atmosphere until it reaches a maximum number of particles at a depth, which depends on the primary energy and composition. When the energy of the secondary particles falls below the threshold for further particle production, the shower is attenuated and the deposited energy decreases.

The EAS can be schematically thought as a sum of three components, namely the electromagnetic, the muonic and the hadronic component. The core of the shower consists of high-energy hadrons which feed the electromagnetic and muonic components mainly via pion production and decay. The neutral pions immediately decay into 2γ (decay length $\sim 10^{-6}$ cm), which initiate an electromagnetic cascade via pair production and Bremsstrahlung. At each hadronic interaction almost one third of the energy is transferred to the electromagnetic component.

The charged pions, with a much higher decay length (~ 780 cm), can decay or re-interact, depending on their energy. A fraction of the primary energy is lost, mainly into neutrinos.

A toy model for the development of electromagnetic cascades was suggested by Heitler [72]. He assumed particles of the same type interacting at length λ. After every interaction length the number of particles is doubled and the energy is then $E_0/2^n$, see Fig. 2.1 left panel. The development stops when the particles in the cascade reach a critical energy E_c where the interaction cross-section for Bremsstrahlung significantly drops. Energy is then mainly lost by ionization and the number size of the shower decreases.

The maximum number of particles in the shower is then the ratio of primary energy and critical energy, $\mathrm{N_{max}} = E_0/E_c$. The depth of shower maximum is obtained by determining the number of interaction length for which the energy is reduced to E_c, $\mathrm{X}_{max} = \lambda \ln (E_0/E_c)$. Even neglecting the details these two results account for the macroscopic characteristics of the electromagnetic dominated showers.

A key quantity, independent of primary energy, (it turns out to be sensitive to the primary composition) is the *elongation rate*, defined as:

$$D_\gamma \equiv \frac{\mathrm{dX_{max}}}{\mathrm{d}\log_{10}(\mathrm{E_0})} = \ln(10)\frac{\mathrm{dX_{max}}}{\mathrm{d}\ln(\mathrm{E_0})} \simeq 2.3\ \lambda\ . \tag{2.1}$$

The radiation length in air is $\lambda_r \simeq 36\ \mathrm{g\,cm^{-2}}$ which yields an increase of the depth of shower maximum of $85\ \mathrm{g\,cm^{-2}}$ per energy decade.

To model a shower induced by hadrons a similar simple approach is adopted. A sketch of the model is shown in Fig. 2.1, right panel. The atmosphere is divided in layers of fixed thickness $\lambda_i \ln(2)$, where λ_i is the interaction length of strongly interacting particles. A good approximation for interactions below 10^5 GeV gives for pions in air $\lambda_i \sim 120\ \mathrm{g\,cm^{-2}}$. Thus the hadronic component carries a large fraction of the shower energy much deeper in the atmosphere with respect to the electromagnetic component.

The primary energy is divided in n_π charged pions and N_{max} electromagnetic particles in sub-showers. It energy can be written as:

$$E_0 = E_c N_e^{max} + E_c^\pi N_\mu \approx 0.85\ \mathrm{GeV}(N_e + 24 N_\mu)\ . \tag{2.2}$$

Typical values for the critical energies are $E_c = 85$ MeV, $E_c^\pi = 20$GeV; the electromagnetic fraction is $\sim 90\%$ at 10^{17} eV [96].

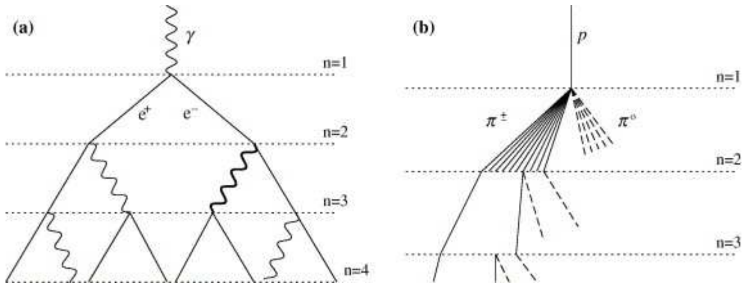

Figure 2.1: Left: schematic view of an electromagnetic cascade, following the Heitler model at each interaction length the number of particles doubles and the energy is $E_0/2^n$. Right: sketch of the hadronic cascade, dashed lines indicate neutral pions and solid lines charged pions (at level 2 only). From [96]

The electron and muon number as a function of primary energy can be derived as:

$$N_\mu \approx 10^4 \left(\frac{E_0}{PeV}\right)^{0.85} \qquad N_e \approx 10^6 \left(\frac{E_0}{PeV}\right)^{1.03} \quad . \tag{2.3}$$

Assuming that only the first generation of neutral pions contribute to the electromagnetic component, if n_π is now the number of charged pions produced in the first interaction occurring at depth $X_0 = \lambda_i \ln(2)$ (function of the primary energy E_0), we have for the depth of shower maximum:

$$X_{max} = X_0 + \lambda_r \ln\left(\frac{E_0}{(3n_\pi)E_c}\right) . \tag{2.4}$$

The estimate is far from being exact, underestimating the X_{max} , since the interactions after the first are neglected. The inelasticity factor, i.e. the fraction of energy carried away in the collision by the leading particle, is also not considered. However with this approximation we can fairly derive the elongation rate for a proton as:

$$D_p = D_\gamma + \frac{\mathrm{d}}{\mathrm{d}\log_{10}(\mathrm{E}_0)}(X_0 - \lambda_r \ln(3n_\pi)) . \tag{2.5}$$

The reduction in the elongation rate, now $\sim 58\ \mathrm{g\,cm^{-2}}$ per decade , is due to two different effects: the higher multiplicity connected with n_π and the increasing cross-section which reduces X_0.

To model the interactions of a cosmic ray nucleus with the atmosphere the superposition model can be applied. A nucleus with atomic number A and total energy E is taken as A individual single nucleons, each with energy E/A, acting independently. The resulting air shower is treated as the sum of A separate proton air showers starting at the same point. We have then for the depth of shower maximum $X^A_{max} = X^p_{max} - \lambda_r \ln A$, which gives a shallower X_{max} for showers initiated by heavier nuclei. Moreover the elongation rate for different primary nuclei can be described by a family of parallel straight lines.

2.2 Photons as EAS primaries

Distinctive characteristics of photon initiated air showers would be a deeper position of the shower maximum and a smaller muonic component. The delayed development of the photon showers resulting in a higher elongation rate is a consequence of the smaller multiplicity of the electromagnetic interactions comparing to the hadron ones. The larger interaction length for photo-nuclear and direct muon pair production with respect to the radiation length is instead responsible for the dominant electromagnetic component. The deviation from hadron expectations could then offer a clear signature detectable from both fluorescence telescopes and surface detector, using the two most sensitive observables: X_{max} and the rise time of the Čerenkov signal.
At the highest energies two competing mechanisms, the Landau-Pomeranchuk-Migdal effect (LPM) and the pair production and magnetic Bremsstrahlung (preshower) effect, are operating. In case of photons the effects of LPM become already significant at an energy of 10 EeV as shown in Fig. 2.2. The average X_{max} as a function of primary energy for simulated photons, protons and iron nuclei is plotted here together with experimental data [91]. As derived in section 2.1, the elongation rate for hadrons is of the order of 58 $\mathrm{g\,cm^{-2}}$ while for photons is about 85 $\mathrm{g\,cm^{-2}}$ per energy decade. Above 10 EeV the LPM effect becomes important and the shower development is even further delayed with respect to hadrons. At energies of an order of magnitude higher and further above, the probability of conversion in the geomagnetic field becomes significative. The electrons radiate strongly, possibly initiating an electromagnetic cascade. Instead of a unique photon, a "preshower" consisting of lower energy electrons and photons, is expected to enter the upper atmosphere, thus resulting in a compensation of the LPM effect on the elongation rate.

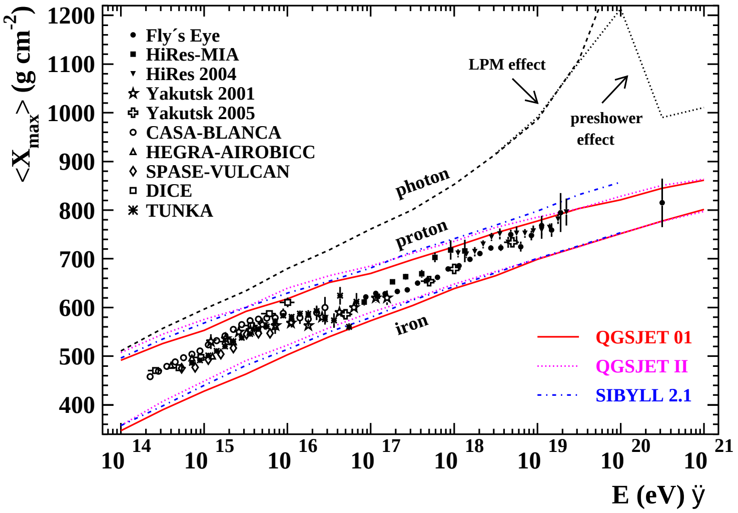

Figure 2.2: From [132]: average depth of shower maximum as a function of primary energy for simulated photons, protons and iron nuclei. The LPM effect and the preshower effect are taken into account in photon simulations. For a complete reference to displayed data see [91].

2.2.1 The Landau-Pomeranchuk-Migdal effect

The electromagnetic component of air showers is brought on by Bremsstrahlung and pair-production. Those processes are governed by the Bethe-Heitler cross section [30]. It has been shown [97] that the traversed medium, in case of air showers the atmosphere, can strongly affect the cross sections suppressing both processes.

The suppressing mechanism originates from the kinematics of the two processes. For a ultra relativistic particle the momentum transfer is in both cases small, especially in the longitudinal direction. In terms of uncertainty principle the interaction must take place over a long distance, the so called formation or coherence length. Interfering processes, as multiple scattering and Compton scattering, occurring over the formation length, can increase the momentum transfer of the particle to the nucleus of the traversed medium. The coherence length is then reduced and the process suppressed. The effective radiation length is then increased resulting in a slower development of the shower and in much larger shower to shower fluctuations.

The energy threshold for LPM depends on the density and temperature of the traversed medium. For photon primaries in the high atmosphere LPM begins to be important at an energy of about 10 EeV and the effect even increases with increasing atmospheric depth.

2.2.2 The preshower effect

Photon primaries with energy above 10^{19} eV, have a large probability to convert into an electron-positron pair in the magnetic field of the Earth before entering the atmosphere. Since the relevant parameter is the product $E_\gamma\ B_\perp$, where E_γ is the primary photon energy, $B_\perp$ the transverse component of the geomagnetic field, this effect is expected to depend on the direction of observation with respect to the Earth frame.

The rate of occurring pair production can be expressed as

$$\alpha_{pp}\,(\chi) = \frac{\alpha\, m_e c}{2\hbar}\ \frac{B_\perp}{B_c}\ T(\chi), \tag{2.6}$$

where α is the fine structure constant and $B_c \equiv m_e^2 c^3/e\hbar \simeq 4.4 \cdot 10^{13}$ G is the natural measure for magnetic field strength [51]. $T(\chi)$ is a function of the following dimensionless parameter:

$$\chi = \frac{E_\gamma}{2\, m_e c^2}\ \frac{B_\perp}{B_c}, \tag{2.7}$$

which can be approximated by $0.46 \cdot \exp(-4/3\chi)$ and $0.60\ \chi^{-1/3}$, for $\chi \ll 1$ or $\chi \gg 1$ respectively [80]. Thus the probability for conversion over the distance R is:

$$P_{conv}\ (R) = 1 - \exp\left[-\int_0^R \alpha_{pp}(\chi(r))\right]. \tag{2.8}$$

Considering a transverse field of ~ 0.1 G, the conversion probability in the magnetosphere starts to become significative for energies of the order $\sim 10^{19}$ eV and increases quickly towards higher energies. At medium latitudes, a photon of energy above 10^{20} eV, converts almost surely before entering the atmosphere, except in a cone of 30° around the direction of the local field. Such a dependence, if observed in cosmic ray experiments, could be a very strong signature of primary photons.

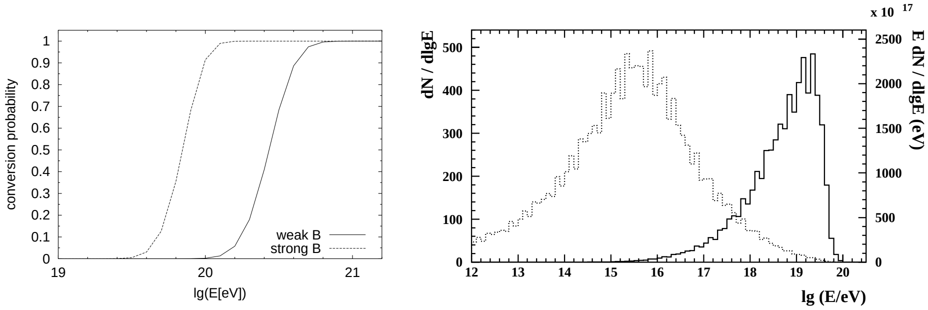

Figure 2.3: Left panel: conversion probability for photons in the geomagnetic field, as a function of primary energy, calculated for two different directions with respect to the local geomagnetic field of the Pierre Auger Observatory [80]. Right panel: spectrum of preshower particles produced in simulations for the Fly's Eye event [129]; the right curve is the spectrum weighted for energy.

Due to the strong decrease of the field with altitude, the probability per unit of length increases rapidly along the trajectory. As a consequence, a EHE photon will produce a pair at high altitude, depending on the strength of the local field, and on the direction of incidence with respect to the field. Typical values for the conversion altitude above the Earth surface, at energies of 10^{20} eV, are around a few thousand km.

The electrons produced at those high energies radiate strongly in the Earth magnetic field. The resulting photon spectrum has a significative extension over several decades below the primary energy E_γ. If the product $E_\gamma \cdot B_\perp$ is large enough, the most energetic photons, radiated by the first pair, produce secondary $e^+ \, e^-$ pairs before entering the atmosphere. An electromagnetic cascade can then develop, as long as the photons are radiated with enough energy to convert in the local field. Finally, this "preshower" which enters the atmosphere, consists of one or a few electron-positron pairs with energy around 10^{18} eV, and a large number of photons with energy below a few 10^{19} eV, which carry most of the initial photon energy.

2.2.3 Photonuclear cross section

The extensive air showers induced in the atmosphere by primary photons are dominated by the electromagnetic component, but contain also a hadronic/muonic component. The dominant process for muon production in an electromagnetic cascade is photo-production. The reaction products are essentially like those of a pion-nucleus interaction. Muons originate from the decay of the produced pions and kaons in the resulting hadronic sub-showers.

The cross-section for photo-production has been measured up to 10^4 GeV for the incident photons in the laboratory frame. In Fig. 2.4 data and extrapolations for the photonuclear cross-section, $\sigma_{\gamma p}$, are plotted (from [15]). A more extreme parameterization giving $\sigma_{\gamma p} \sim 10$ mb at the highest energies has been also proposed [48].

Above the resonance region the cross section is ~ 100 μb per nucleon, and rises slowly for photon energies above 10 GeV. The corresponding cross-section on air nuclei is ~ 1.1 mb, obtained scaling $\sigma_{\gamma A} \simeq A^\beta \sigma_{\gamma p}$, with $\beta \sim 0.9$.

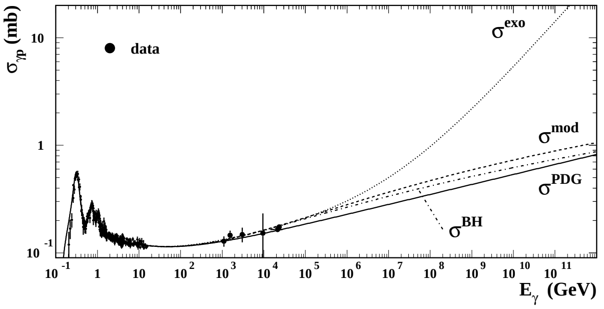

Figure 2.4: Data and extrapolations of the photonuclear cross-section $\sigma_{\gamma p}$ at the highest energies. For references see [131].

The ratio of the photohadronic cross-section to the pair production cross-section gives the relative probability of a hadronic interaction:

$$Q = \frac{\sigma_{\gamma\ \rightarrow\ \mathrm{hadrons}}}{\sigma_{\gamma\ \rightarrow\ \mathrm{e}^+\ \mathrm{e}^-}} \simeq 2.8 \cdot 10^{-3}, \tag{2.9}$$

which grows with the incident photon energy because of the rise in the photo-production cross section, and it is expected to be $\sim 10^{-2}$ at 10^{19} eV.
A positive change in the photonuclear cross-section value influences the rate of transferring energy to hadrons enhancing the production of secondary muons. Moreover the depth of shower maximum is decreased, resulting in a shower with more hadron-like characteristics. In case of a photonuclear interaction occurring as the first place in the atmosphere, the resulting shower would be hardly distinguishable from an hadronic cascade.
The relative probability of photo-production is further enhanced at ultra-high energies when the LPM effect takes place. Further details about the impact of the photonuclear cross-section on shower phenomenology and the consequences on showers simulations, are discussed in [131].

2.3 EAS detection techniques

2.3.1 Fluorescence telescopes

As the primary cosmic ray enters the atmosphere and the secondary cascade develops, the ionizing particles in the shower produce light by exciting the 2P and 1N band systems of N_2 and N_2^+ molecules. The spectrum is mainly emitted in the wavelength region $300 \div 400$ nm, a range in which atmospheric absorption is minimal. The fluorescence photons are emitted isotropically along the shower track, resulting in a spherical light source moving approximately at the speed of light. The fluorescence yield is approximately 4 photons per meter per ionizing particle and depends on particle energies and atmospheric pressure. Precise measurements of the air-fluorescence efficiency are crucial to increase the accuracy of the primary energy determination.
The first experiment which successfully made use of this technique is the Fly's Eye [16], followed by HiRes [33] and lately by Telescope Array [147]. A fluorescence telescope consists of mirrors which collect the photons and focus them on an array of photomultiplier

tubes (PMTs). While traversing the telescope field of view, the shower produces a characteristic pattern of triggered pixel, which identifies the shower-detector plane (SDP). The PMTs signal charge as a function of time is recorded. The typical sampling time is of the order 100 ns.

This information is then used to fix the shower geometry inside the SDP and, after correcting for atmospheric attenuation, to determine the longitudinal shower profile, defined as the number of ionizing particles as a function of atmospheric depth.

The parameterization of the longitudinal shower development of hadronic showers as a function of the depth of first interaction, size and depth of shower maximum, as derived by Gaisser and Hillas [60], can be written as:

$$N\left(X\right) = N_{max}\left(\frac{X - X_0}{X_{max} - X_0}\right)^{\frac{(X_{max}-X_0)}{\lambda}} \quad \cdot \quad \exp\left[\frac{(X_{max} - X)}{\lambda}\right] , \tag{2.10}$$

where X_0 is the depth of first interaction, main source of shower-to-shower fluctuations, and $\lambda \sim 70\ \mathrm{g\,cm^{-2}}$ energy dependent. The integral of this profile is proportional to the primary shower energy and the proportionality constant is largely independent of the hadronic physics at the primary interaction. The "calorimetric" energy can be derived as:

$$E_{cal} = \alpha \int_0^\infty N\ (X)\ dX\ , \tag{2.11}$$

where α is a constant that expresses the average rate of energy loss for ionization in the shower and is $\sim 2.2\ \mathrm{MeV/g\,cm^{-2}}$. Actually this number should equal the ratio between critical energy and radiation length. A correction for missing energy, the "invisible" energy fraction carried mainly by neutrinos and high-energy muons, has then to be applied. The correction depends on the primary energy and particle type. In Fig. 2.5 (left panel) the fraction of calorimetric energy to primary energy, E_{cal}/E_0, is plotted as a function of E_{cal} for protons and iron nuclei at different zenith angles. The right panel shows the simulations result adopting different hadronic interaction models. In case of nuclear primaries, the correction amounts to $7 \div 14\%$, with a slight dependence on zenith angle and a significant dependence on primary energy and hadronic interaction model [18]. For photon primaries, the missing energy fraction is much smaller and amounts to $\sim 1\%$, see also [113].

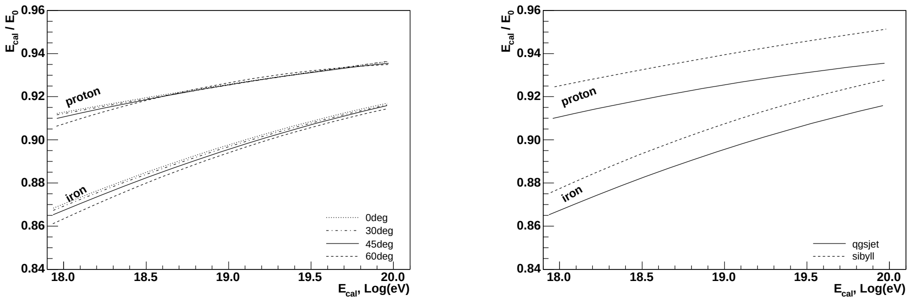

Figure 2.5: Left panel: ratio of calorimetric energy to primary energy E_{cal}/E_0 as a function of E_{cal} for protons and iron nuclei at different zenith angles. Right panel: dependence on the different hadronic models. From [18].

Fluorescence signal

The expected fluorescence signal at the detector aperture is given by:

$$N_\gamma = N_e \cdot Y \cdot c\ \Delta t \cdot Q_e \cdot \frac{A}{4\pi r^2} \cdot \exp\left[-\frac{r}{r_0}\right] , \tag{2.12}$$

where Y is the fluorescence yield, $c\Delta t$ is the track element viewed in the integration time Δt, Q_e is the quantum efficiency of the optical devices and A is the telescope diaphragm area. The exponential term account for the atmospheric transmission.
The background signal due to the night sky is:

$$N_{bg} = I_{bg} \cdot \Delta t \cdot A \cdot Q_e \cdot (\Delta\theta)^2 , \tag{2.13}$$

where I_{bg} is the night sky intensity (in photons/$m^2/sr/\mu s$). The signal to noise ratio is then:

$$\frac{N_\gamma}{\sqrt{N_{bg}}} = N_e \cdot Y \frac{c}{4\pi r^2} \cdot \sqrt{\frac{\Delta t\ Q_e\ A}{I_{bg}\Delta\theta}} \cdot \exp\left[-\frac{r}{r_0}\right] . \tag{2.14}$$

To optimise the signal to noise ratio, a large collection area equipped with small viewing angle and high efficiency optical devices, is required. The optimal signal integration time window must also be derived by a study of the typical signal durations.

2.3.2 Surface detector arrays

Simple detectors or counters organised in arrays, can sample the energy deposit or the number of particles produced by a primary cosmic ray in an extensive air showers at a given observation level, i.e. the EAS footprint.
The parameters which characterise this type of detection are the observation level, the array surface and the detectors spacing. The site altitude determines at with atmospheric depth the average longitudinal development of the showers is studied, for instance close or above the shower maximum. The geometric area is related to the events rate expected at a given energy and has to match the dimensions of the cascades. Since large areas cannot be fully equipped with devices, the detectors spacing must be optimised to guarantee an efficient sampling of the particles densities in order to reconstruct accurately the primary energy.
The particle density as a function of distance from the core, is typically measured with plastic scintillators or Čerenkov detectors. The direction of the shower axis is at first determined by fitting the hit time pattern assuming a planar shower front. The lateral distribution function, corrected by zenith angle effects, can then be fitted in order to estimate the primary energy.
There are significant fluctuations in the position of depth of shower maximum for an event with the same energy and atomic mass. Hillas [23] proposed a method to reduce the influence of shower development fluctuations on the determination of shower energy by ground array experiments. The method relies on the fact that particles at distances of $500 \div 1000$ m from the core of the EAS have been most likely produced at shower maximum. Since the shower size at maximum, N$_{max}$, is proportional to primary energy and the fluctuations are minimised in this stage of shower development, a measurement of the density far away from the core should give more accurate results.

The lateral distribution of particles is mainly determined by Coulomb scattering of the dominant electromagnetic component and can be approximated by the Nishimura-Kamata-Greisen (NKG) function [68][84]:

$$\rho(r) = k \left(\frac{r}{r_M}\right)^{-\alpha} \left(1 + \frac{r}{r_M}\right)^{-(\eta-\alpha)} \quad , \tag{2.15}$$

where r_M is the Moliere radius $\approx$ 78 m at see level for low energy particles; η, α are parameters determined experimentally and k is proportional to shower size.
The lateral distribution of muons and their number, depends on the distribution of charged pions produced in the hadronic interactions, and on the likelihood of their decays. High energy muons are produced most likely at low depths from the decay of high energy pions, thus they reflect processes occurring in the early development of the cascade. The muon content of the EAS at ground level depends on the nature of the primary. Thus, surface arrays with the capability to distinguish muons from electrons and photons are sensitive to the primary cosmic ray composition.

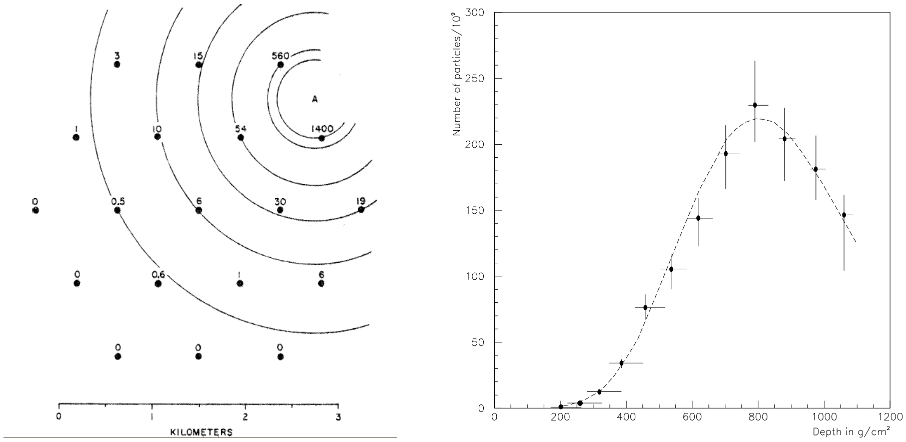

Figure 2.6: Left: particle density at ground for the highest energy event recorded by the surface array of Volcano Ranch [95]. Right: longitudinal shower profile of the highest energy event recorded by the fluorescence telescope of Fly's Eye [34].

2.3.3 Radio and acoustic detection

In addition to these "classic" detection techniques, it may also be possible to exploit the radio frequency (RF) pulses generated by air-showers. CR showers induce radio pulses through several mechanisms, the dominant process is coherent synchrotron emission by the electron-positron pairs propagating in the Earth magnetic field.
Radio pulses of about $20 \div 100$ MHz, coincident with EASs were first measured in 1966 [20]. Recently the Low-Frequency Array (LOFAR) [54] has been proposed in the context of next generation digital telescopes. This device consists of around 100 stations of 100 dipoles antennas distributed over a region about 400 km in radius. According to the cited work, LOFAR should be able to observe events up to 10^{20} eV at a rate of the order of 1 per year.

The CR energy range for which one achieves both a reasonable signal-to-noise ratio and a reasonable event rate depends on the number of dipoles actually employed. A single LOFAR-type station of about 100 dipoles, for example, would be useful for measurements in the range $10^{15} \div 10^{17}$ eV; To study different station configurations and optimise the detection performances, a prototype station, has been setup since 2003 at the KASCADE experiment site, see [82].
The main advantages of radio detection compared to other techniques are that radio signals are not absorbed nor deflected on their path, and the amplitude of the signal is proportional to the primary energy of the incoming particle. Moreover the duty cycle is in principle 100%, which guarantees a large data volume necessary for statistical analysis. An array of about 20 km^2 to be deployed at the Pierre Auger site, is currently in R&D phase, see [155]. Studies for an extension of the surface array located on top of the IceCube detector are underway [86].
Another technique which is now being explored, expecially in combination with large scale neutrino telescopes under the sea or ice, is based on acoustic sensors. They detect the signals produced by high-energy particle cascades which for short time heat the traversed volume. This effect, leading to a pressure pulse with amplitude dependent on primary energy, was suggested by Askaryan [12] already in 1957. The acoustic signals have a range $1 \div 100$ kHz with peak frequency at about 30 kHz.
The absorption length for acoustic waves with this frequency in sea water is at least an order of magnitude larger than that of Čerenkov radiation. Therefore acoustic signals can be detected at larger distances (~ 1000 m) with respect to Čerenkov light. Current tests of detector prototypes along with studies of the background are underway at various sites [39] [38], see [102] for a detailed review.

Chapter 3

Overview of experimental results

Is the GZK cutoff present?
At what energy does it occur?
How steep is the falloff above the cutoff?
What is the energy of the ankle?
What are the power law indices below and above it?
What is the composition as a function of energy?
Is it heavy or light?
Can we see a transition region?
Is the transition at the ankle or lower in energy?
What is the cause of the second knee?
Is the second knee a galactic feature or an extragalactic feature?
What are the sources of the highest energy cosmic rays?
Is there anisotropy in the cosmic ray flux that points to sources?
Is there large-scale anisotropy related to galactic magnetic fields?

P. Sokolsky

3.1 Spectrum and composition

UHECR spectra compilation

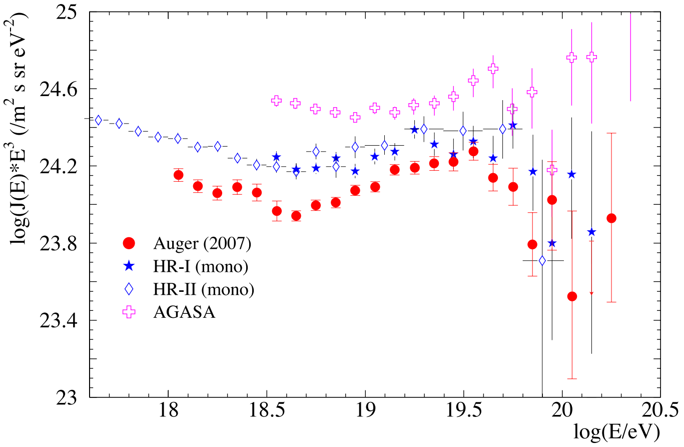

Figure 3.1: Measurements of the cosmic ray energy spectrum at the highest energies by different experiments. The flux is multiplied by E^3 to enphatise the positive slope in the ankle region. Data are plotted for AGASA [146], HiRes [78] and for the Pierre Auger Observatory [110] [133] [161]. HiRes measures the ankle at $\sim 10^{18.65}$ while the GZK feature appears at $\sim 10^{19.75}$. PAO confirms this measurements. AGASA data are under a process of reanalysis. Discrepancies between data are evident, however uncertainties of the order 20% in energy scale must be accounted for.

UHECR spectra rescaled

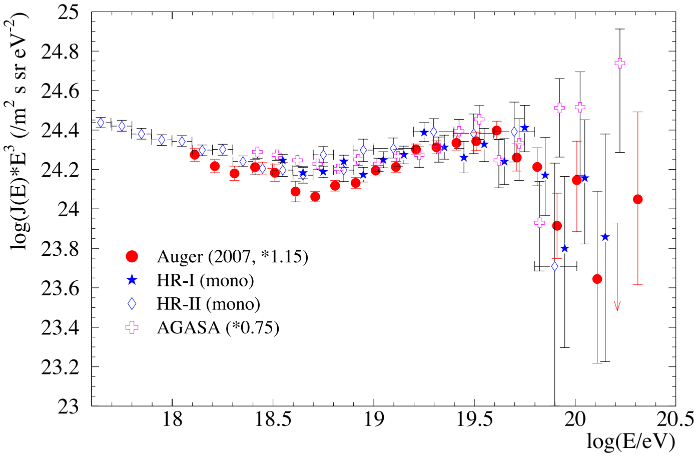

Figure 3.2: Same plot but with AGASA spectrum scaled down by 15% and PAO spectrum scaled up by 15%, from [85]. This shows agreement within the uncertainties on the overall energy scale (22% for Auger [47]).

UHECR spectra measured by the Pierre Auger Observatory

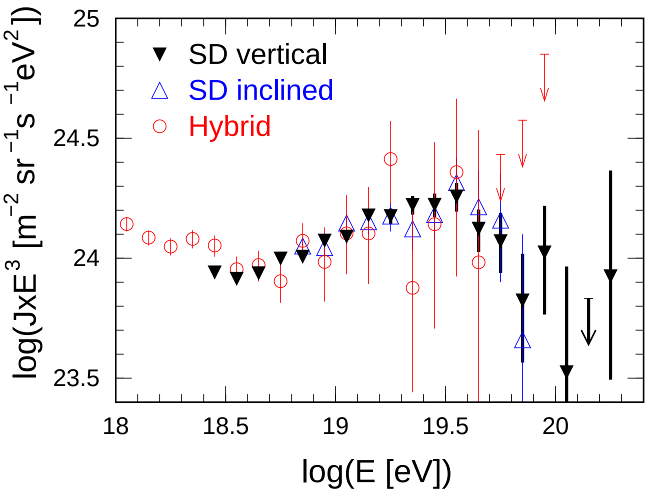

Figure 3.3: Measurements of the cosmic ray energy spectrum at the highest energies by the Pierre Auger Observatory (flux multiplied by E^3). The surface detector array data at zenith angles below 60° [133] (black filled triangles) and larger than 60° [53] (blue open triangles). The hybrid spectrum [110], extending the threshold at lower energies, is also shown (red open circles). Arrows indicate 84% c.l. upper limits.

UHECR spectrum measured by the PAO Fluorescence Detector

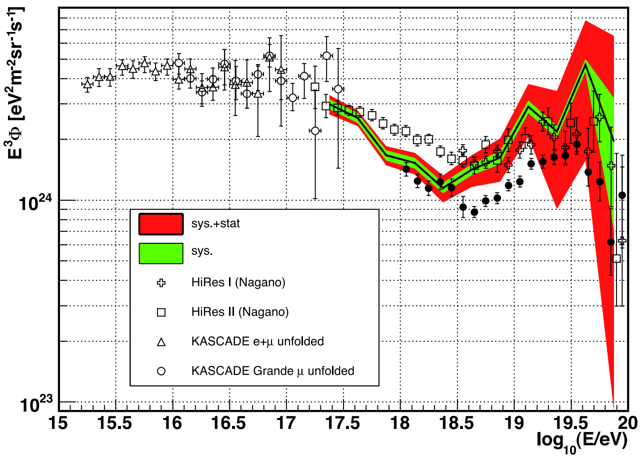

Figure 3.4: Spectrum measured from the Pierre Auger fluorescence detector (FD-mono) [62], along with data from HiRes [78], KASCADE [9], KASCADE-Grande [87] and Auger combined. Agreement is found within the experimental uncertainties.

Testing astrophysical models

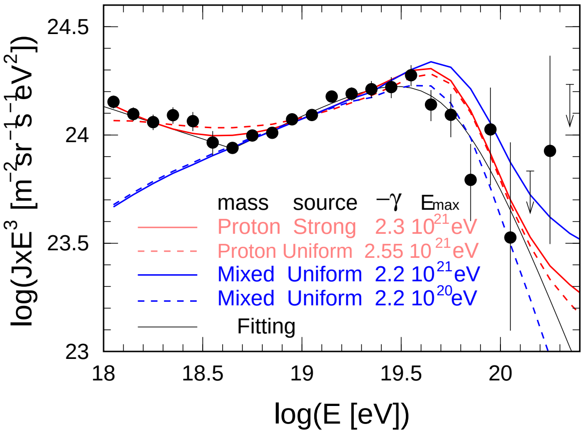

Figure 3.5: The combined Auger energy spectrum multiplied by E^3, together with a fit with a broken power law [161]. Predictions of two astrophysical models (blue and red lines) are also shown [3]. The input assumptions of the models (mass composition at the sources, sources distribution, spectral index and exponential cutoff energy per unit charge at the acceleration site) are indicated in the figure. Precise measurements of the composition before the ankle are needed to discriminate between the models, see also [29].

Mixed composition fit

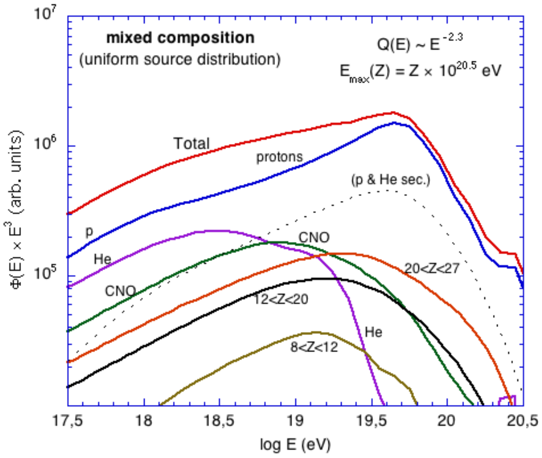

Figure 3.6: Contribution to the spectrum of different elements classes. GZK suppressions can be seen around 10^{19} eV for He and $2 \cdot 10^{19}$ eV for the CNO group. The dotted line shows the contribution of the secondary low mass nuclei (protons and He) resulting from the photo-dissociation of heavier nuclei. Their contribution is responsible for the bump in the spectrum around $5 \cdot 10^{19}$ eV. From [3].

Measurement of the UHECR composition

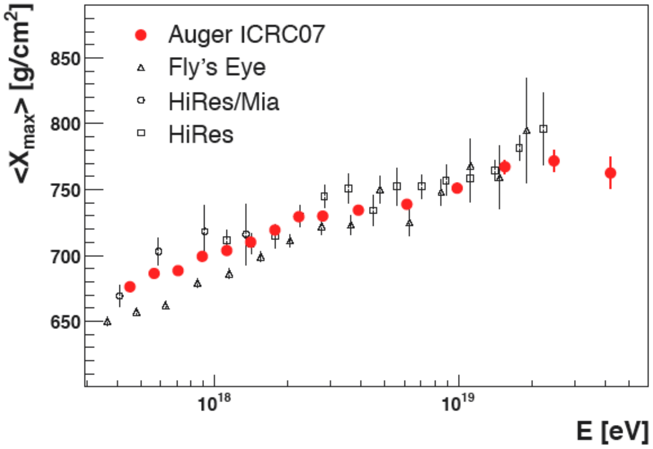

Figure 3.7: Mean depth of shower maximum, X_{max} , as a function of energy, for data from the Pierre Auger Observatory along with previous results from Fly's Eye and HiRes [154]. An unexpected trend towards a heavier composition at the highest energies seems to appear in the PAO data, however within the quoted uncertainties the experiments still agree.

Estimate of the composition change: Pierre Auger

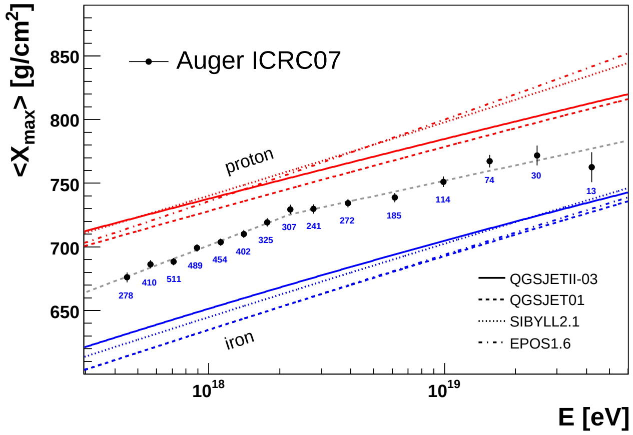

Figure 3.8: Mean X_{max} as a function of energy, the Auger "elongation rate". The number of hybrid events in each energy bin is indicated, and the predictions for pure proton and pure iron from different hadronic interaction models are shown for reference. The dashed line denotes a fit with two constant elongation rates (71 ± 5 and $40 \pm 4 \mathrm{g\,cm^{-2}}$ /decade) and a break-point at$\sim 10^{18.35}$ [154]. A mixed composition is favored, a transition towards light elements at the highest energies is not confirmed.

3.2 Limits to photons and neutrinos

Limits to the photon fraction in cosmic rays

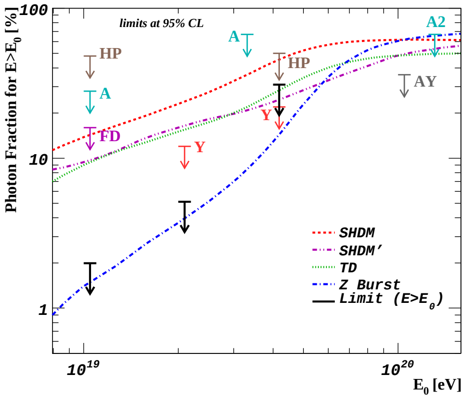

Figure 3.9: Experimental upper limits to the photon fraction in the integral cosmic ray flux (95% c.l.) for Auger SD (Limit $E > E_0$) [21], Auger Hybrid (FD) [119], AGASA (A) [141] and (A2) [130], Haverah Park (HP) [14], Yakutsk data (Y) [65], and a combination of AGASA and Yakutsk data (AY) [134][66]. Also shown the theoretical expectations from different non-acceleration models(ZB, SHDM, TD from [63] and SHDM' from [49]), assuming a spectrum without flux suppression above E_{GZK}, see also [132]. Top-down scenarios are strongly constrained.

Limits to the diffuse flux of neutrinos

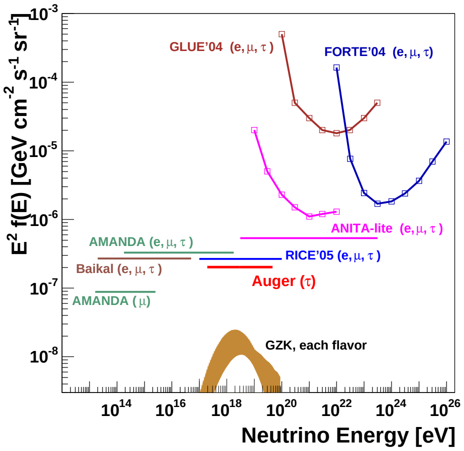

Figure 3.10: Upper limit to the tau neutrino diffuse flux (90% c.l., E^{-2}) derived with data of the Pierre Auger Observatory [35]. For the other experiments see references therein. The PAO sensitivity to Earth skimming or very inclined neutrino events is expected to increase, possibly reaching the expected flux from GZK neutrinos.

3.3 Inelastic proton-air cross section

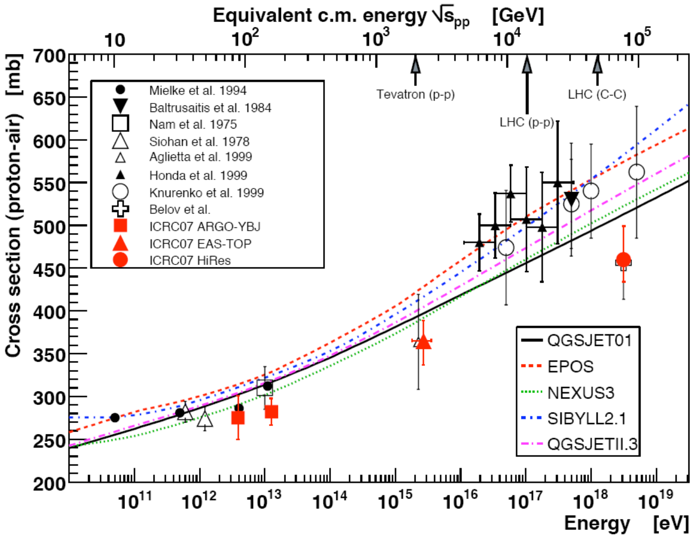

Figure 3.11: The range of cosmic ray experiments extends beyond the energy of the LHC, thus they provide significant and complementary information. New measurements of the proton-air inelastic cross section based on cosmic rays data are shown [50]. Data from [17][81], corrected by [37], [26], for other references see [150].

3.4 Anisotropy studies

Search for large scale anisotropies: the AGASA map

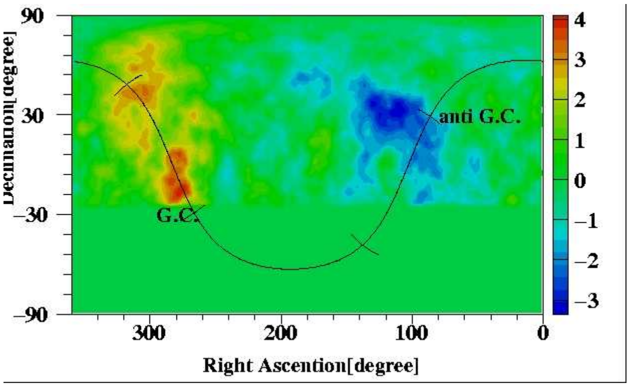
90
30
−30
−90
Declination[degree]
300
200
100
0
Right Ascention[degree]
G.C.
anti G.C.
4
3
2
1
0
−1
−2
−3

Figure 3.12: Significance map with angular size 20°, a 4 σ excess can be seen near the direction of the Galactic Center. In contrast, near the direction of anti-Galactic Center a deficit in the cosmic ray intensity of 3.7σ is found. An event excess from the direction of the Cygnus region is also seen in the significance map at the 3 σ level [2].

Search for excess in the Galactic Center region: Pierre Auger Observatory

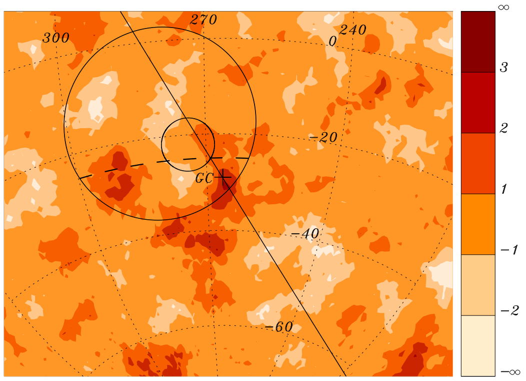
300
270
240
0
−20
−40
−60
GC
∞
3
2
1
−1
−2
−∞

Figure 3.13: Map of the cosmic rays overdensities in the Galactic center (GC) region in circular windows of 5° radius, for Pierre Auger array data with energies in the range $10^{17.9} \div 10^{18.5}$ eV. The GC is marked with a cross and the Galactic plane with the solid line. The large and small circles indicate the regions of the AGASA excess and the SUGAR excess. The picture from the Pierre Auger Observatory data is consistent with what is expected from the fluctuations of an isotropic sky [149].

Correlation of the highest energy events with nearby extragalactic objects: are UHECR protons from AGNs ?

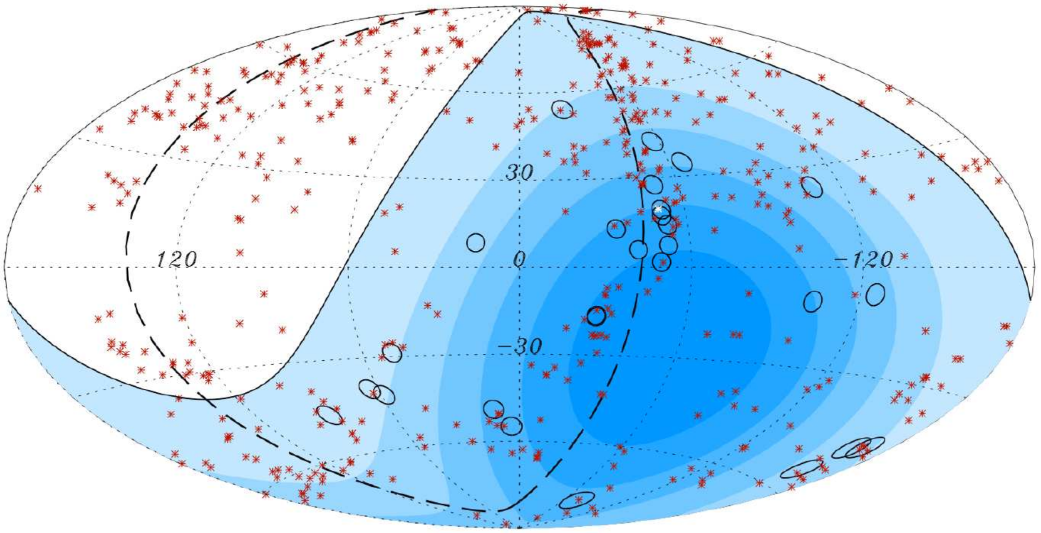

Figure 3.14: Correlation of the highest energy cosmic rays with nearby extragalactic objects [116]. Sky map in galactic coordinates with circles of radius 3° centered at the arrival directions of 27 cosmic rays with reconstructed energies above 57 EeV detected by the Pierre Auger Observatory. The positions of 472 AGN at distance < 75 Mpc following the Vèron-Cetty catalogue of quasars and active galactic nuclei, are indicated by asterisks. The solid line draws the border of the field of view for the southern site of the Observatory shaded bands indicate regions of equal integrated exposure. Centaurus A, one of our closest AGN, is marked in white. 20 out of the 27 observed events correlate with at least one of the selected AGN, while only 5.6 are expected for the case of a isotropic distribution. The probability to achieve this level of correlation starting from an isotropic distribution is $4.6 \cdot 10^{-9}$. This is a **strong indication that AGN may be the sources of UHECR.** The energy threshold at which the correlation is larger coincides with the measured flux suppression above $10^{19.5}$ eV, thus, an association with the origin in nearby objects, is **consistent with the GZK cutoff.** Moreover within energy scale uncertainties a **light primary composition** is highly favored.

Chapter 4

The Pierre Auger Observatory

The challenging aim of the Pierre Auger Observatory (PAO) [124] is to give an answer to the questions on nature and origin of the highest energy cosmic rays, well above 10^{18} eV. It will measure the energy, arrival direction and mass composition of the UHECR with unprecedented statistical and systematic accuracy.
Conceived to be the largest cosmic ray detector, it will consist of two experimental sites, one already in operation in the southern hemisphere, and one to be built in the northern hemisphere, thus providing full sky coverage. The distinctive feature of the project is to combine the most advanced detection techniques in a hybrid solution, thus allowing cross-correlation of independent measurements and reducing systematic uncertainties.
The Pierre Auger Collaboration has gathered at present more than 70 institutions from 17 countries, together around 300 scientists and 100 technicians.
After a first engineering phase, the southern site, located in Malargüe Argentina, is taking reliable data since 2004, and has now almost completed the construction phase reaching its final aperture. Together with the northern site will be soon complete and extend the cosmic ray investigations, possibly opening a new window for astronomy and particle physics.

4.1 The Pierre Auger Observatory: a hybrid detector

The Pierre Auger Observatory is the answer to the need of synergy between the most advanced techniques in UHECR detection, in order to combine and enhance the single detector capabilities, achieving the best possible experimental accuracy.

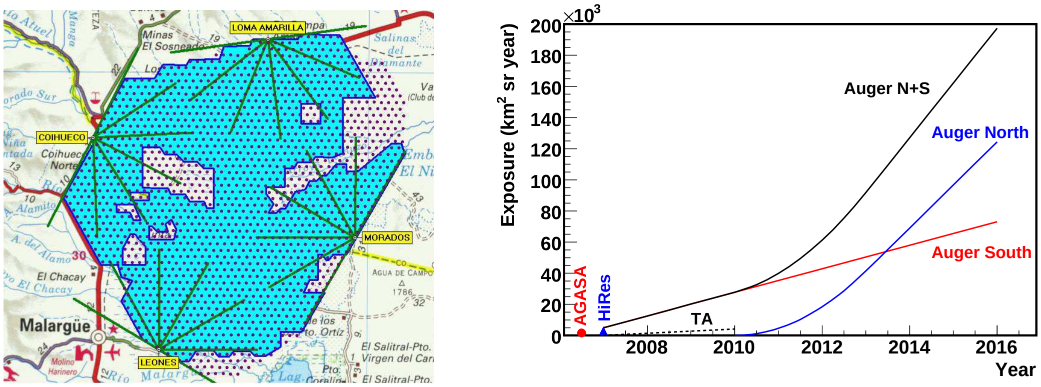

Figure 4.1: Left: map view of the southern Pierre Auger Observatory status in September 2007. The 24 fluorescence telescopes are fully in operation and currently 1500 of the 1600 Čerenkov tanks are deployed (shaded area), completion is scheduled by the beginning of 2008. Right: exposure above 10^{19} eV as a function of time for Auger South (red line) and Auger North (blue line) and the combination of the two (black line); also shown is the exposure for the Telescope Array (black dotted line), from [105].

The advantages of this concept have been described in detail in [142]. The ground array provides a huge collecting area with an easily calculable aperture and a 100% duty cycle. It measures the primary energy in relation to the particle density at 1000 m from the shower core.

The fluorescence detector operates in clear moonless nights, for a total duty cycle of the order of 10%. The fluorescence measurements determine the shower energy in an independent way, integrating the size or energy deposit profile in the atmosphere. Thus it can provide an accurate conversion to connect the particle density on ground with the primary energy, almost independent from model uncertainties.

The current layout of the Pierre Auger Observatory is shown in Fig. 4.1, left panel. The position and field of view of the FD eyes surrounding the array is displayed, dots mark the SD tanks, the light blue shade indicates the deployed area. The map refers to August 2007 with a deployed fraction of $\sim 85\%$, completion is scheduled by the end of 2007.

Fig. 4.1, right panel, shows the exposure above 10^{19} eV as a function of time for Auger South (red line), Auger North (blue line) and the combined exposure. The Telescope Array exposure is shown for comparison (black dotted line), from [105].

We summarise briefly here the characteristics of the PAO detector, with particular attention to the FD-hybrid. For further technical details see [114][115].

4.1.1 The surface array (SD)

The surface array (SD) [145] of the southern site of the Pierre Auger Observatory consists of 1600 Čerenkov detectors spaced by ~ 1.5 km on a triangular grid covering a total area of ~ 3000 km^2. The structure is designed to have high-level performance in highly varying climate conditions and extreme temperature ($-15 \div 50$ °C), typical of the semi-desertic areas.

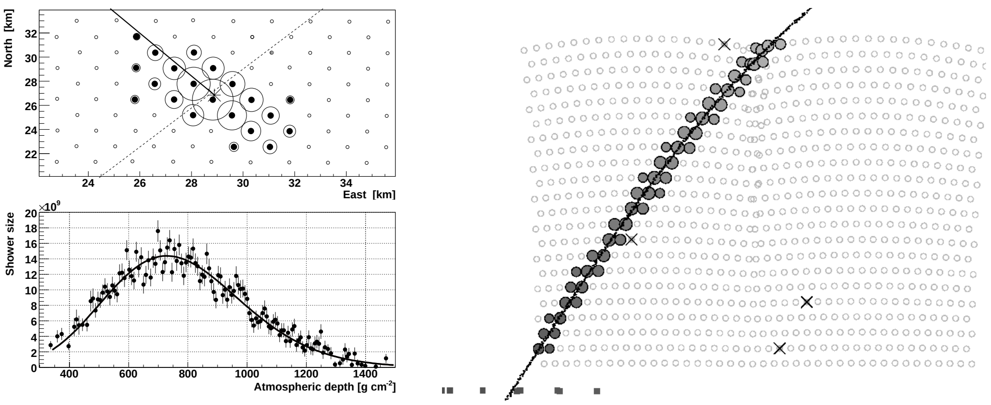

Figure 4.2: Left: array view of the triggered tanks (top panel) and longitudinal profile measured by the fluorescence detector (bottom panel). Right: FD camera view of a hybrid event. The shower detector plane is indicated by the solid line, the squares represent the triggered SD tanks. From [98].

The configuration has been optimised in order to have a fully efficient detector at an energy of $\sim 10^{19}$ eV. The altitude of the site in grammage is $\sim 870\ \mathrm{g\,cm^{-2}}$, just above the shower maximum for protons of energy $\sim 10^{20}$ eV.
The accuracy in determination of the primary direction is $0.6 \div 1.5°$, improving with increasing energy. The energy resolution is of the order of $10 \div 12\%$.

Signal detection

The Čerenkov tanks have a collection surface of $\sim 10\ \mathrm{m}^2$ for a heigth of 1.2 m, containing 12 tonnes of pure water. The large surface allows detecting particles even at low densities ($\sim 1/m^2$) with good statistical precision. The tank heigth is designed to absorb almost completely the electromagnetic component, and to optimise the muon pulse amplitude. Moreover the lateral cross-section increases sensitivity to very inclined showers. They are equipped with three 9 inches photomultiplier tubes (Photonis XP1805), viewing the tank from above. The dynamic range is matched by two different gain channels, a low gain channel connected to the anode and an amplifying stage connected to the last dynode.
Typical signals extend over a few microseconds, but duration and amplitude vary strongly as a function of distance from shower core. Young and vertical showers have the largest spread, both in intensity and in duration, due to the fact that the electromagnetic component is still detectable. Old or very inclined showers have smaller densities near to the core and the pulse is shorter at all distances, as it is mainly due to the muonic component.
The readout is performed by digital electronic modules, FADCs, with 400 MHz sampling rate and 10 bits resolution. The stations host a GPS receiver to synchronise triggered data and a radio communication system, which sends data to the central data acquisition system (CDAS). Independent power supply (about 10 W) is provided by batteries recharged by solar panels. A sketch of the SD tank is shown in Fig. 4.3, left panel.

Trigger modes

Two first level triggers are used: a simple threshold trigger (ThT) and time-over-threshold (ToT) trigger. In addition, a muon trigger allows for recording continuous calibration data.
The ThT is a 3-fold trigger with a threshold at 1.75 VEM (Vertical Equivalent Muon) on each PMT. It is designed to trigger over fast signals, induced for instance by the muonic component of very inclined showers. The ThT trigger rate is ~ 100 Hz.
The ToT trigger requires 12 FADC bins with signals larger than 0.2 VEM in a sliding window of 3 μs in each of 3 or more detectors in a compact configuration. It efficiently triggers on the shower particles far away from the shower core, avoiding single muons. After a few months the average rate of ToT is stable, at the level of 1.6 ± 1Hz.
The on-board second level trigger (T2) is devoted to select physics triggers to be then sent to the CDAS, all the ToT are promoted , while only the 3-fold coincident ThT with threshold 3.2 VEM pass. The final rate of T2 triggers is ~ 20 Hz.
At the CDAS, second-level triggers are promoted to third-level trigger in case 3 stations have passed the ToT or 4 stations have a second level trigger in particular time space configurations, related to the event compactness. These events fill the SD data stream, from which the real showers are then extracted. The "shower conditions" are: compactness of the triggered tanks and sufficient time duration. This rejects spurious events with an efficiency of 99%.
The FD can also drive the third level trigger in hybrid mode. The surface array is then triggered in a sub-threshold mode, and the tanks can be matched in time and position, adding crucial information for the geometry reconstruction. This extends the detector efficiency and the reconstruction capability to energies well below 10^{18} eV.
The probability of a trigger depends on energy and zenith angle of the primary particle. It is derived from measurements in station pairs or obtained parameterising for each event the lateral distribution function from the signals in all triggered stations. The stability and uniformity of the trigger rates is crucial for aperture calculations.

Surface detector calibration

The SD calibration is performed using muons, which give in the PMTs an average signal of ~ 95 photoelectrons. The pulse rise time is about 15 ns. The trigger rates are adjusted to have gain uniformity at the level of $\sim 6\%$ between the photomultipliers. The measurement of the muon charge spectrum allows to derive the charge value for the Vertical Equivalent Muon, from which the calibration is inferred for the whole dynamic range.
The daily variation of atmospheric temperature due to day-night effect are larger than 20°C. Temperature is measured on the PMT bases, on the electronics board, and on the batteries. Typical day-night variations are of the order of 2 ADC counts for the muon peak. They also affect the ToT trigger, so careful monitoring and correction is crucial for data analysis.

4.1.2 The fluorescence detector (FD)

The SD is overviewed by the fluorescence detector (FD) [156], consisting of 4 "eyes" each equipped by 6 Schmidt telescopes with a field of view of 30° × 30°.

The optical system

The optical system consists of a *diaphragm* of 3.8 m^2 aperture, the *mirrors* of 12 m^2 area and 3.4 m radius of curvature. An UV transmitting *filter* (Schott M-UG6) is installed at the aperture to improve the signal-to-noise ratio in the fluorescence band.
To reduce optical aberrations, corrector lenses are installed and arranged in a ring around the diaphragm. With this device the collection area of the telescope is increased while the light spot reflected on the camera surface keeps a maximum angular size of 0.5°.
At the focal surface the structure hosts the *camera*, equipped with 440 hexagonal photomultiplier tubes (PMTs) with inscribed diameter 1.5° arranged in a 22×20 matrix.
The PMTs (Photonis XP-3062 [112]) have a semitransparent bialkaline photo-cathode, the quantum efficiency is about 25% or larger in the spectral band $350 \div 450$ nm. All optical devices have been tested at the production site and after installation. The alignment of the mirror structure and camera, adjusted with precise laser measurements, is monitored continuously via reconstruction of laser shots and analysis of background noise. A sketch of the FD optical system is shown in Fig. 4.3, right panel.

FD electronics and trigger

Each PMT is equipped with a *head electronics unit* (HE) which provides active bias and signal driving [40]. The active network improves linearity over the whole dynamic range compared to a standard passive base that would need to inject a current two times larger to obtain the same performance. The PMT signal is sent back, in differential mode, to the Analog Board (AB), where it is filtered and amplified [11].
Each analog board serves 22 channels, thus 20 modules are installed in the front-end crate to readout the full camera.
The AB controls the gain of the 440 channels, which are equalized via programmable potentiometers to guarantee a uniform amplitude and time response.
A double gain system, the so called *virtual channel* has been adopted to match the dynamic range of 15 bit with the 12 bit FADC resolution. This system consists in a high-gain channel per single PMT, and two low-gain channels per board, which both record the sum of the signals in 11 non adjacent pixels. More details on this system, and its use in the analysis, are given in App. A.
In addition the AB hosts a test pulse system, which allows to emulate fluorescence tracks, which can be driven into the HE and then readout, in order to monitor the performances of the full electronics chain. The electronic noise is kept below 20% of the night sky background. Accurate tests showed that both channel cross-talk and deviations from linearity are minimal.
The analog board is connected to the digital front-end board, which hosts the first level trigger board (FLT) and the second level trigger (SLT). Here the signals from the triggered PMTs are digitized at a 10 MHz sampling rate with 12 bit resolution, and stored in a buffer. The first level trigger threshold is adjusted to have a hit rate of ~ 100 Hz.
The programmable logic chips (FPGAs) allow to test the events searching for different pattern configurations in a 1 μs time window. A sliding matrix of 5×22 pixels scans the full camera in 10 μs. The SLT requirement is 5 adjacent pixels with possibly only one under threshold, as this could be for instance a bad pixel. The SLT trigger rate is at the level of 0.1 Hz.

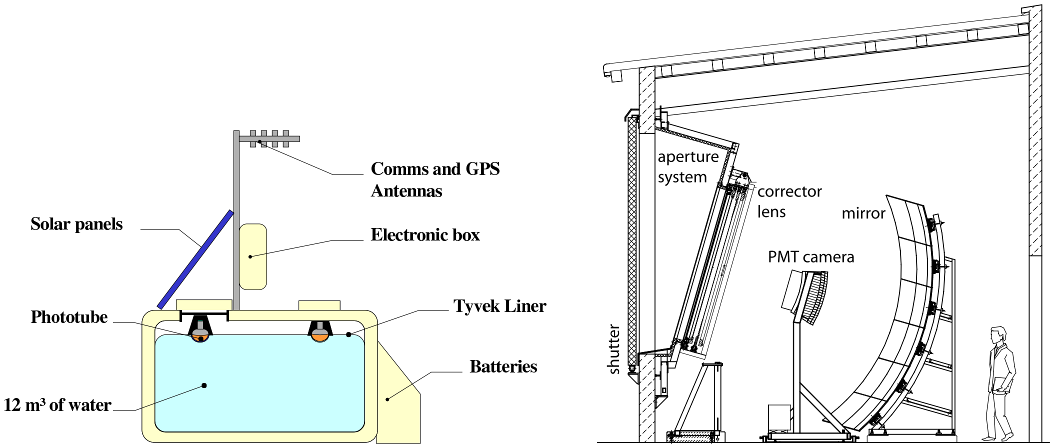

Figure 4.3: Left: sketch of the SD Čerenkov tank [7]. Right: the FD optical system [114].

The *mirror pc* processes the SLT events in order to reject spurious triggers due to noise, by checking the time sequence. After this step the rate is decreased of a factor 10. The sequences are sent via LAN to the *eye pc*, which builds the fluorescence raw event with the information from the telescopes that triggered. This data is stored locally and send to the CDAS to be combined with the information from SD, if available.

The slow control system [19] handles the operational data and experimental conditions which are stored in a local mySql database and available for the on-line monitoring, together with calibration tests and various performance parameters [128].

Fluorescence detector calibration

The calibration of the FD relates the electronic signal recorded by the FD data acquisition system to the flux of photons of a given wavelength at the detector aperture. Two end-to-end methods are used to determine the absolute calibration considering the system as a whole. Relative calibration routines, calA, calB and calC, running on a nightly base, monitor the response and stability of the different optical components.

The *drum calibration* is designed to provide an end to end calibration of the FD using an illuminated surface covering the entrance aperture of an FD telescope. The light source consists of 2 pulsed UV LEDs (375 ± 12 nm). The LEDs are embedded in a Teflon cylinder that sits on top of a 15 cm disk of diffusively reflective Tyvec.

Artificial tracks, generated from a 355 nm laser located ~ 4 km from the FD, are used to confirm the FD calibration obtained by the drum. If the energy and polarization state of the laser beam are well known, Rayleigh scattering from the molecular atmosphere provides an accurately calculable flux of photons arriving at a telescope aperture from each part of the track. An advantage of this calibration method is that it produces a track image that is very similar to the cosmic ray tracks measured by the FD.

To monitor changes in the response of the single components, a relative calibration system has been implemented 3 different xenon flash light sources are mounted located at each FD building. Light from each source is distributed through optical fibers to the six telescopes, at different positions.

The light from the calA source directly illuminates the camera through a diffuser placed at the center of each mirror, to monitor stability and linearity of the camera response. The calB source is reflected from the mirrors on to the camera to monitor the combined stability of the mirror reflectivity and camera gain. Light from the C source illuminates Tyvec targets on the inside of the telescope doors, then goes through the aperture towards the mirror and finally to the camera. The C light source includes 5 narrow band interference filters at wavelengths of 330 nm, 350 nm, 370 nm, 390 nm and 410 nm. This light source monitors the end-to-end stability of the full telescopes at all 5 wavelengths.

The overall stability of the camera gain, as well as pixel to pixel variation in relative gain, is better than 5%. The total uncertainties are kept below 10%. Further details on the instruments and procedures can be found in [118].

4.1.3 Atmospheric models and monitoring devices

The knowledge of efficiency of fluorescence light production and atmospheric transmission is crucial for the determination of the shower parameters. Efforts aiming to improve the accuracy on laboratory measurements of the main variables connected with the fluorescence emission are ongoing. An accurate characterization of the detection volume in terms of aerosol content, presence of clouds, suspended dust and smoke, is needed. Atmospheric conditions can vary on short time-scales thus requiring a dedicated set of monitoring routines, see [117].

Different devices have been developed in order to study in detail the Auger "atmospheric calorimeter". Redundant information allows cross-checks and provides a better understanding of the uncertainties in data reconstruction.

Atmospheric profile models

To derive realistic models of the atmosphere, campaigns of meteorological radio soundings were performed at the Auger site. Helium filled balloons equipped with radiosondes recorded measurements of temperature, air pressure and relative humidity as a function of altitude. Average seasonal and monthly models have been derived.

Fig. 4.4, left panel, shows the difference between average seasonal profiles, obtained from the measurements in the Auger site, and US Standard atmospheric model. The right panel is the impact on fluorescence yield calculated assuming the seasonal models again compared to US Standard.

The impact on the shower development and the fluorescence production efficiency, directly affecting mass sensitivity and energy reconstruction, has been discussed in detail in [88] [89].

Central Laser Facility

The central laser facility (CLF) [58] is located in the middle of the Pierre Auger Observatory SD array, at distances that range from 26 to 39 km from the FDs. The CLF is equipped with a steerable 355 nm laser, producing pulses with a width of 7ns and a maximum energy of around 7 mJ.

Its main purpose is to measure the aerosol content of the atmosphere. The intensity of

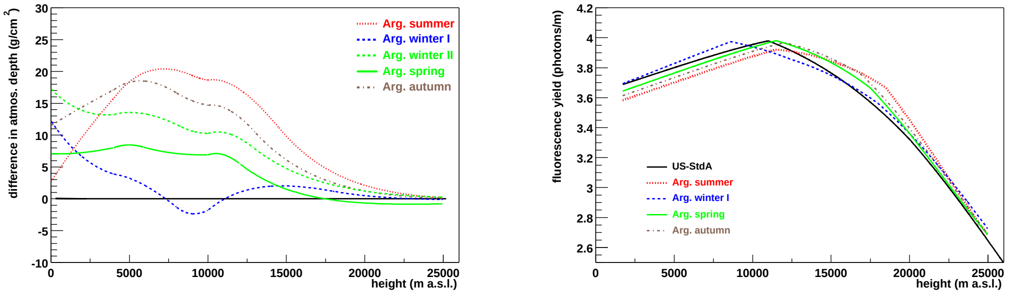

Figure 4.4: Left: differences in the average seasonal atmospheric depth profiles of Malargüecompared to US Standard, from [88]. Right: fluorescence yield profiles for a 0.85 MeV electron with vertical incidence for realistic atmospheric models compared to US Standard atmosphere, from [89].

light scattered from the beam at each heigth can be used to measure the aerosol attenuation from the beam to the FDs providing a measurement of vertical aerosol optical depth (VAOD) as a function of altitude.

Shots can be steered in any direction in the sky to study the response of FD detector in different geometry and energy configurations. Moreover a fraction of the laser light can be injected via optical fibers into a nearby SD tank allowing systematic studies of the hybrid geometry reconstruction accuracy, see for instance [4].

Horizontal Attenuation Monitors

The horizontal attenuation monitors (HAMs) measure the horizontal attenuation length as a function of wavelenght. The HAM system consists of a high intensity discharge lamp, located at the Coihueco FD building, and a receiver CCD located at the Los Leones FD eye, about 45 km away.

The light sources emit a broad spectrum of wavelengths including the $300 \div 400$ nm range where the FDs are sensitive. A filter wheel in front of the CCD allows monitoring the aerosol extinction coefficient at five different wavelengths. To monitor time variations, the measurement of the horizontal attenuation length at these wavelengths is performed hourly during FD operation.

Aerosol Phase Function Monitors

The aerosol phase function monitors (APF) [28] are designed to measure the aerosol differential scattering cross-section. Two of them are located several km from the FD building at Coihueco and Los Morados sites. The measurement is made by firing a horizontal, collimated beam of light from a xenon flash lamp across the field of view of an FD eye. The parameters can be determined simply by fitting the horizontal light tracks recorded by the FD, which contain a wide range of light scattering angles from the beam ($30° \div 150°$ in azimuth).

APFs include narrow band filters to monitor the wavelength dependence of the scattering cross section.

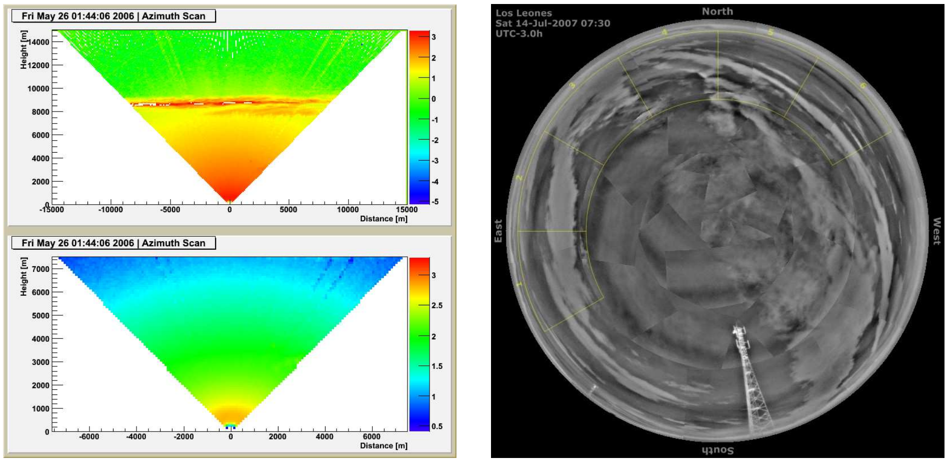

Figure 4.5: Left: scattering LIDAR systems meant for measuring the extinction length can reveal cloud layers above the FD telescopes, from [122]. Right: cloud camera mosaic pictures arranged in a 360° view around the FD telescopes, from [123].

Back-scatter LIDARs

Elastic back-scatter LIDAR stations are located near each of the FD sites. Three of them are already in operation, the fourth is currently being built at the Loma Amarilla FD site. Each LIDAR station uses pulsed 351 nm lasers operating hourly at 333 Hz, in fully steerable geometry configuration. Three parabolic mirrors focus the back-scattered signals on photomultiplier tubes. Thus the measurement of the extinction coefficients and VAOD are performed independently from the CLF, and can be cross correlated.
The station at Los Leones also includes a Raman lidar test system, detecting aerosols and the relative concentration of N_2 and O_2 in the atmosphere. Moreover the LIDAR is capable to detect cloud layers, which create significant echoes in the back-scattered light signal. An example of a continuous scan revealing a cloud layer at 3.5 km altitude over the station is shown in Fig. 4.5, left panel. Data is available for the collaboration at [122].

Cloud monitors

Clouds can have very large optical depths and irregular shapes, thus they may have a dramatic and unpredictable effect on the scattering and transmission properties of the atmosphere. Thus, to guarantee high data quality, detailed all-sky coverage maps are necessary during regular data taking operations.
Since clouds radiate strongly in the infrared it is possible to detect them, against a much weaker clear sky background. By accurate cross checks with other devices it is then possible to exclude cloud disturbance on an event-by-event basis. The *cloud cameras*, mounted at three of the four FD telescopes, consist of infrared digital cameras with spectral range between 7 and 14 μm. The cameras, with a FOV of 45° × 35°, are on steerable mounts so that they can survey the entire sky and generate a full picture every 15 minutes [43]. These mosaics are available at [123].

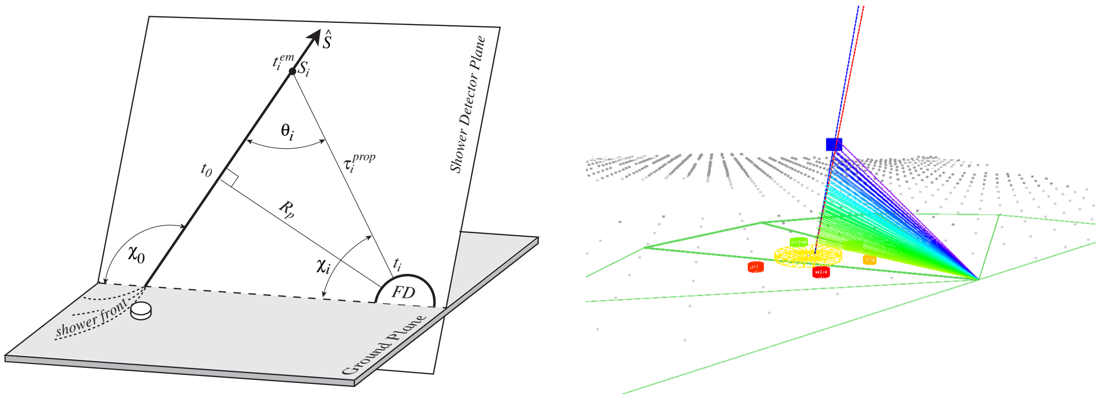

Figure 4.6: Left: illustration of the hybrid geometrical reconstruction technique and definition of geometrical parameters, from [93]. Right: 3D display [148] of a real event in a similar geometric configuration. The FD pixel directions and the triggered SD tanks are shown: color code reflects trigger time, size of the tank markers the particle density.

4.2 Details of the hybrid reconstruction

Fig. 4.6 is an illustration of the hybrid geometrical reconstruction technique. The shower detector plane (SDP) is defined as the best fit to the pattern of triggered pixels in the fluorescence detector camera. The geometry is completely determined by tree parameters: the impact parameter R$_p$, i.e. distance of closest approach to FD, the time t$_0$ at which that distance is reached, and the angle χ_0 between shower axis and horizontal vector.
The shower axis is determined testing the derived prediction for the arrival time at each detector component with each trial geometry. Differences between measured and predicted times are weighted using their corresponding squared uncertainties, summed to construct a χ^2. Minimising the value of the χ^2 yields the reconstructed shower axis parameters.
The light is detected at the ith pixel at the time t$_i$ determined as:

$$t_i = t_0 + \frac{R_p}{c} \tan\left[\frac{(\chi_0 - \chi_i)}{2}\right] , \tag{4.1}$$

where χ_i is the direction of the ith pixel within the SDP. This formula assumes instantaneous emission of fluorescence light and straight line propagation with vacuum speed of light. The impact of a more realistic treatment of the emission and propagation of fluorescence light on the geometry reconstruction has been recently discussed in [94].
The accuracy of the monocular reconstruction is limited when the measured angular speed $d\chi/dt$ does not change much over the observed track length. This happens especially for short tracks resulting in a small curvature in the functional form of Eq. 4.1. In this case the three parameters fit (R_p, χ_0, t_0) gives a large number of possible axis configurations. This is shown in Fig. 4.7 left panel, for the monocular reconstruction (red ellipse), not only the uncertainties in R_p and χ_0 are large, but also they are strongly correlated. The geometry uncertainties affect directly the reconstruction of the other shower parameters, especially the primary energy. Using the timing information of the tanks allows to break this degeneracy and critically improve the detector resolution, as is evident from the plot (blue ellipse). In Fig. 4.7 right panel, the correlation between trigger time and pointing

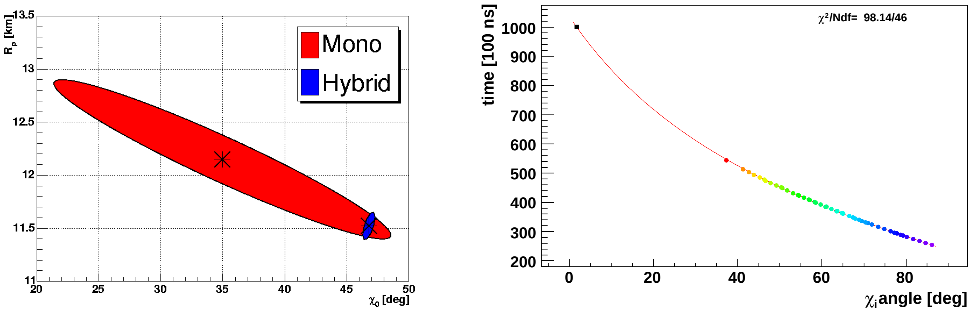

Figure 4.7: Left: FD monocular reconstruction uncertainty (red) versus hybrid uncertainty (blue). Using SD timing information constraints the fit breaking the degeneracy in the FD monocular reconstruction, from [98]. Right: for a real event example, correlation of the arrival time of the light at each triggered FD pixel with the pixel pointing direction within the shower-detector plane. The color code reflects pixel trigger time, the SD tank with greatest signal also included in the reconstruction (black filled square).

direction within the shower-detector plane for the triggered pixels for a real event case is shown. Information from the SD tank with greatest signal is included in the time fit (black filled square). Other tanks and pixels have been rejected (open squares and circles) The accuracy of the hybrid geometry reconstruction can be checked by means of CLF laser shots, which trigger the FD and the nearest SD tank. Results from this measurement are shown in Fig. 4.8, from [160]. The accuracy of the shower axis angular reconstruction is shown in left panel for the monocular FD and for FD-Hybrid fit, obtained adding the information from the SD tank (blue shaded area). The resolution of the impact parameter is shown in the right panel. The critical improvement of the hybrid mode, with respect to FD only, is evident.

The precise determination of the the event geometry, allows, after having applied the calibration constants to the FADC traces recorded in the FD pixels, to perform an accurate

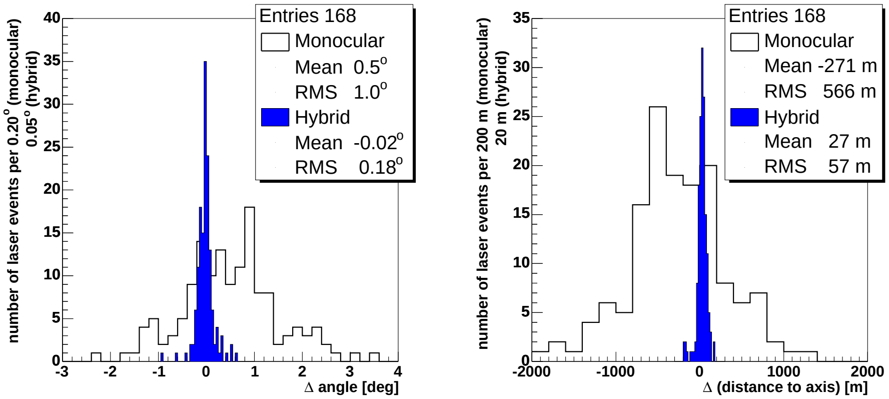

Figure 4.8: Resolution in shower axis angle reconstructed for the FD only and for the FD-Hybrid (blue shaded area). Right: resolution in the shower impact parameter. From [160].

conversion of the light flux at the aperture into light emitted at shower track. In this calculation the atmospheric profile models, the scattering models and the air fluorescence light efficiency have to be taken into account.

As discussed in section 2.3.1 the amount of fluorescence light emitted at the track element, is proportional to the energy dissipated by the charged particles in that track. Fitting the measured longitudinal profile, is then possible to derive the electromagnetic energy of the primary particle.

As we said, the correction for the "invisible" energy carried by high-energy muons and neutrinos must be applied to obtain the primary total energy. This correction requires assumptions about the primary mass and introduces a slight dependence on the hadronic interaction model. Typical values for the average correction are $\sim 12\%$, assuming a mixed composition (50 % protons and 50% iron nuclei) at energies $\sim 10^{19}$ eV. The discrepancies between different models are however below $\pm 5\%$.

The model dependencies thus affect the FD "calorimetric" energy measurement much less with respect to array-based measurements, that rely on shower simulations. Hybrid data, which represent a 10% of the total, can be used to calibrate the SD energy estimator, S_{38}, namely the density at 1000 m from the core, normalized with the method of the constant intensity cut. Assuming an isotropic flux, the new parameter S_{38} may be regarded as the S(1000) the shower would have produced arriving from a zenith $\theta = 38^\circ$ [133].

In Fig. 4.9, left panel, the correlation between S_{38} and the FD energy measurement is shown for a set of 387 high quality hybrid events. The fitted line gives an empirical rule for assigning energies, in eV, based on S_{38} in VEM: $E_{FD} = A + B \cdot \ln S_{38}$. The best fit gives $A = 17.08 \pm 0.03$, $B = 1.13 \pm 0.02$. The relative residuals $(E_{SD} - E_{FD})/E_{FD}$ are plotted in Fig. 4.9, right panel, from [133].

Tab. 4.1 summarises the systematic uncertainties in the FD energy determination, which, summed in quadrature, give a total uncertainty of 22% [47]. Efforts to reduce the main terms, namely the fluorescence yield and the absolute calibration, and to improve the reconstruction algorithm are underway.

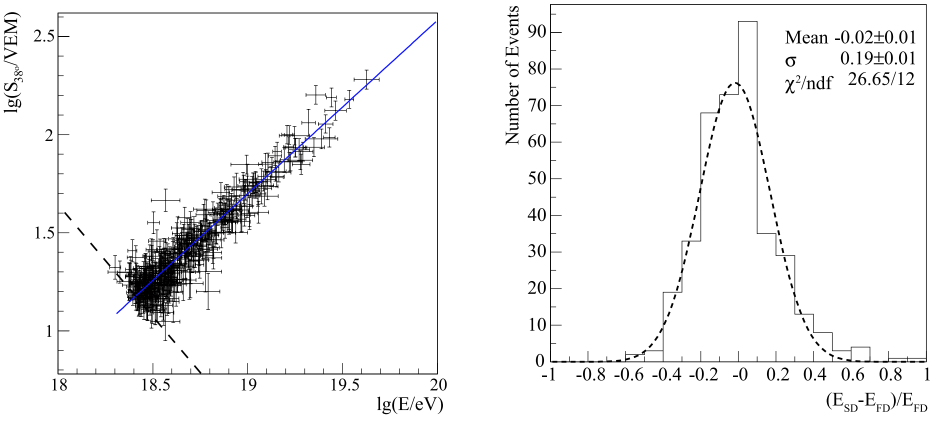

Figure 4.9: Left: correlation between shower energy measured from the FD as a function of the ground parameter S_{38}, determined by the SD, from [133]. Right: current estimates of the systematic uncertainties affecting energy reconstruction.

Table 4.1: Current estimates of the systematic uncertainties affecting energy reconstruction. Values from [47].

	uncertainty %		uncertainty %
fluorescence yield	14	atmosphere (P,T,humidity)	7
detector calibration	9.5	atmosphere (attenuation)	4
geometric reconstruction	10	missing energy	4
total			**22**

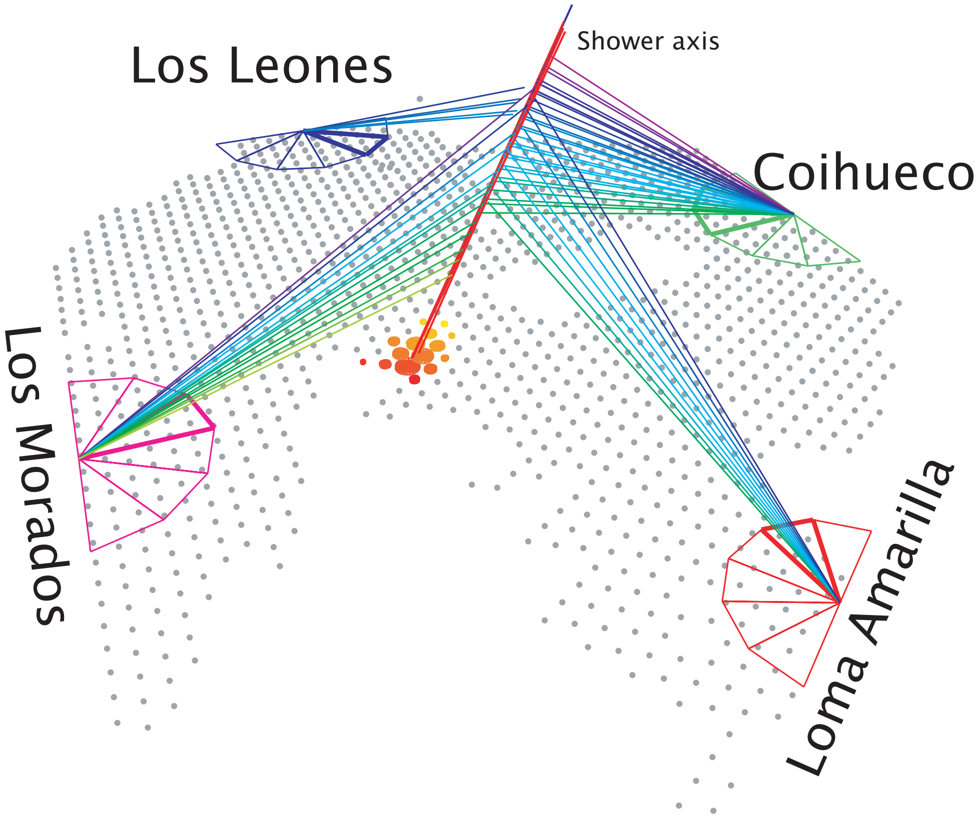

Figure 4.10: The first 4-fold event recorded on the 21st May 2007, from all the four FD telescopes together with the SD array. The event, coming at zenith angle ∼ 65°, has a reconstructed energy of $\sim 10^{19}$ eV, a X_{max} of 790 $\mathrm{g\,cm^{-2}}$ [99]. Graphics from [94].

4.3 Photomultipliers qualification tests

As described in section 4.1.2 the optical system of the Pierre Auger Observatory employs, for each fluorescence telescope, a camera which mounts 440 photomultiplier tubes (PMTs). In total, about 11 000 of these modules, had to be delivered to the PAO site. Before being shipped to Argentina, the PMTs were mounted with the head electronics and had to pass a strict test following the requirements described in [114].
About 6100 out of the total production, plus additional spares, have been tested in Wuppertal with a dedicated setup, the others in a similar setup in Rome [121]. The description of the test system and the results of our work were presented to the collaboration in [23] and published in [24].

Requirements and setup

Because of the large number of PMTs to be tested the measurement procedure has to be highly automatized and focused on the main requirements:

- identification of dead and unstable modules
- measurement of the PMT gain as a function of high voltage (HV)
- classification of the PMTs according to gain classes
- test of linearity of the response for different light intensities
- test of wavelength dependence of the PMT response.

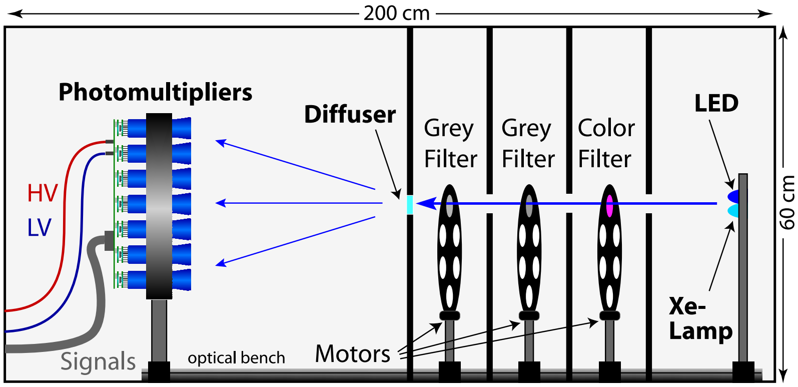

Figure 4.11: Sketch of the PMT test setup. On the left a metal structure hosts 37 PMTs and the low and high voltage supply boards, in the central part the attenuation and wavelength filters, on the right the light sources (LED and Xenon lamp).

In Fig. 4.11 a sketch of the test setup is shown. A black box of ~ 2 m length hosts the optical devices, the attenuation and wavelength filters and the light sources. At each run 37 PMTs are tested, four PMTs are taken as the *reference PMTs* and are measured at the same positions in each run. Knowing the response of these PMTs, changes in the setup

can be tracked and accounted for in the analysis. The other 33 positions are filled with the PMTs which have to be tested. They share one HV supply unit while the reference PMTs are operated with an independent HV supply driven by the test software.
Neutral density attenuation filters are used for a controlled reduction of the light intensity over 3 orders of magnitude. These filters are mounted on two remote controlled wheels, which allows for different combinations. Two interference filters transmit light in a narrow wavelength interval (10 nm wide) around 337 nm and 390 nm allowing measurements of the spectral response of the PMT photocathode.
Two different light sources have been used for the measurements, with pulses which emulate the typical signals from real cosmic ray showers. The first is a blue-light emitting diode (LED), at 470 nm, providing signals with a width of about 1.5 μs and variable repetition rate. The second is a Xenon flash lamp with a wide range of wavelengths down to 240 nm. The width of the signal is about 2 μs.
The PMT response is analyzed by integrating the charge of the digitized signals. The digitization with FADCs provided the opportunity to implement a highly automated on-line monitoring and analysis of the PMT response, e.g. checking for saturation, implementation of dynamic integration gates, and automatic determination of the baseline used for pedestal subtraction. The DAQ system also allows remote control of the HV power supply and the motors which rotate the wheels on which the optical filters are mounted.
The data acquisition (DAQ) is connected via a VME/PCI bridge to a PC running a Linux. The PMT signals are digitized by FADCs running at a frequency of 100 MHz and a resolution of 12 bit. The system has been adapted from [157].
The PMT and head electronics serial numbers are scanned along with the position in the structure. This information together with test results is stored in a local MySQL database.

Measurements and results

For all the measurements we have used the integrated charge Q to quantify the PMT response. To extract Q the baseline must be subtracted and the amplitudes summed up in an optimal time window which depend on the signal shape. The time window is chosen 5 μs – 7.1 μs for the LED and 4 μs – 10 μs for the Xenon lamp.
The baseline is estimated by calculating the median of recorded amplitudes in the time range before the signal (between 0 μs and 3.5 μs). We found this estimation very stable against baseline noise.

Gain and high voltage classification

At the experimental site PMTs are typically operated at a gain of $\sim 10^5$. In the FD camera 10 groups of 44 PMTs are operated by the same high voltage (HV) module. In order to equalize the response and to minimize calibration corrections only PMTs of similar gain, at a given high voltage, should be connected to the same HV channel.
For the calibration of the PMT gains we measured the integrated charge response of the PMT for fixed light intensity as a function of the HV applied to the tube. For each unit the HV dependence of the measured charge was fitted with the power law:

$$G = K \cdot (HV)^{\alpha} \ . \tag{4.2}$$

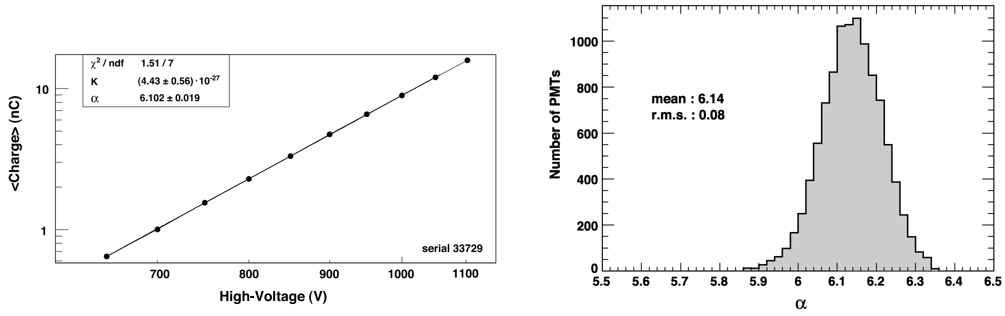

Figure 4.12: Left: example of a measurement of the HV dependence of the gain. Errors of the data points, calculated as $RMS(Q)/\sqrt{N_{evts}}$, are smaller than the marker size. Right: distribution of the measured parameter α (see equation 4.2).

An example of the measurement and fit is shown in Fig. 4.12, left panel. The errors of K and α are only approximations since we neglect the correlation of the parameters. However, they are generally small and their absolute value is of no importance for these classification tests.

The distribution of the power index α is shown in Fig. 4.12, right panel. The mean value is close to 6.1, in agreement with the expectation from the manufacturer based on the known secondary emission coefficient of the dynodes. The spread is quite small with a RMS of the order of 1 %. The photomultiplier tubes were pre-classified by the factory into ten HV classes, identified by the letters A to J, according to the value of the HV needed for obtaining the electron gain $G = 10^5$. A table summarising the class definition according to high voltage interval is shown in Fig. 4.13, left panel.

From our measurement we get the nominal voltage to reach an effective gain of 10^5, which is not identical to the electron gain determined at the factory, but takes into account differences of the quantum efficiency, the collection efficiency, the sensitive photocathode area, and the HE unit.

gain class	HV range	mean HV%
A	850-876	863
B	876-903	890
C	903-931	917
D	931-959	945
E	959-989	974
F	989-1019	1004
G	1019-1050	1035
H	1050-1083	1067
I	1083-1116	1100
J	1116-1150	1133

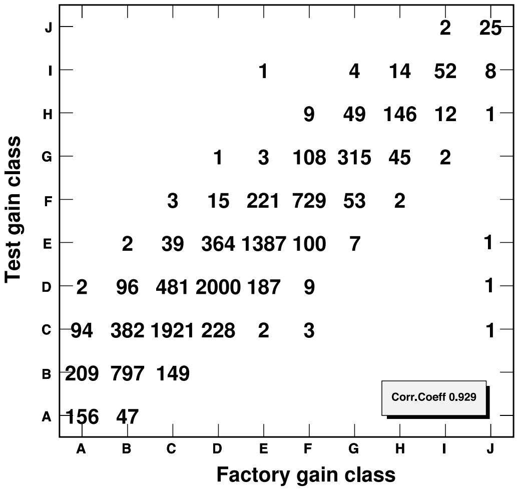

Figure 4.13: Left: table of the gain class definitions. Right: distribution of the PMTs in the corresponding gain classes, the acceptance test results versus the factory results.

However, we find a good overall correlation between the two classifications, even if there is a substantial migration of PMTs into other gain classes, thus showing the importance of the acceptance tests. A few modules are found with a strong deviation from the factory result, see Fig. 4.13, right panel.

A small dependence of the parameter α on the gain class has been measured. Gain classes designated with a higher letter correspond to PMTs of smaller gain and therefore larger operation voltage, and tend to have smaller values of α, reflecting the fact that for those tubes the average secondary emission coefficient is slightly smaller.

Linearity response

In order to test the proportionality between the input light intensity and the PMT response, we measure the charge of pulses sent by the blue LED traversing different combinations of the attenuation filters. For each run the PMTs are operated with a high voltage set to the mean value of the factory gain class.

The maximum value of the signal obtained without attenuation is chosen to correspond to the largest detectable signals. Data have been fitted with a power law, $\langle Q \rangle = p_0 \cdot T^{\beta}$. The distribution of the resulting power index β from the fit is shown in Fig. 4.14, left panel. The values are consistent with $\beta = 1$ and the fits have $\chi^2/d.o.f. \sim 1$.

The PMTs show an excellent linear overall behavior. No significant deviations from linearity have been observed when testing the most critical high-amplitude response over two orders of magnitude.

Wavelength response

The sensitivity of the photocathode at different wavelengths is tested by measuring the mean collected charge using pulses from the Xenon lamp, with two narrow band filters, $337 \pm 10\,\text{nm}$ and $390 \pm 10\,\text{nm}$. The mean response of the PMTs for each wavelength filter is normalised to the charge measured without filter, Q_{white}.

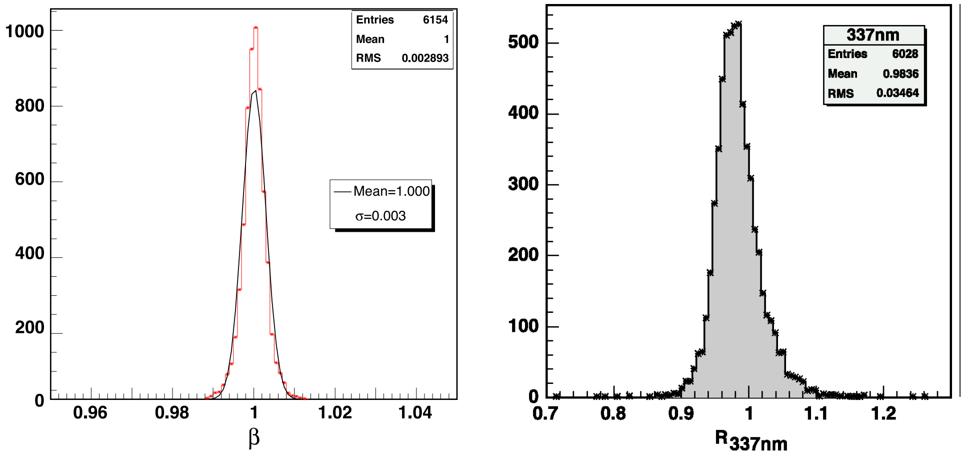

Figure 4.14: Left: measurement of the linearity of the PMT response; distribution of the power law index β, obtained fitting data with the function $\langle Q \rangle = p_0 \cdot T^{\beta}$. Right: measurement of the wavelength response; distribution of the spectral R_{337}.

In order to account for the fluctuations in the intensity of the Xenon lamp and its wavelength spectrum, we normalise each measurement first to the mean response of the reference PMTs. This cancels out also time dependent drifts of the setup. We define as key parameter the following double ratio:

$$R_\lambda \equiv \frac{< Q_\lambda > / < Q_\lambda^{ref} >}{< Q_{white} > / < Q_{white}^{ref} >} \ . \tag{4.3}$$

The resulting R_λ is computed for both wavelengths and each measured PMT. Strong deviations from unity indicate a drop or an increase of the cathode sensitivity for this specific wavelength (relative to a normal response given by the reference PMTs).
Fig. 4.14, right panel, shows the distribution of $R_{\lambda=337\,\mathrm{nm}}$. The deviations from unity have an RMS of less than $\sim 3.5\,\%$ and the largest observed deviation is $28\,\%$.

Stability of the measurements

Checking the stability of the setup is essential, since the production and test phase was spread over more than one year. Relative changes are monitored by measuring changes in the response of the reference PMTs. In addition we repeated measurements of the same set of PMTs at different times, and also at different positions in the setup. The spread of the nominal HV during the different gain calibration of the same PMTs is found to be less than 3 V, which corresponds to an uncertainty in gain of about $2\,\%$.
Changes in the absolute response of the reference tubes give information about the overall stability of the chain, including light sources, reference PMT+HE themselves, the data acquisition, and environmental effects. The RMS spread of the HV measurement is found less than $2\,\%$.

Failure rate

During the Wuppertal acceptance tests 9 PMTs over 6100 have been rejected, 5 of which have been recuperated replacing the head electronics base. Two others had small factory defects and two no photocatode layer. The total number of rejected units was 14 over 11 000, which means a very small rejection rate of $\sim 0.13\%$.

Chapter 5

Performance of the Fluorescence Detector reconstruction algorithm

This chapter is focused on the performance of the Fluorescence Detector (FD) reconstruction algorithm and its accuracy. A dedicated study, at different cut levels, has been performed in order to quantify the detector resolution and systematics and to identify and avoid possible biases. The detector trigger efficiency as a function of energy and distance has been investigated. The monocular geometry resolution is derived, results are in agreement with a previous study [109]. A realistic estimate of the hybrid X_{max} and energy resolution is provided setting the geometry to the true value. The sensitivity of the reconstructed energy to the atmospheric properties has also been investigated by assuming two different atmospheres.

The extension of the reconstruction capabilities to the highest energies covered by the Fluorescence Detector dynamic range has been achieved after a detailed study of the saturation region (energy-distance). A new technique has been implemented to recover events eventually exceeding the signal range of the high gain channels improving the performance of the full simulation-reconstruction chain at the highest energies.

A detailed description of the first Fluorescence Detector simulation program is given in [125]; the reconstruction was performed using the official $\overline{\text{Off}}\underline{\text{line}}$ [10] software. Details of the simulation reconstruction chain have been given in [104].

The results of this studies have been published in [108] and [136], presented at two collaboration meetings and are part of the Pierre Auger Collaboration technical information [137][138].

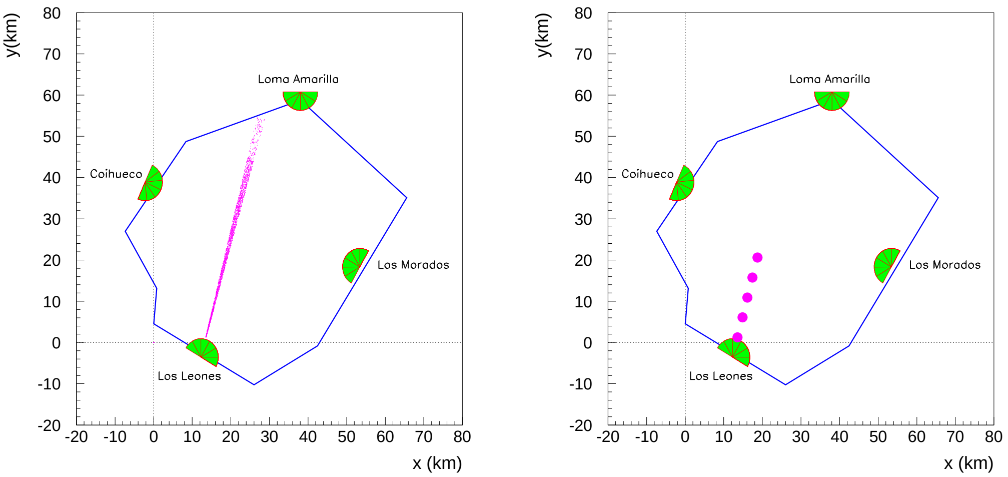

Figure 5.1: Sketch of the Pierre Auger Observatory showing the core positions of the simulated showers. Left plot for the trigger efficiency and resolution study (sample 1) , right plot for the saturation region study (sample 2).

5.1 Generation parameters

A large sample of fully simulated CORSIKA showers [71], taken from the shower database generated in the Lyon computing center for simulation studies, has been used for these studies. The shower sample consists of 4400 proton showers and 4150 iron showers with zenith angles of 0°, 18°, 26°, 37°, 45°, 60° and energies ranging between $10^{17.5}$ and 10^{21} eV in steps of 0.25 or 0.5 in the logarithmic scale.

For the trigger efficiency and detector resolution study the CORSIKA showers have been simulated in a slice of 2° in the field of view of Bay4 (Los Leones Eye), with uniformly distributed core distances ranging from 5 to 60 km (sample 1).

The maximum distance of the generated impact points was to chosen to depend on the shower energy as shown in Tab. 5.1. This choice is not reflecting the real events distribution but minimizes the inefficiency affecting low energy showers landing far away from the telescope i.e. with a negligible probability of being triggered.

Table 5.1: Settings for an energy dependent core generation (sample 1).

zone #	Log(Energy/eV)	R_{max} [km]
1	17.5	15
2	18	32
3	18.5	50
4	>19	60

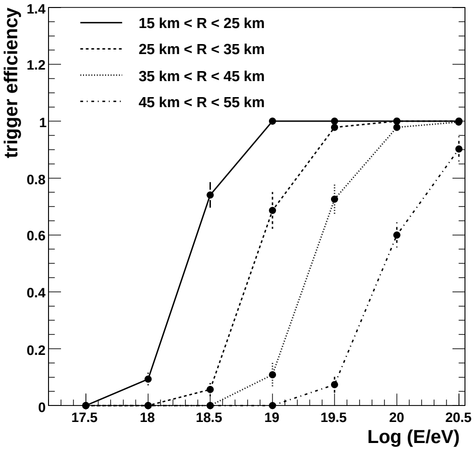

Figure 5.2: Trigger efficiency as a function of energy for increasing core distances ranges (zenith angles merged). The trigger probability is 100% up to a distance of 25 km for showers with energy of 10^{19} eV.

Care has been taken to exclude border effects by setting R_{max} where the trigger efficiency has already dropped to zero. For a detailed study of the detector response at the highest energies, characterizing the FD saturation region, the proton set has been re-sampled at fixed core distances of 5, 10, 15, 20 and 25 km from the eye, for a total of 22000 showers (sample 2).

A sketch of the Pierre Auger Observatory, showing the core positions of the simulated showers along with the four FD buildings and the SD array area, is given for the two different samples in Fig. 5.1.

5.2 Trigger efficiency

The Fluorescence Detector monocular trigger efficiency has been studied as a function of shower energy, zenith angle and core distance. The only requirement at this level is a second level trigger flag in one or more of the 6 bays of the Los Leones telescope. In Fig. 5.2 the trigger efficiency is plotted for protons as a function of energy for increasing core distance ranges (zenith angles merged). The trigger efficiency is 100% up to a distance of 25 km for showers with energy of 10^{19} eV.

Three dimensional contour plots for the different zenith angles bins (0°, 26°, 45°, and 60°) are given in Fig. 5.3. The trigger probability increases, as expected, for more inclined showers which fall in the field of view of more than one fluorescence telescope.

A detailed calculation of the fluorescence detector aperture for different detector configurations and using analytical shower profiles is given in [111].

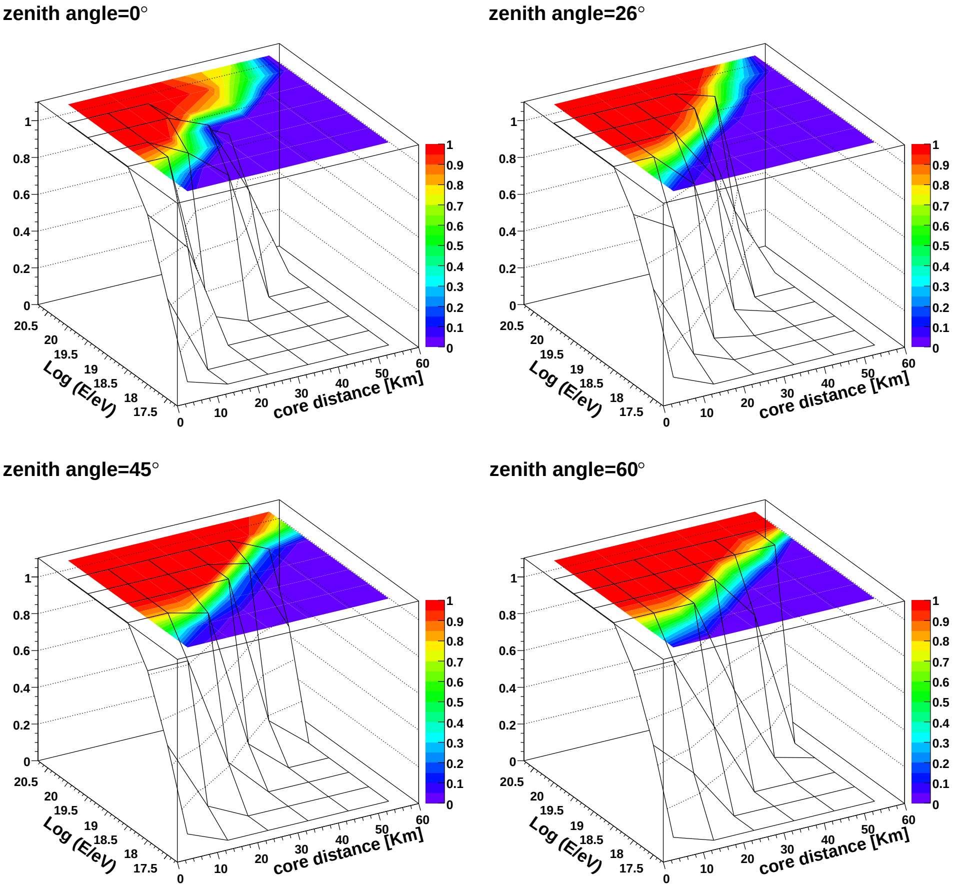
zenith angle=0°

zenith angle=26°

zenith angle=45°

zenith angle=60°

Figure 5.3: Trigger efficiency as a function of energy and core distance for different zenith angles (0°, 26°, 45°, and 60°). The trigger probability increases, as expected, for more inclined showers, as they may fall in the field of view of more than one fluorescence telescope.

5.3 Monocular geometry resolution

The Fluorescence Detector monocular resolution in the geometry variables (SDP angles, axis angles, R_{core}, R_p, χ_0) has been investigated. The very good accuracy in the determination of the shower-detector plane has been verified; the resolution in the axis space angle quantified. The quality requirements at geometry reconstruction level are the following:

- minimum number of triggered pixels = 10,
- successful SDP fit with $\chi^2/Ndof$ smaller than 5,
- successful time fit with $\chi^2/Ndof$ smaller than 5.

In Fig. 5.4 the residuals (Rec-MC) in the SDP angles are plotted, the RMS values give an estimate of the FD monocular resolution. Fig. 5.5 shows the resolution in the impact parameter R_p (left) and in core distance (right). In Fig. 5.6 the resolutions in axis space angle (left), and in χ_0 (right) are given. The uncertainty in the FD time fit is responsible for the large tails in the residuals distributions. In Tab. 5.2 the overall resolutions are summarized.

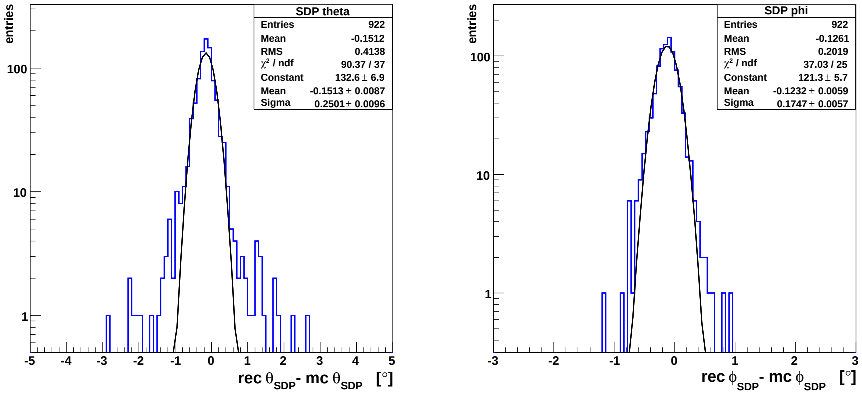

Figure 5.4: FD monocular resolution in the SDP variables: left SDP zenith angle, right SDP azimuthal angle.

5.4 X_{max} and energy resolution

The characteristics of the simulation sample allow a specific study of the energy residual distribution and its resolution as a function of energy, zenith angle and core distance. The FD monocular X_{max} and energy resolutions have been estimated and compared with the case of known fixed shower geometry.

Setting the geometry to the true value can provide a realistic estimate of the energy resolution for the hybrid mode. This assumption is justified by the argument that hybrid reconstruction benefits from a more accurate shower geometry with respect to the monocular fluorescence reconstruction. A dedicated module has been developed to by-pass the

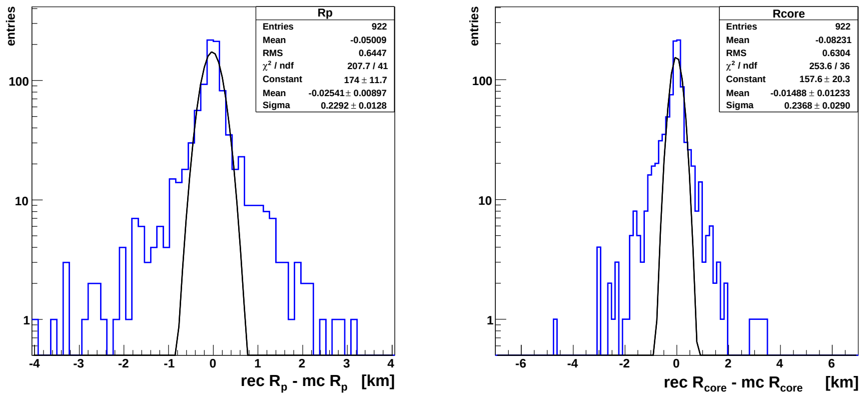

Figure 5.5: FD monocular resolution in $\mathrm{R_p}$ (left) and core distance (right).

geometry reconstruction modules, feeding the chain with the true Monte Carlo values. The quality requirements at this stage are the following:

- detected longitudinal profile wider than 200 $\mathrm{g\,cm^{-2}}$,
- successful Gaisser-Hillas fit with $\chi^2/Ndof \leq 5$,
- observed X_{max} .

Especially the last quality cut is very strict (efficiency $\sim 40\%$) but necessary to minimize the uncertainties due to the longitudinal shower profile fit. The impact of the adopted cuts on the detector aperture will be discussed later.

Fig. 5.7 shows the residual distribution of the reconstructed depth at shower maximum ($\mathrm{X}_{max\ rec}$ - $\mathrm{X}_{max\ MC}$) for proton (black line, RMS=25 $\mathrm{g\,cm^{-2}}$) and iron (red dot-dashed

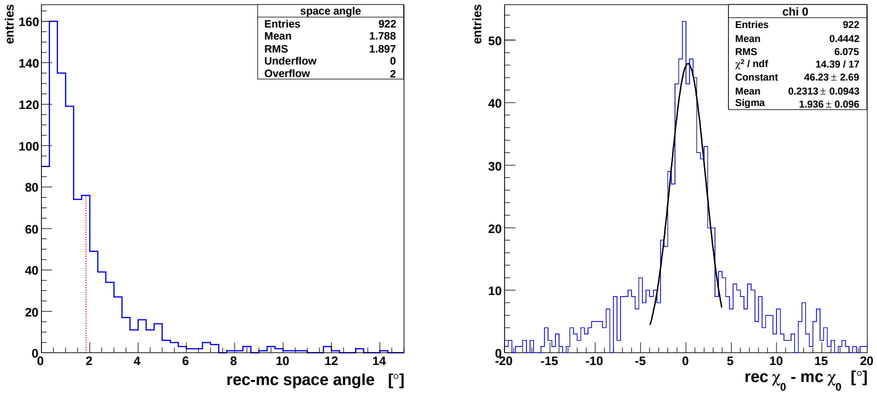

Figure 5.6: FD monocular resolution in the axis variables: left panel axis space angle, right panel χ_0.

Table 5.2: Summary of the overall FD monocular resolutions in the geometric variables (sample 1).

angles [°]	mean	RMS
θ_{SDP}	-0.2	0.4
ϕ_{SDP}	-0.1	0.2
axis		1.9 (68%)
χ_0	0.4	6.1

distances [km]	mean	RMS
R_p	-0.07	0.64
R_{core}	-0.09	0.63

line, RMS=22 $\mathrm{g\,cm^{-2}}$). Fig. 5.8 shows the relative residual of the reconstructed energy $((E_{rec} - E_{MC})/E_{MC})$, for events with fixed geometry (blue line) and with reconstructed geometry (red dot-dashed line). The energy resolution improves from 11% to 9% in terms of RMS and the number of selected events increases by a factor 2 if the geometry is set to the true MC value. This demonstrates how much the performance of the Auger Observatory can improve when operating in hybrid mode.

The mean and RMS of the residual for the case of fixed geometry is shown in Fig. 5.9 as a function of zenith angle (top), core distance (middle) and true energy (bottom). Error bars include statistical fluctuations only. The mean residual is about 5% for vertical showers and for low energy, elsewhere better. The RMS has a stable average value of about 9% over the studied core distance and zenith angle range. It depends weakly on energy, improving with increasing energy, if one excludes the last energy bin, which will be discussed in the next section.

The energy resolution shown has been calculated for proton primaries and for a clean atmosphere (aerosol horizontal attenuation length at sea level of 24 km and scale height of 2 km). A test performed with a different atmosphere (aerosol horizontal attenuation length at sea level of 12.5 km and scale height of 2 km) shows that the energy resolution may degrade from 11% to 13% for the proton case, due to the larger geometry uncertainties.

In Tab. 5.3 the estimated energy and X_{max} resolutions are summarized.

Table 5.3: Summary of the FD monocular X_{max} and energy resolutions (sample 1). The right column contains the overall estimates for hybrid-like (bold), for FD monocular and in brackets for a worse atmosphere

	θ	R_{core}	MC_{ene}	overall RMS
X_{max} [$\mathrm{g\,cm^{-2}}$]	$23 \div 40$	$25 \div 46$	$20 \div 49$	**25**(p) **22**(Fe)
Energy [%]	$8 \div 10$	~ 9	$7 \div 11$	**9** 11 (13)

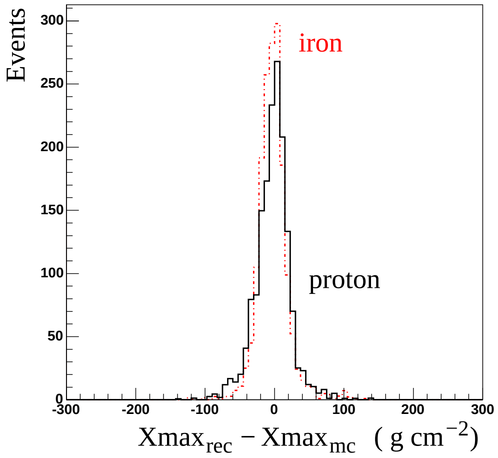

Figure 5.7: Residual distribution of the reconstructed depth at shower maximum (reconstructed X_{max} - MC X_{max}) for proton (black line, RMS=25 g cm^{-2}) and iron (red dot-dashed line, RMS=22 g cm^{-2}).

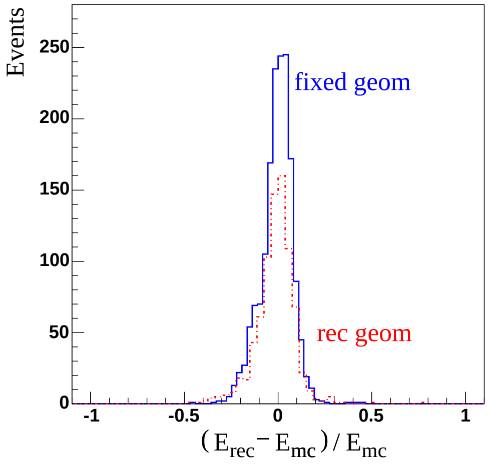

Figure 5.8: Energy relative residual $(E_{rec} - E_{MC})/E_{MC}$ for the simulated data sample with true geometry (blue line, 1607 events, RMS=9%) and reconstructed monocular geometry (red dot-dashed line, 798 events, RMS=11%).

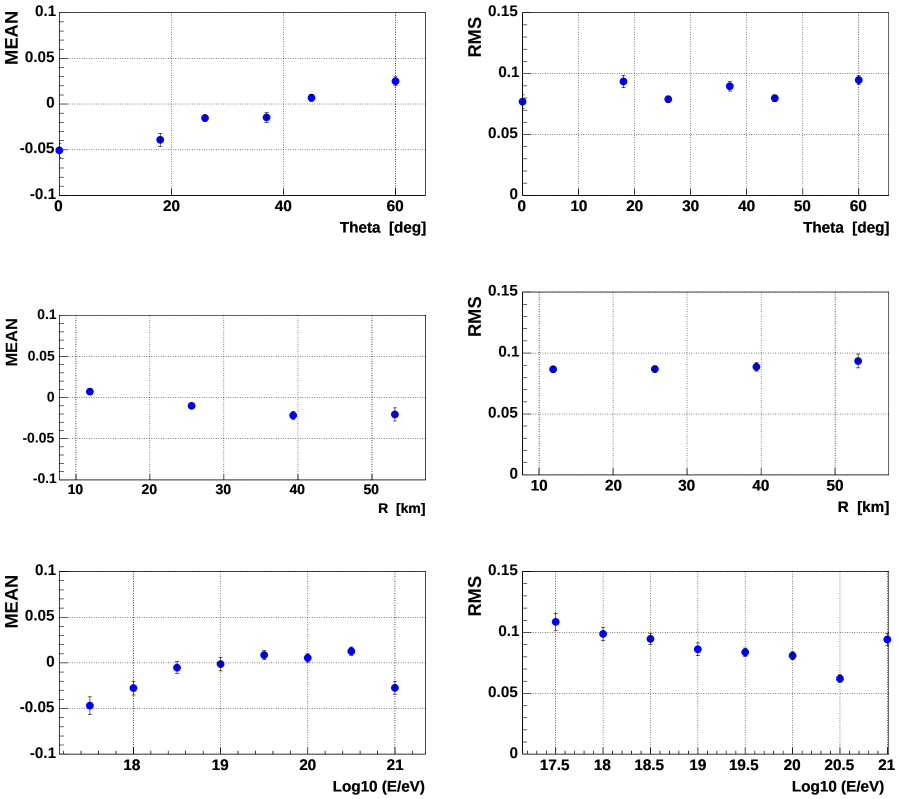

Figure 5.9: Energy residuals (left) and energy resolution (right) as a function of zenith angle (top), core distance (middle) and true energy (bottom).

5.5 Extension to the highest energies

As shown in Fig. 5.9, bottom left plot, the reconstruction at the highest energies, instead of being more precise as expected, is affected by an evident negative shift, i.e. energy underestimation. Moreover the RMS is deteriorated. Being able to reproduce the collected signal correctly, by means of accurate simulations, becomes crucial at these extreme energies especially for the Pierre Auger Observatory.

Two effects are responsible for the underestimation of shower energy in this range and are discussed in this section: the saturation of the high-gain channels and the inhomogeneity of light collection.

5.5.1 Saturation in the high gain channel

The description of the FD electronics has been given in Sec. 4.1.2; for further details on the Fluorescence Detector analog board (AB) see [114] [11]. A clever system adopting a readout with two different electronic gains, the high-gain or *normal* channel and the low-gain or *virtual* channel, has been designed to extend the dynamic range containing the costs of analog electronic components. For this work the writing and reading routines for simulation and reconstruction have been implemented and fully tested in our mass production chain. The results have been presented to the collaboration, published in the internal notes [137] [138] and the modules are now part of the official software repository.

In order to quantify the fraction of events saturating the high-gain channel and eventually the low-gain channel, we use here the sample 2, as defined in 5.1. A detailed explanation of the working principle and more details on the signal recovery module are given in App. A.

Simulations with different gain settings

Our aim is to study the effect of a change in the settings of the electronics gain on the FD reconstruction capabilities. We simulated firstly with a gain ratio corresponding to the nominal value of 32, then with an extreme value of 5 (corresponding to the resistive partition only) and finally we raised it to 20, which after this study we consider to be the minimum safe value for on-site operations.

Fig. 5.10 shows the fraction of events with at least one pixel with saturation of the normal (top) and of the virtual channel (bottom) in at least one time bin. A color contour plot and a text histogram are given on the left and on the right, respectively.

The fraction of saturated events already begins to be significant at short distances for an energy of 10^{19} eV and remains above 50% at higher energies with core distances increasing in steps of 5 km for each half decade in energy.

The nominal value for the gain ratio has been chosen based on the study given in [46] and adopted for the Pierre Auger design report, in order to cover the signal dynamic range avoiding saturation in the virtual channels even for events at the highest energies. Saturation in the normal channels occurs for a significant fraction of these events, but this is in most cases fully recoverable.

To lower the gain ratio by raising the virtual gain obviously doesn't affect the normal channel saturation phase space but it enlarges the virtual one. Fig. 5.11 shows the fraction of events with saturation in any single time bin of any virtual channel in a telescope. The gain ratio is set to 5 and to 20 in the top and in the bottom panels, respectively. With

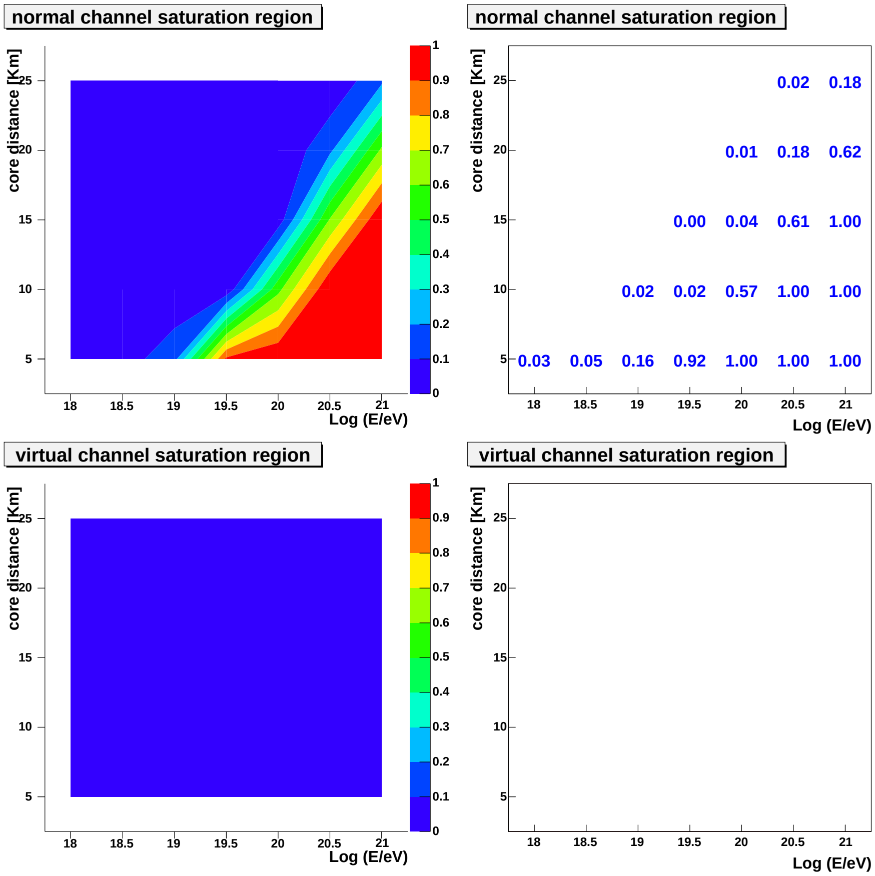

Figure 5.10: Fraction of events with at least one saturated time bin in the normal channel (top) and in the virtual channel (bottom). The gain ratio (normal gain / virtual gain) is set to the nominal value of 32.

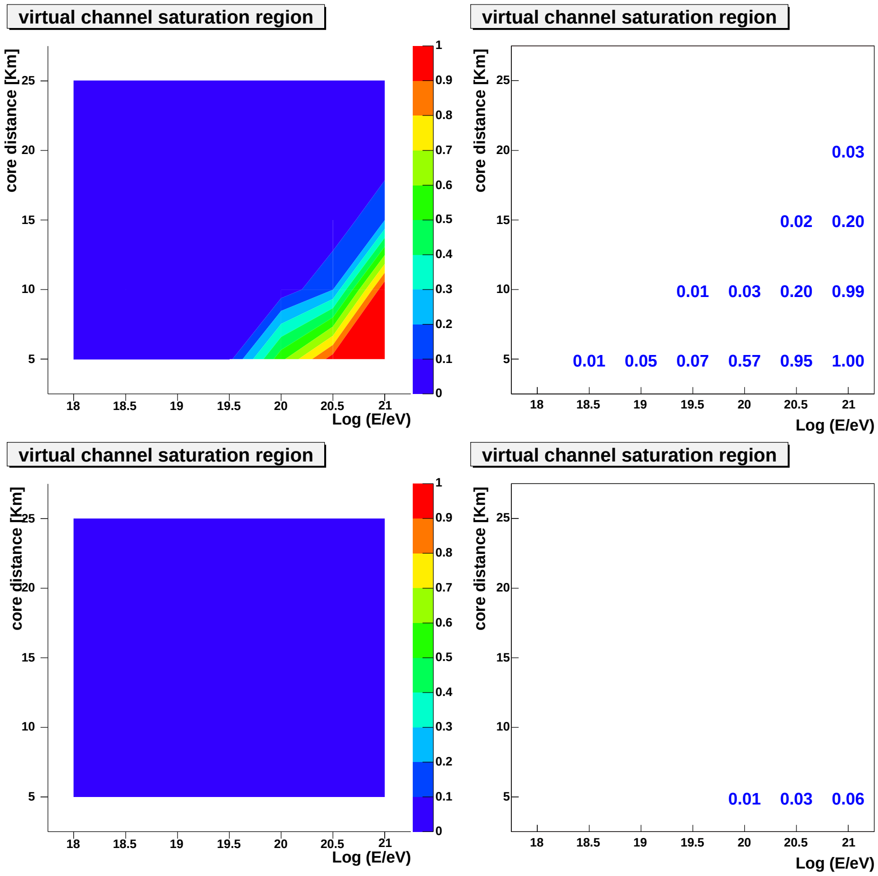

Figure 5.11: Fraction of events with at least one time bin with saturation in the virtual channel. The gain ratio is set to 5 (top) and 20 (bottom).

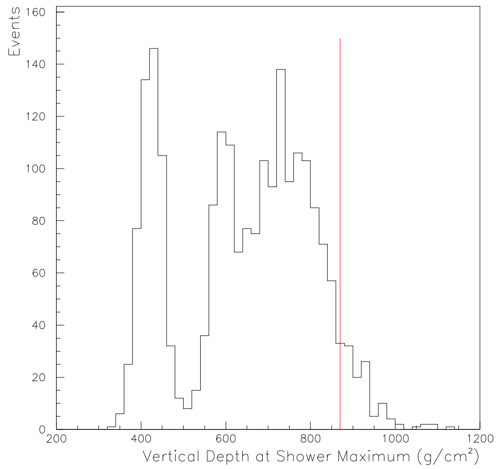

Figure 5.12: Distribution of vertical depth at shower maximum for the events with saturated virtual channel. The vertical red line gives the ground position in grammage at Auger altitude. The structure of the histogram reflects the zenith distribution of the simulated events.

a gain ratio of 5, saturation of virtual channel occurs for a fraction of events of about 20% at energy of $10^{20.5}$ eV and core distance of 10 km. With a gain ratio of 20, the fraction of lost events is reduced to less than 6% at any energy less then 10^{21} eV and any core distance larger than 5 km (see bottom left histogram in Fig. 5.11).

Fig. 5.12 shows the distribution of the vertical depth at shower maximum for the events with saturated virtual channel. Most of the events has a maximum well above the observation level (marked by a red line) and are thus potentially detectable. Therefore, the large majority of the events saturating the virtual channel are in principle detectable and should be recuperated.

Finally, in order to clarify the impact of the virtual channel gain settings on the FD monocular aperture, the second level trigger efficiency × R^2 (with R the core distance of each event from the FD Telescope) is shown in Fig. 5.13 for all events (black squares), for the fraction with at least one time bin saturated (red bullet) and for the fraction of those with saturated virtual channel (pink triangles). The flattening of the curve is due to the fact that the maximum core distance in the simulation sample is limited to 25 km where the Fluorescence Detector efficiency is 100% already at energies of $10^{19.5}$ eV. For this simulation, a gain ratio of 5 and 32 has been used for the plot on the left and on the right, respectively.

Check on real data

The actual value of the gain ratio was measured in the real data collected in 2004 and 2005 from Los Leones and Coihueco eyes. In order to correctly calculate the normal to virtual gain ratio, events with a single triggered pixel per virtual channel have been used for this analysis and a cut on minimum threshold for the signal charge has been applied. Saturated laser shots have been excluded. The average value found for all telescopes was

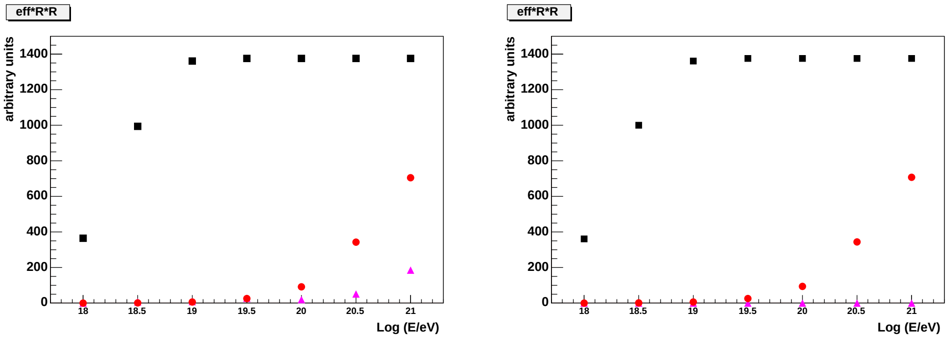

Figure 5.13: Simulations: trigger efficiency × R^2 for all events (black squares), for the fraction with at least one saturated time bin (red bullet) and for the fraction of those with saturated virtual channel (pink triangles). At the simulated core distances detector efficiency is 100% already at 19.5 eV. For this simulation, the normal to virtual channel gain ratio is set to 5 (left) and 32 (right).

in a range between 4 and 5, corresponding to the resistive partitor setting in the Analog Board. By means of the programmable potentiometers present in the AB, the value of the relative gains was raised to 20, a safe value according to this study.
As a cross-check the data collected by Los Leones, Coihueco and Los Morados, since February 2006, have been reconstructed and the relative gain ratio of each hit pixel has been calculated with our dedicated module. The gain map of the FD cameras of Los Leones, Los Morados and Coihueco has been filled. Fig. 5.14 shows the average distribution of the gain ratio for the six telescopes in Los Morados. The average value found for all telescopes is around 18, i.e. reasonably close to the expected one.
This method has also been applied to data the calibration laser shots (APF) in the Coihueco FD site. The different data sources (real showers and lasers) give results which agree to each other. Moreover, the nightly relative calibration shots (calA) could be useful to monitor the stability of the gain settings and to check for unwanted possible side effects (like the non-uniformity of the time response, etc.).

5.5.2 Saturation recovery

In real data analysis the saturated events are typically just removed from the analysis sample. We have shown that a significant fraction of the high energy events landing close to the detector would be lost. Even in the case of lower energy events the loss of information is not negligible if we consider that most of those showers are candidate to be stereo events and the complementary information would be lost. Moreover removing the saturated events could bias the data sample disfavoring specific geometric configurations.
The developed saturation recovery module has been implemented in the reconstruction sequence and tested on the simulated showers of sample 2.
Fig. 5.15 shows the energy and X_{max} residual distributions for the case of saturation recovered (blue line) or simply where saturated events have been removed (red line). The resolutions remain stable while the total number of events surviving the reconstruction

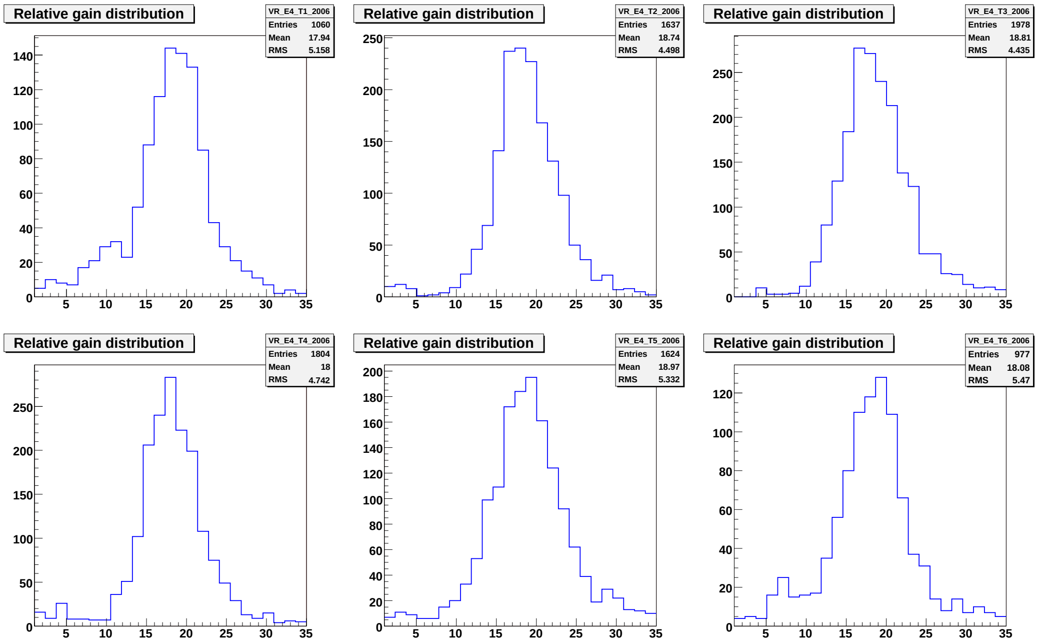

Figure 5.14: Real data: relative gain distributions for the 6 telescopes in Los Morados, collected data since Feb 2006. In order to correctly calculate the normal to virtual gain ratio, events with a single triggered pixel per virtual channel have been used for this analysis and a cut on minimum signal charge has been applied.

cuts[1] significantly grows (25%). A first achievement applying the recovery algorithm is then the increase of statistics at the highest energies.

The significant improvement in the treatment of the collected charge is evident when we look at the reconstructed profiles of the simulated events. Fig. 5.16 and Fig. 5.17 are two examples of the worst cases: the first is a very high-energy shower landing close to the FD detector, the second a more distant shower which is vertical in the SDP, so that all the PMT signals fall into two virtual channels only. The reconstruction power of the recovery method even in these extreme cases is evident.

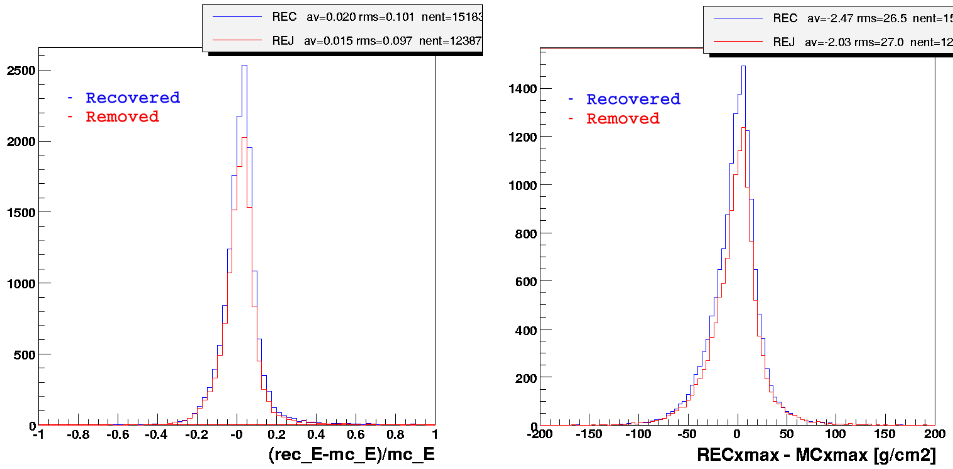

Figure 5.15: Left overall energy residuals distribution and right X_{max} residual distribution; the saturated events are recovered (blue line) or simply removed (red line). The resolutions are still affected by the inhomogeneities of the light collection. This problem can be only solved using a more detailed simulation of the light spot.

5.5.3 Treatment of light collection inhomogeneities

As shown in Fig. 5.15 the resolutions at the highest energy are still affected by the inhomogeneities of the light collection. Already at energies around $10^{19.5}$ eV the reconstructed profile begins to show a wavy sub-structure due to the inhomogeneity of light collection at the telescope focal surface. This fact results in a overall underestimation of the shower energy and a poor fit quality.

Fig. 5.18 shows an example of the light collected at the telescope diaphragm as a function of time bins for a shower of energy 10^{21} eV where the detector pixellation effect overcomes the signal uncertainty. The so called Spot method [52], a more detailed model taking into account the necessary corrections to the profile reconstruction algorithm, has been applied. The calculated expected photons (black line) follow accurately the data points. The first test run on a sample of 200 showers with energy 10^{21} eV, has been performed including the Spot method in the reconstruction algorithm. Fig. 5.18 shows the much better accuracy achieved, now at the level of 5.7% (RMS). A further effort to validate the method with dedicated simulations is planned.

---

[1] successful Gaisser-Hillas fit, bracketed X_{max}, longitudinal profile wider than 200 g/cm^2

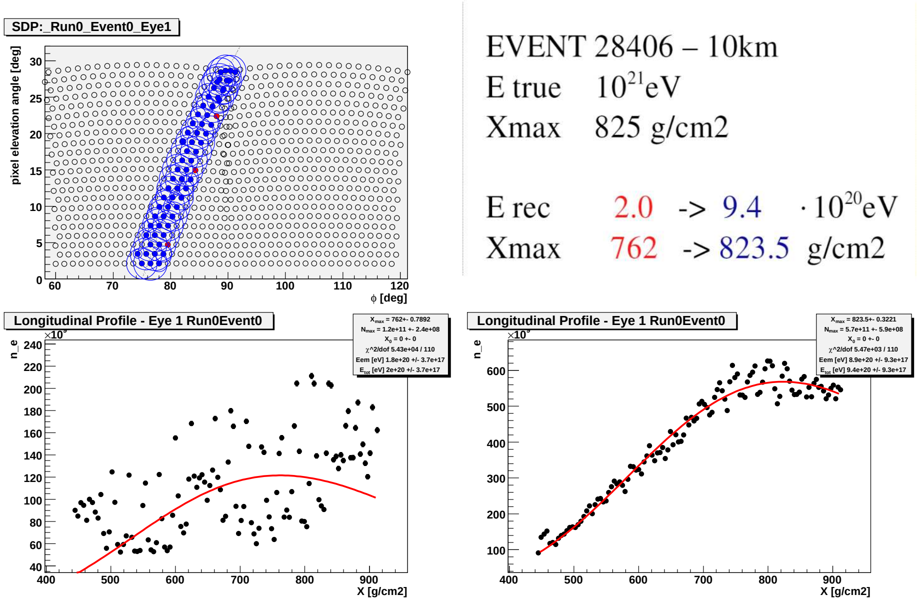

Figure 5.16: Example of a high-energy simulated shower landing very near to the Eye (E=10^{21} eV, d=10km). Top the SDP, bottom left the saturated longitudinal profile, bottom right the recovered.

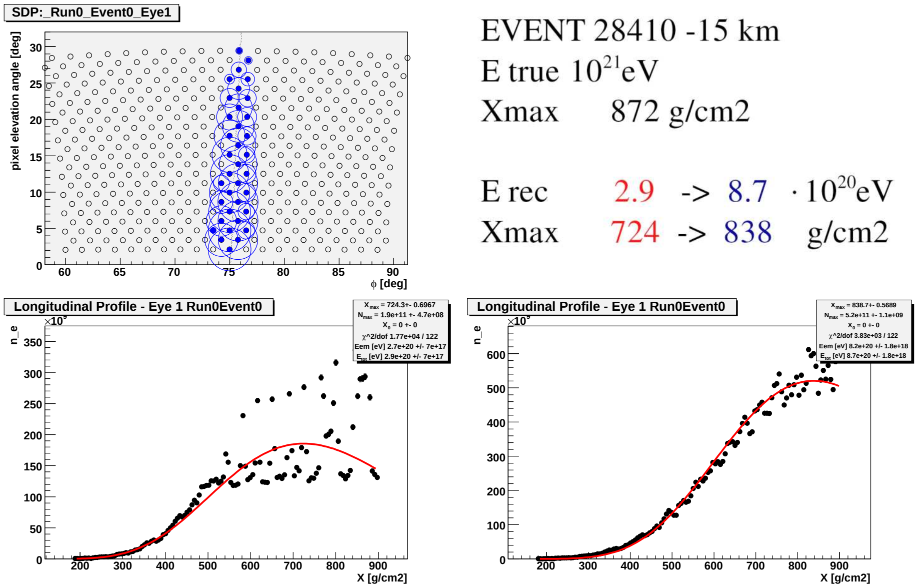

Figure 5.17: Example of a high-energy simulated shower vertical in SDP (E=10^{21} eV, d=15km). Top the SDP, bottom left the saturated longitudinal profile, bottom right the recovered.

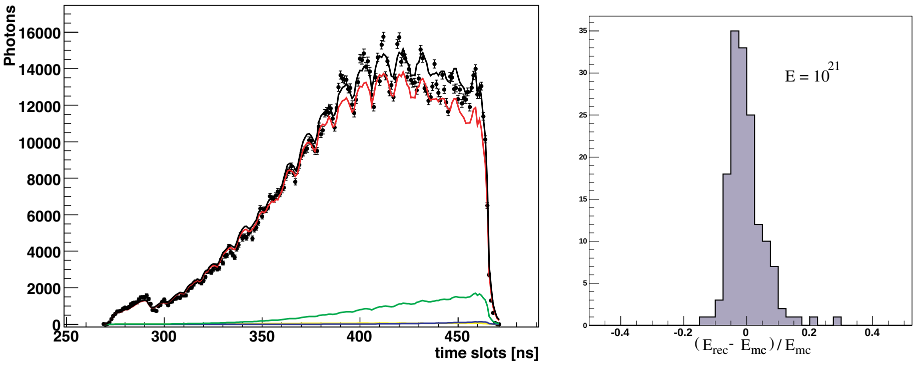

Figure 5.18: Left: light collected at the telescope diaphragm as a function of time bins for a shower of energy 10^{21} eV. The black dots data signal black line expected photons, red line fluorescence component, green Čerenkov. Right: energy residual distribution for events at 10^{21} eV including the corrections for light collection inhomogeneity, the so called Spot model, see [52]. Average -0.002, RMS 0.057.

5.5.4 Impact of quality cuts

The cuts adopted in this study have been widely used by the collaboration as they guarantee the quality of the reconstructed longitudinal profiles. We show how especially the cut on X_{max} and the one on the normalized χ^2 could introduce an energy dependent bias and have to be performed carefully.

The current field of view of the Fluorescence Detector is limited to $X_{lb} = 1.5°$ and $X_{ub} = 30°$, the lower and upper boundary respectively. A sketch of the FOV with examples of accepted and rejected profiles is shown in Fig. 7.2

The more distant the shower is, the higher in the atmosphere its track will fall out of the FOV. The nearer the shower is, the lower its track will fall in the FOV. This fact evidently causes an energy dependent bias, as the near showers are on average less energetic with a shallower X_{max} , and the more distant ones are more energetic showers with a deeper X_{max} . For the same reason a composition dependent bias is also introduced. On both sides a cut must be designed in order to avoid these biases on data reconstruction. Recent detailed studies of the necessary anti-bias cuts applied to data for the X_{max} measurement can be found in [154][152][25].

The intensity of the recorded light in each pixel is reflected in a smaller statistical uncertainty assigned to the time bins, which means, going back to the shower axis, that the points in the longitudinal profile fit have a smaller error. This simple consideration leads to the conclusion that a quality condition on the χ^2/Ndof of the Gaisser-Hillas fit, if not carefully applied, may result in the rejection of high-energy events. The solution is a more detailed error treatment at the level of shower profile including the precise propagation of the geometrical uncertainties. A new treatment of the profile reconstruction has lately been implemented in the official reconstruction, see [153].

Fig. 5.19 shows the reconstructed profiles of two simulated events with energy of 10^{21} eV. The event shown on the left is landing close to the telescope (Rp=21 km), the signal is large, the statistical uncertainty is small and the χ^2/Ndof of the Gaisser-Hillas fit gives

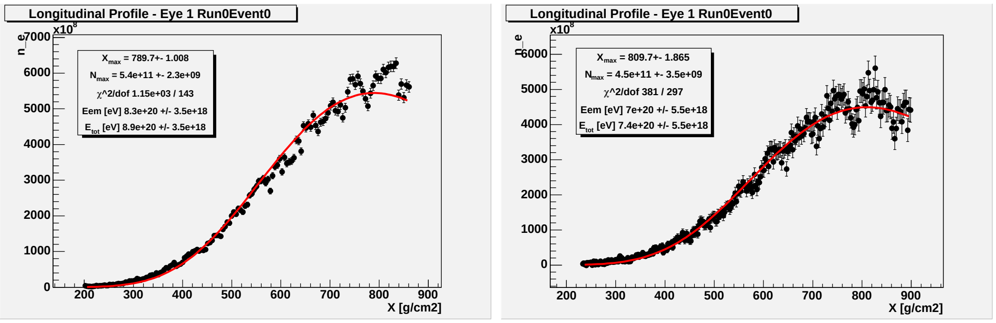

Figure 5.19: Reconstructed longitudinal profiles of events simulated at 10^{21} eV: left an event landing close to the telescope, right a more distant event. The first case is rejected because of a bad χ^2/Ndof, the second is instead accepted.

an insufficient significance and is rejected. The event shown on the right, with the same energy as the first, is landing further away (Rp=37 km), the signal is smaller, statistical errors are larger and the χ^2/Ndof of the Gaisser-Hillas fit improves, this event is accepted. Fig. 5.20, left panel, shows the normalized χ^2 distributions from the Gaisser-Hillas profile fit, as a function of primary energy. The correlation with energy is evident. Due to the large spread, even if the mean value satisfy the cut requirement, some of the highest energy events will be rejected. The impact of the two cuts on the detector aperture is shown in Fig. 5.20, right panel, (all events blue squares, X$_{max}$ cut pink triangles, $\chi^2/Ndof < 5$ red bullets).

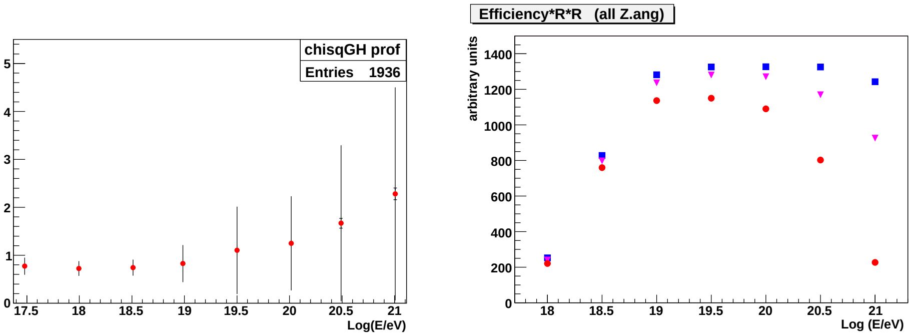

Figure 5.20: Left panel: profile plot of the normalised χ^2 from the Gaisser-Hillas profile fit, as a function of primary energy. Larger errors show the spread, smaller ones the spread divided by $\sqrt{N}$. Right panel: trigger efficiency × R^2 for all events (blue squares), for the fraction satisfying the condition on X$_{max}$ (pink triangles) and $\chi^2/Ndof < 5$ (red bullets). The trigger efficiency is already 100% at $10^{19.5}$ eV for the generated core distances.

Chapter 6

Simulation study of shower profiles from ultra-high energy cosmic rays

We investigate here the composition sensitivity of different parameters connected to the shape of the longitudinal shower profile. The position of the shower maximum, X_{max} , directly observed by the fluorescence telescopes, has been shown to be a powerful discriminant variable for composition studies. The motivation of this study is to search for further sensitive observables to enhance the discrimination power between different primaries. Photon selection, for instance, could be contaminated by late developing hadron cascades, in particular from deeply fluctuating protons.

A dedicated study has been performed on a set of simulated CORSIKA [71] showers induced by different primary particles. A fitting routine has been developed to extrapolate the profile parameters and test different proposed trial functions, like the Gaisser-Hillas [60], and the Gaussian [77, 143] or double Gaussian [64] in shower age.

Finally, a detailed study on the parameters correlations and the Principal Component Analysis (PCA) [42], see also[92], have been performed. The hadron-photon separation power of a simple X_{max} cut has been quantified and compared to the one achievable combining other sensitive observables. Results, reported in [139], are presented in the following sections.

The analysis is repeated on the reconstructed Monte Carlo sample to quantify the composition sensitivity after full hybrid detector simulation. Further tests on the combined observables, including other statistical parameters correlated with the longitudinal development, are planned.

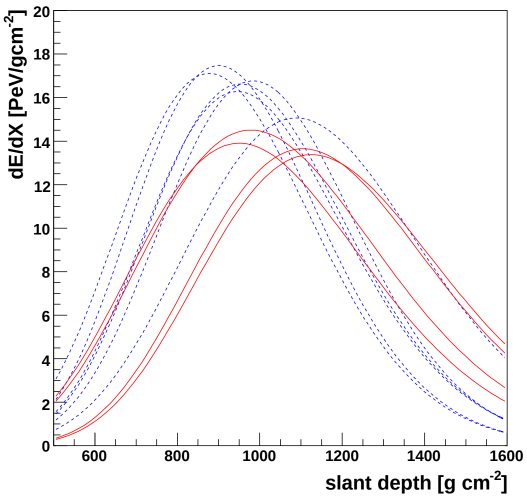

Figure 6.1: Example of $\frac{dE}{dX}$ profiles of simulated showers induced by photons (dashed blue line) and deeply fluctuating protons (thick red line) at 10 EeV.

6.1 Composition sensitivity of the shower profile

The Fluorescence Detector is observing directly the longitudinal shower development in the atmosphere. The detected light intensity, including the Fluorescence and Čerenkov direct and scattered contributions, and taking into account the atmospheric effects, is proportional to the energy deposited at each depth.

The longitudinal shower profile, here defined as the energy deposit as a function of atmospheric slant depth, can be reconstructed with good accuracy. The non-observed part can be extrapolated with a fit. As we have shown in section 2.1 (Eq. 2.10), the shower profile can be well described by the Gaisser-Hillas function (GH):

$$GH\left(X\right)=\left.\frac{dE}{dX}\right|_{X_{max}}\left(\frac{X-X_0}{X_{max}-X_0}\right)^{\frac{(X_{max}-X_0)}{\lambda}}\cdot\quad\exp\left[\frac{(X_{max}-X)}{\lambda}\right]\tag{6.1}$$

where X$_{max}$ is the position of shower maximum in slant depth, $\left.\frac{dE}{dX}\right|_{X_{max}}$ is the energy deposit at shower maximum.

X_0 and λ are strongly correlated and connected with the starting point and width of the curve, but cannot directly be interpreted as the first interaction point and interaction length, as already pointed out in [76].

The depth of shower maximum has good discriminating power between the different primaries inducing the cascade. The average value of X$_{max}$ for the simulated distribution for photons differs from that of hadrons by about 200 $\mathrm{g\,cm^{-2}}$ at 10 EeV. This evidence was used to set a limit to the photon fraction of the total flux [119] and for a recent update see [21].

In Fig.6.1 the energy deposit as a function of slant depth for some example profiles is plotted (dashed blue line for photons, thick red line for protons). The protons have been

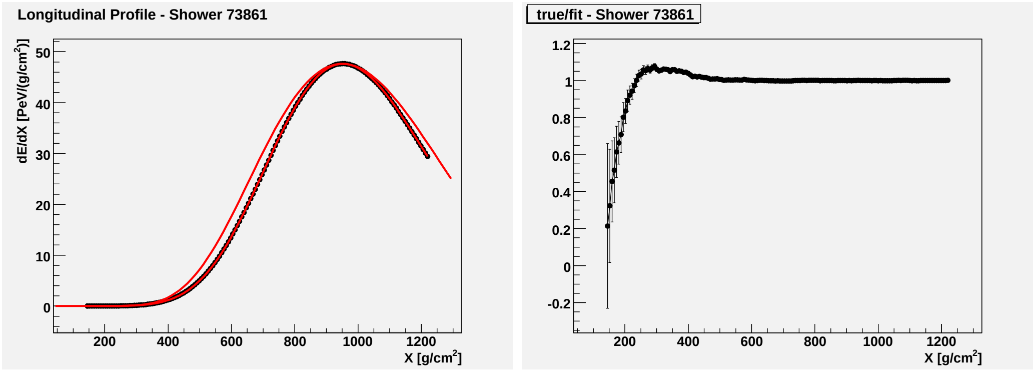

Figure 6.2: Left: longitudinal profile (energy deposit as a function of slant depth) for a simulated shower induced by a photon at 10^{19} eV. Black dots for the data points, dashed red line for CORSIKA 6-parameters GH fit, thick red line for the 4-parameters GH fit. Right residuals from the 4-parameters fit.

chosen to have a deep value of the shower maximum, compatible with the photon average distribution. In this case a selection based on X_{max} only would fail in discriminating protons from photons. We show in the next sections how further information coming along with the shower profile could enhance the discrimination power.

6.1.1 CORSIKA profile and Gaisser-Hillas fit

The simulated hadron sample consists of 750 protons and 500 iron nuclei per energy bin, ranging from $10^{17.0}$ eV to 10^{19} eV in steps of 0.5 in Log, (CORSIKA 6.200, FLUKA [55] and QGSJET01 [83] as low and high-energy hadronic interaction models). The photon sample, 1000 showers per energy bin, same energy range, has been generated with CORSIKA 6.600, FLUKA and QGSJET-II [106]. The thinning factor is in both cases 10^{-6}.
The longitudinal profile of each event is sampled in vertical steps of 5 $\mathrm{g\,cm^{-2}}$ and recorded in the CORSIKA output file, together with the result of a 6-parameter Gaisser-Hillas fit. Here λ, see Eq. 6.1, is replaced by a quadratic function of the atmospheric depth.
This fit is found to be robust for deriving X_{max} but less efficient in adapting the shape of the GH curve to data points, as can be seen in Fig 6.2. This may be connected with the limited number of profile points, especially in the falling side of the shower development.
A more effective 4-parameters constrained fit with the GH function has been implemented as reported in [153]. The X_{max} value agrees to CORSIKA better than 1 $\mathrm{g\,cm^{-2}}$.
In Tab. 6.1 the mean X_{max} value and the RMS spread, along with the σ of a Gaussian fit the distribution for iron, proton and photon showers at 10 EeV, are summarised. In Fig. 6.3 X_{max} is plotted as a function of the logarithm of the primary energy for different primaries, errors represent the RMS of the X_{max} distributions. A linear fit to the different components is also shown. The average X_{max} value for photons differs from that of hadrons by $\sim$ 200 $\mathrm{g\,cm^{-2}}$ or more. In this energy range the preshower effect is negligible and LPM effect dominates resulting in a deeper X_{max} for photons. The fluctuations are at the same level for photons and protons while much smaller, as expected, for the case of iron nuclei.

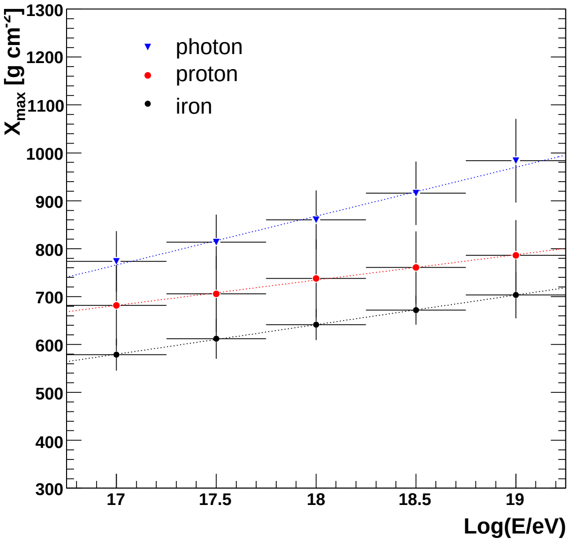

Figure 6.3: Depth of shower maximum, X_{max} , as a function of energy for different simulated primaries (photons blue triangles, protons and iron nuclei red and black bullets respectively). A linear fit of the different components is also shown.

6.1.2 Other trial functions and PCA analysis

The longitudinal profile can be translated into shower age s by means of the following transformation:

$$s(X) = \frac{3X}{X + 2X_{max}} \tag{6.2}$$

that aligns the profiles at $s(X_{max}) = 1$ and is scale-free. The shower starting point is in this case set to 0, but it could be added as a fourth fit parameter by substituting X with $(X - X_1)$. The normalised profile can then be fitted by the following Gaussian function in age (AG):

$$AG(s) = \exp\left(-\frac{1}{2\sigma^2}(s-1)^2\right) \tag{6.3}$$

where σ and X_{max} are free parameters, together with $\frac{dE}{dX}\big|_{X_{max}}$.

Table 6.1: Mean value, RMS spread, and Gaussian σ of the X_{max} distribution for different simulated primaries at 10 EeV, as extrapolated from the 6-parameters GH fit.

	$< X_{max} >$ [g cm^{-2}]	RMS [g cm^{-2}]	σ [g cm^{-2}]
Iron	703	48	24
Proton	786	73	57
Photon	983	87	59

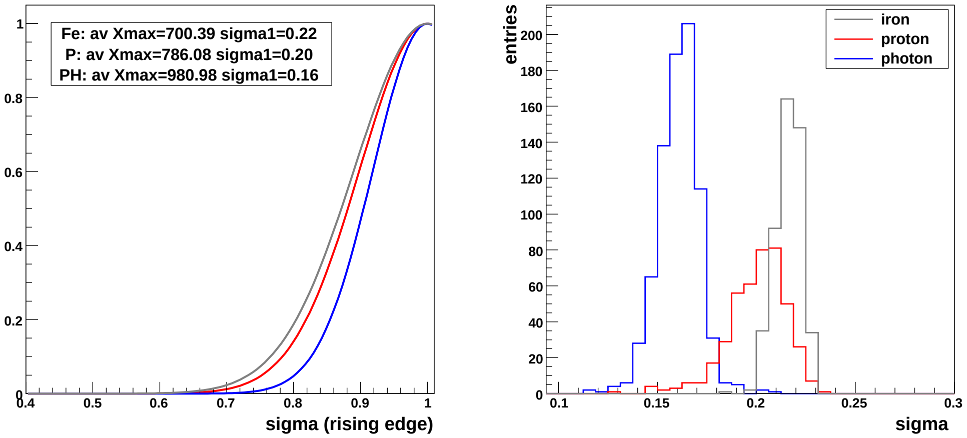

Figure 6.4: Left panel: average rising shower profile (2G) for simulated photons (blue line), protons (red line) and iron nuclei (grey line) at 10 EeV. Right panel: distributions of the σ (AG), same color code. For the average and RMS values, see Tab. 6.2.

Following [64] we can employ a double Gaussian fit (2G) with two different widths corresponding to the shower development before and after the shower maximum. The number of free parameters is increased in this case to four.

In Fig. 6.4 left panel, the average rising shower profiles obtained with the 2G fit for simulated photons (blue line), protons (red line) and iron nuclei (grey line) are plotted. The right panel shows the distributions of the width (σ) of the Gaussian in shower age (AG), same color code. In Tab. 6.2 the mean and RMS values for the σ AG for the simulated iron, proton and photon showers are summarised.

The fitting routines can be compared on the base of the average relative residuals. In Fig. 6.5 the average relative residuals, as a function of shower age, obtained with the tested analytical fit functions are plotted for the proton sample. While the CORSIKA 6-parameters fit tends to depart from the data points at the profile margins, the GH 4-parameter fit is found to be robust and the agreement with profile data extends on the entire range. The Gaussian fits in age show a good agreement too.

The correlation between the width of the Gaussian AG and the depth of shower maximum is shown in Fig. 6.6 (left panel). A later development of the cascade is associated

Table 6.2: Mean and RMS of the width (σ) distributions of the different simulated primaries at 10 EeV, for the AG fit.

	Mean width ($<\sigma>$)	RMS
Iron	0.22	0.006
Proton	0.20	0.015
Photon	0.16	0.011

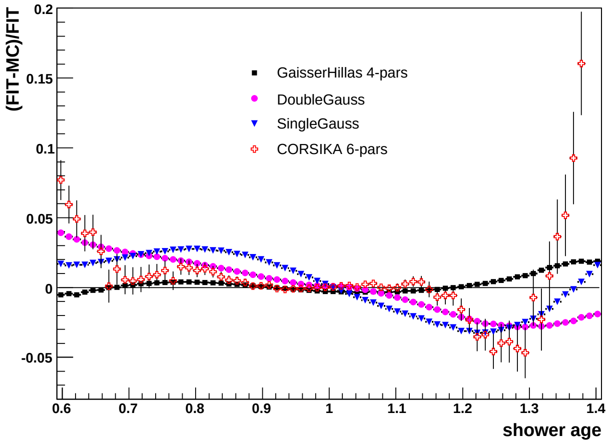

Figure 6.5: Average relative residuals to the tested analytical functions for protons at 10 EeV: GH 4-parameters fit (black squares), single Gaussian (blue triangles), double Gaussian (pink bullets), and 6-parameters CORSIKA (red crosses).

with a narrower profile width. Similar average values and the same correlation are found between the rising edge σ and the X_{max} for the 2G fit, in agreement with the previously cited works.
Using X_1 as a free parameter in the fitting process we observe a correlation with σ that can be represented, both for hadrons and photons, by a straight line. This correlation is shown in Fig. 6.6 (right panel) for the simulated sets of iron, proton and photon primaries. The possibility to exploit the additional information carried by the width of the profile,

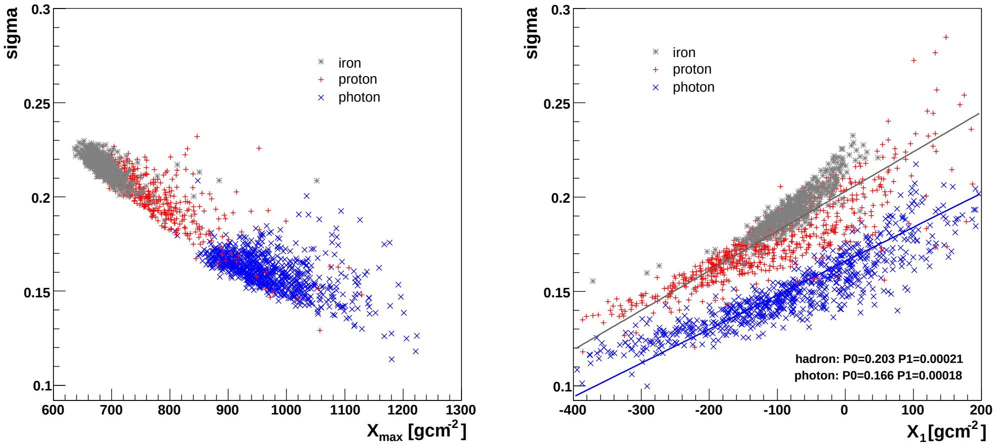

Figure 6.6: Left panel: correlation between the width of the Gaussian (AG) and depth of shower maximum for showers at 10 EeV initiated by iron, proton and photon primaries, respectively marked as grey stars, red crosses and blue ×-shaped crosses. Right panel: correlation between σ and X_1, same color code.

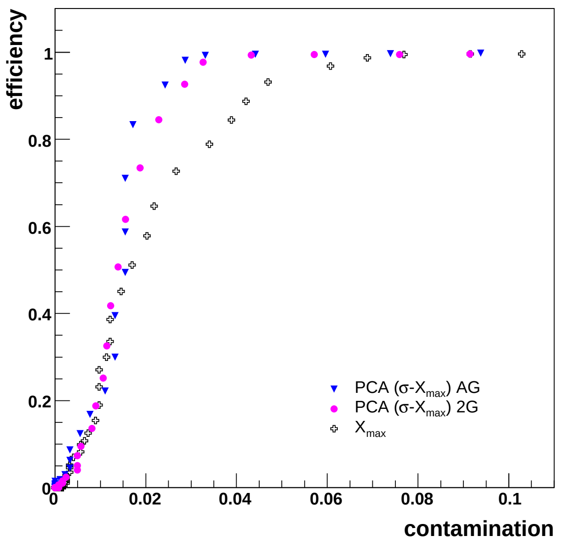

Figure 6.7: Efficiency for accepting photons as a function of hadron contamination in the PCA-transformed variable (σ and X_{max} combined) for the single Gaussian (blue triangles) and for the double Gaussian (pink bullets) compared to the X_{max} cut (black crosses for AG).

described by σ, for the separation between different primaries has been studied. Applying the Principal Component Analysis (PCA) it has been quantified for the case of photon-hadron separation.
In Fig. 6.7 the efficiency of a cut for accepted photons in the PCA transformed variable is plotted as a function of the hadron contamination. Blue triangles refer to the single Gaussian fit and pink bullets to the double Gaussian fit. The photon-hadron separation power of a cut in the PCA variable compared to a X_{max} cut on the data set (black crosses for the AG) is clearly enhanced in both cases. The same analysis has been tested in a three dimensional space for the GH fit (λ, X_{max} and X_0) and for the Gaussian in age (σ, X_{max} and X_1) letting X_1 be the curve starting point. The enhancement of the separation power was found to be less evident in those cases.

6.2 Separation power after full detector simulation

A test of the PCA analysis after applying the full detector simulation reconstruction chain has been performed. The uncertainties associated to the geometry reconstruction, together with the limited field of view of the detector and the disuniformities in the light collection, reflect in the smearing of the fit parameters distributions. Consequently a partial loss of the hadron-photon separation capability is expected.
The combinations of variables from the fitting routines which gave, in the previous section, the highest efficiency in distinguishing hadrons from photons have been tested again here. The correlation between the width of the Gaussian (AG) and depth of shower maximum for showers at 10 EeV, initiated by iron, proton and photon primaries, respectively marked

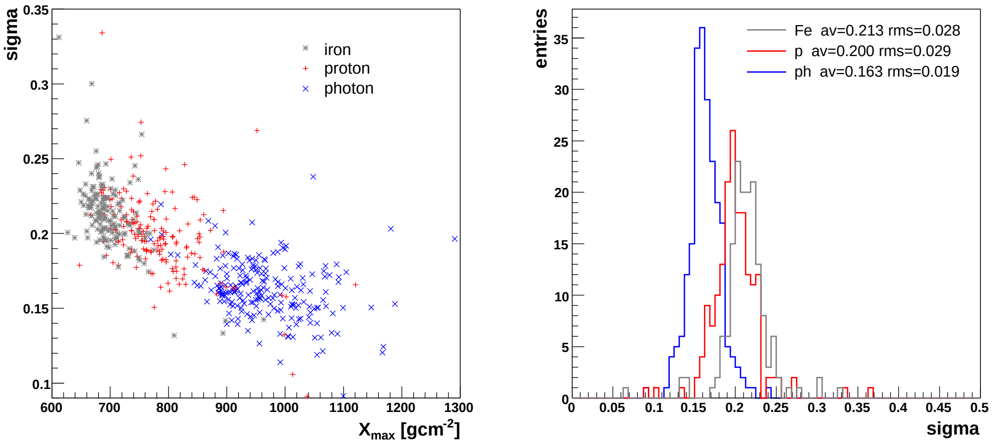

Figure 6.8: After full detector simulation: left panel: correlation between the width of the Gaussian (AG) and X$_{max}$ for showers at 10 EeV initiated by iron (grey stars), proton (red crosses) and photon primaries (blue ×-shaped crosses). Right panel: σ distribution (AG).

with grey stars, red crosses and blue ×-shaped crosses, is plotted in Fig. 6.8 left panel, to compare to Fig. 6.6 (left panel). The right panel shows the σ distribution; the separation between hadron and photon distributions is smaller, compared to the right panel of Fig. 6.4, but still evident.

Finally, in Fig. 6.9 the efficiency for accepting photons as a function of the hadron contamination in the PCA-transformed variable (σ and X$_{max}$ combined) for the single Gaussian (blue triangles) and for the double Gaussian (pink bullets) compared to the X$_{max}$ cut (black crosses for AG), is plotted.

After the full detector simulation, due the uncertainties in the profile reconstruction and the consequent smearing of the fit parameters, the enhancement obtained in the previous section seems to be lost. However, as pointed out also in an independent analysis [41], there is still room for improvement. Further tests on the combined observables including other statistical parameters like the asymmetry or the skewness of the profile, are planned.

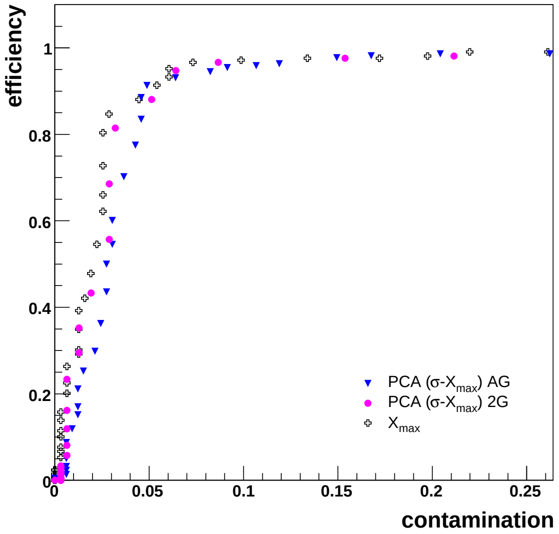

Figure 6.9: After full detector simulation: efficiency for accepting photons as a function of hadron contamination in the PCA-transformed variable (σ and X$_{max}$) for the single Gaussian (blue triangles) and for the double Gaussian (pink bullets) compared to the X$_{max}$ cut (black crosses for AG).

Chapter 7

Upper limit to the photon fraction in cosmic rays

The first upper limit to the photon fraction in cosmic rays at energies above 10 EeV from the Pierre Auger Observatory hybrid data, was derived using the depth of the shower maximum as the discriminating observable. The stated limit is 16% at 95% c.l., see [119]. We perform the update of that analysis with one more year of collected data, which allows us to reach a limit of 13% at 95% c.l., see [21].

Our next step is to lower the energy threshold of the data sample, in order to benefit from a factor $\sim (E/10^{19})^{-3}$ larger statistics. The challenge is now to place the limit in a region where the detector efficiency may drop below 100%. This is only possible after a detailed study of the relative acceptance, assuming hadron and photon primaries, by means of a full hybrid detector simulation.

The increased statistics at lower energies allows applying the method described briefly in section 7.1.2. The Auger hybrid data collected between February 2004 and July 2007 in two of the four fluorescence telescopes are used in this analysis. The derived upper limits are 3.7%, 1.8%, 3.7% and 11.6% respectively above 2, 3.16, 5 and 10 EeV (all limits at 95% c.l.) see 7.3.3. The impact of a photon contamination of this order, on the estimate of the inelastic p-air cross section, is briefly discussed in section 7.4.

7.1 Deriving an upper limit

The key observable to derive the integral upper limit to the photon fraction in cosmic rays with Auger hybrid data is the depth of shower maximum. As already discussed in section 6.1.1, this observable offers a very good discrimination power between hadrons and photon induced events. In this analysis the direct observation of the shower longitudinal profile from the Fluorescence Detector is combined with the high accuracy of the hybrid geometry reconstruction.

As we demonstrated in chapter 6.1.2, discriminant variables could be built from a combination of independent characteristic observables connected to the longitudinal profile, like the curve width or the derived first interaction point. Moreover hybrid detection gives the chance to combine profile developement quantities with shower front parameters measured by the surface array, for example the signal rise-time or the front curvature. Exploiting the capabilities of the different detection techniques is the natural next step to take after this work.

7.1.1 Small data sample: probabilistic method

We describe briefly here the method we apply for deriving the updated limit to the photon fraction in the cosmic ray flux above 10 EeV, see section 7.2. This method has been first developed for the analysis of the highest energies Fly's Eye data [129], AGASA data [130], and extended for the analysis of the Auger data above 10 EeV [119].

The method is very powerful in the case of small data samples. With increasing statistics, on the one hand, the computing time required for the dedicated event-by-event simulations becomes too large, on the other hand, more powerful statistical tools can be applied, as this method tends to be over-conservative.

A sample of high quality reconstructed events is selected from the bulk of recorded data. The measured discriminant observable, the depth of shower maximum X_{max} , is compared to the theoretical expectations for showers of the same geometry and energy, but assuming a primary photon origin.

The minimum possible fraction to be excluded with a given number of measured events n_m is:

$$F_\gamma^{min} = 1 - (1-\alpha)^{1/n_m} \tag{7.1}$$

where α is the required confidence level. This theoretical limit is reached only if a photon origin can be basically excluded for every event in the set.

For each measured event a large set of dedicated simulations of photon induced showers with the same characteristics (primary energy and direction) is performed. To quantify the probability for each event in the set to be consistent with the photon hypothesis, a χ^2 can be defined as follows:

$$\chi_i^2 = \frac{(X_{\mathrm{max,i}} - < X_{\mathrm{max}}^\gamma >)^2}{(\Delta X_{\mathrm{max,i}})^2 + (\Delta X_{\mathrm{max}}^\gamma)^2} \tag{7.2}$$

where $X_{\mathrm{max,i}}$ and $\Delta X_{\mathrm{max,i}}$ are the measured depth of shower maximum and its uncertainty for the i-th event, $< X_{\mathrm{max}}^\gamma >$ and $\Delta X_{\mathrm{max}}^\gamma$ are the mean depth of shower maximum and RMS fluctuations predicted from simulations.

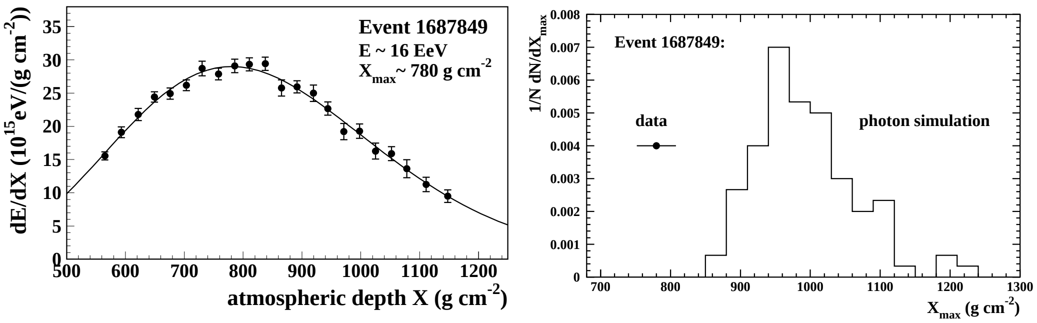

Figure 7.1: Left: reconstructed shower profile for event sd_1687849. Right: X_{max} of data point along with photon simulated distribution, see [119].

The probability p_γ for the i-th event to give a χ^2 larger than observed is determined via a Monte Carlo method, naturally taking into account non-gaussian fluctuations, for details see [130]. A smaller value indicates most probable hadron origin.

A set of artificial data events is produced by randomly shifting each of the candidates by the systematic uncertainty. To test a photon fraction the χ_i^2 for the single shifted data point are ordered and a total data χ^2 is obtained summing up the n_γ most photon-like events. A global simulation χ^2 is obtained summing the contributions from the corresponding simulated photons, randomly shifted according to the experimental resolution. The probability of the simulation χ^2 exceeding the data one, gives the probability for a real photon fraction F_γ to produce larger deviations than observed in data.

For the fraction F_γ we have the following relation:

$$P(F_\gamma) = \sum_{n_\gamma=0}^{n_m} F_\gamma^{n_\gamma}(1-F_\gamma)^{n_m-n_\gamma} \left(\begin{array}{c} n_m \\ n_\gamma \end{array} \right) \cdot p_\gamma(n_\gamma) \cdot p_{\bar{\gamma}}(n_m - n_\gamma) \tag{7.3}$$

where $p_{\bar{\gamma}}$ are the probabilities, for non-photons, to give larger χ^2 then in data.

A correction for the relative detector acceptance for photon and nuclear primaries must be also applied, see 7.1.4. Finally, the photon fraction F_γ can be excluded with confidence level $\alpha = (1 - P(F_\gamma))$.

In Fig.7.1 the reconstructed longitudinal profile, the measured X_{max} along with the dedicated photon simulations, are plotted for an event of the candidate lists. This is a typical event with energy 16 EeV and X_{max} ~ 780 g cm^{-2} . The mean X_{max} of the photon simulations is ~ 1000 g cm^{-2} , and the corresponding deviation in units of standard deviations is 2.9.

7.1.2 Large data sample: statistical method

We describe here the method adopted for setting the limit to the photon fraction in cosmic rays above 2 EeV, see 7.3.3. This method, based on the classical Neyman hypotesis test[103], becomes more powerful than the previous when dealing with large data sample. This is also the case for the limit with data from the surface detector, see [21].

A discriminant observable is chosen and an *a priori* cut is determined, which divides the variable space in two regions.

By observing a number n_γ of events above the cut, the upper limit to the photon fraction in the full data sample is set. The 95% confidence level upper limit is calculated, according to Neyman-Pearson prescription, assuming zero background, i.e. the n_γ events above the cut are deemed to be photons.
A procedure could be implemented to optimise the selection power of the cut, finding a compromise between overlapping region and cut efficiency i.e. the fraction of photons below the cut, for instance by testing it on a simulated hadron sample. However we decide to stick to the most straightforward and robust solution, namely cutting at the median of the simulated photon X_{max} distribution. The corresponding cut efficiency f, to be taken into account in the final step of the calculation, in our case is then simply 0.5.
The integral upper limit to the photon fraction F_γ in the data sample above an energy threshold E_{thr} is:

$$F_\gamma(E > E_{thr}) = \frac{n_\gamma(E_\gamma > E_{thr}) \cdot \frac{1}{f} \cdot \frac{1}{\epsilon_{det}}}{n_\gamma(E_\gamma > E_{thr}) + n_{\bar{\gamma}}(E_{\bar{\gamma}} > E_{thr})} \tag{7.4}$$

where n_γ is the number of observed candidates above threshold at a confidence level α, $n_{\bar{\gamma}}$ is the number of non-photon events in the sample, with reconstructed energy above E_{thr}, and ϵ_{det} is the relative detector acceptance (photon vs hadron).
Knowing the aperture A of the detector an integral upper limit on the flux of photons above E_{thr} can be set according to the following relation:

$$\Phi_\gamma(E > E_{thr}) = \frac{n_\gamma(E_\gamma > E_{thr}) \cdot \frac{1}{f} \cdot \frac{1}{\epsilon_{det}}}{A} \tag{7.5}$$

The aperture calculation is quite simple and accurate in case of the surface detector. In the hybrid case, expecially due to the ongoing construction of the fluorescence detector, a bigger effort is needed to reproduce the experimental operating conditions. A detailed calculation of the aperture and uptime of the hybrid detector has been performed in [111] and [110].

7.1.3 General considerations on the derived limits

The discussed methods are both conservative, in the sense that they don't take into account, and consequently subtract, the hadron background contribution. In Eq.7.3 the probabilities for non-photons to generate larger χ^2 than in data are set to one. For the statistical method this means that the surviving events, those passing the photon cut, are treated indeed as photons, then giving a higher upper limit.
Both the methods suffer from a systematic limitation due to the overlapping area of the photon-like and hadron-like distributions. In this region, the probabilities for a hadron induced event to be consistent with photons are large, consequently rising the limit. The second method is less affected, as the overlapping region might not extend beyond the applied cut, depending on its position.
However most of the photon-deemed events could come from the hadron tails. The estimation of background is then necessary if one wants to obtain confidence level intervals for the photon fraction, according to Feldman-Cousins [56], and definitely essential to claim an observation.
As a matter of fact, the background from hadronic primaries is very difficult to estimate.

Model dependence is the largest source of uncertainty, in particular regarding the tails of the X$_{max}$ distributions. Even if the hadron background can't be reliably predicted from our Monte Carlo simulations, as the sample is not meant to reproduce the real cosmic rays spectrum, a temptative plot to quantify the fraction of expected background events is given for protons and iron nuclei in Fig. 7.11.

The number n_γ of photon candidates measured in an experiment, is expected to fluctuate according to a Poisson distribution with mean μ:

$$P\ (n_\gamma|\ \mu) = \frac{\mu^{n_\gamma} e^{-\mu}}{n_\gamma!} \tag{7.6}$$

The upper limit is stated with confidence level α requiring that, for a fraction $(1-\alpha)$ of identical experiments, a number of photon candidates smaller or equal to n_γ, could be observed. We have than:

$$(1-\alpha) = \sum_{n=0}^{n_\gamma} \frac{\mu^n e^{-\mu}}{n!} \tag{7.7}$$

The value of μ is taken as the final number of candidates. For this work $\alpha = 95\%$.

7.1.4 Acceptance correction

Another essential contribution to be taken into account is the relative efficiency in detecting photon showers with respect to hadron primary induced showers. The fraction of photons F_γ in the cosmic-ray flux integrated above an energy threshold E_0 (assuming photon primaries) is given by:

$$F_\gamma(E \geq E_0) = \frac{\int_{E_0} \Phi_\gamma(E)dE}{\int_{E_0} \Phi_\gamma(E)dE + \sum_i \int_{E_0} \Phi_i(E)dE} \tag{7.8}$$

where $\Phi_\gamma(E)$ denotes the differential flux of photons and $\Phi_i(E),\ i = \mathrm{p}, \mathrm{He}, ...$ the fluxes of nuclear primaries.

Knowing the detector acceptances, $A_\gamma(E)$ and $A_i(E)$, to photon and nuclear primaries respectively, the fraction of detected photons F_γ^{det} is given by:

$$F_\gamma^{\mathrm{det}}(E \geq E_0) = \frac{\int_{E_0} A_\gamma(E)\Phi_\gamma(E)dE}{\int_{E_0} A_\gamma(E)\Phi_\gamma(E)dE + \sum_i \int_{E_i} A_i(E)\Phi_i(E)dE} \tag{7.9}$$

where E_i $(> E_0)$ is the threshold energy assuming primary nucleus i, that is related to E_0 by the ratio of the missing energy corrections ($\sim 1\%$ for photons, $\sim 7\% - 14\%$ for proton and iron nuclei). By subtitution into Eq. 7.9 we get:

$$\begin{aligned} F_\gamma^{\mathrm{det}}(E \geq E_0) &> \frac{\int_{E_0} A_\gamma(E)\Phi_\gamma(E)dE}{\int_{E_0} A_\gamma(E)\Phi_\gamma(E)dE + \sum_i \int_{E_0} A_i(E)\Phi_i(E)dE} \\ &= \frac{\int_{E_0} A_\gamma(E)\Phi_\gamma(E)dE}{\int_{E_0} A_\gamma(E)\Phi_\gamma(E)dE + \sum_i \int_{E_0} \frac{A_\gamma(E)}{\epsilon_i(E)}\Phi_i(E)dE}\ , \end{aligned} \tag{7.10}$$

where the acceptance ratio $\epsilon_i(E) = A_\gamma(E)/A_i(E)$ was introduced. If A_γ keeps constant in the studied energy ranges, Eq. 7.10 can be simplified as follows:

$$\begin{aligned} F_\gamma^{\mathrm{det}}(E \geq E_0) &> \frac{\int_{E_0} \Phi_\gamma(E)dE}{\int_{E_0} \Phi_\gamma(E)dE + \frac{1}{\epsilon_{\mathrm{min}}} \sum_i \int_{E_0} \Phi_i(E)dE} \\ &> \epsilon_{\mathrm{min}} \cdot F_\gamma(E \geq E_0) \;, \end{aligned} \tag{7.11}$$

since $\epsilon_{\mathrm{min}} < 1$.

In this way the upper limit F_γ^{ul} to the fraction of photons in the cosmic-ray flux can conservatively be calculated as

$$F_\gamma^{\mathrm{ul}} = F_\gamma^{\mathrm{det}}/\epsilon_{\mathrm{min}} > F_\gamma \;. \tag{7.12}$$

independently on assumptions for the differential fluxes $\Phi_\gamma(E)$ and $\Phi_i(E)$.

7.2 Update of the hybrid limit above 10 EeV

7.2.1 Data sample

The data sample used for this analysis contains the events recorded, between February 2004 and March 2007, from the fluorescence eyes together with the surface detector tanks. Due to the ongoing construction of the FD detector which has been completed in February 2007, we selected only the events with a trigger in one of the two FD telescopes, Los Leones or Coihueco. The total number of recorded events is 221250.

The hybrid reconstruction benefits from a much accurate geometry reconstruction as respect to FD only. The angular resolution is ~ 0.5° [47] compared to ~ 2° for FD only as reported also in sec 5.3. The higher geometric accuracy reflects in a smaller uncertainty on the determination of the shower maximum. The hybrid X_{max} and energy resolution are of the order of 20 $\mathrm{g\,cm^{-2}}$ and 9% respectively, (the overall uncertainty in the energy scale is at the level of 22% [47]).

The data sample has been first processed in our cluster with the $\overline{\text{Off}}\underline{\text{line}}$ [10] reconstruction software, version v1r2-rc1. The so called advanced data summary tree (ADST), has been recently released by the Auger collaboration and is available for downloading at [148]. The provided ASCII files have been parsed and the essential variables stored in a table belonging to a local database. After an overall consistency test and an event-by-event cross-check the ADST has been adopted in this analysis. The advantage of this solution is to have a reliable and up-to-date reconstructed data sample.

The latest profile reconstruction implements the new method described in [153] and includes a detailed and reliable error treatment. The end-to-end calibration of the FD detectors [22], the monthly models for the atmosphere [90], and an average aerosol model [117] based on local measurements, are also adopted in the reconstruction procedure.

The main contributions to ΔX_{max} in Eq. 7.2 are the uncertainties in the profile fit, in shower geometry and in atmospheric conditions. The systematic uncertainty in the simulation predictions comes mainly from the detector energy resolution which, for an average elongation rate of 106 $\mathrm{g\,cm^{-2}}$ per energy decade, means ~ 10$\mathrm{g\,cm^{-2}}$. A correction of ~ 1% for the missing energy, calculated assuming photon primaries [113], was applied to the reconstructed electromagnetic energy. In this way the energy threshold of the analysis corresponds to the effective energy of primary photons. This choice is conservative in the sense that, by underestimating the energy of nuclear primaries, it tends to fill the sample with photons, consequently raising the upper limit.

7.2.2 Reconstruction requirements

The quality of geometry and shower profile reconstruction can be guaranteed applying the following cuts, in agreement with the previously cited paper:

- hybrid trigger and geometry reconstruction quality cuts:
  - number of phototubes in the fluorescence detector triggered by shower $\geq$6;
  - number of Čerenkov tanks in the surface detector triggered by shower $\geq$1;
  - distance of the reconstructed shower axis to the hottest tank <1.5 km;
  - difference between SD measured time and FD estimated time at tank < 300 ns

- quality of Gaisser-Hillas (GH) profile fit:
  - χ^2(GH) per degree of freedom <6,
  - χ^2(GH)/χ^2(line)<0.9, where χ^2(line) refers to a straight line fit;

- observed depth of shower maximum;

- minimum viewing angle (angle between FD pixel direction and shower axis) >15°;

- reconstructed primary energy E>10^{19} eV;

Requiring the shower maximum to be in field of view (FOV) is a very strict cut, but necessary to guarantee the quality of the X_{max} measurement itself. As discussed also in section 5.5.4 this cut may introduce an energy dependent bias in the reconstructed sample. Moreover, for this analysis, the absence of a composition dependent bias is essential. The requirement of X_{max} observed, instead, causes the rejection of photon induced showers, that on average develop later with respect to hadron induced showers. This happens especially for showers with small zenith angles, or landing far from the fluorescence detector, see Fig. 7.2.
As the lower limit of the FOV is about 1.5° above horizon, the not observed shower portion near the ground grows with distance. The photon induced events, with a mean X_{max} closer to ground with respect to hadron showers, would then be more efficiently rejected with growing core distance. The higher absorption of fluorescence light in the lower atmosphere contributes to further reducing the distance range in which the FD is fully efficient for detecting photon induced showers.
To reduce those biases two further cuts, one on small zenith angles and one on large core distances, are introduced in the analysis. The energy dependent relations are the following:

- shower zenith angle $> 35^\circ \ + \ g_1(E)$,
  where $g_1(E) = 10(\lg E/\mathrm{eV}{-}19.0)^\circ$ for $\lg E/\mathrm{eV} \leq 19.7$
  and $g_1(E) = 7^\circ$ for $\lg E/\mathrm{eV}{>}19.7$

- distance of FD telescope to shower core < 24 km + $12(\lg E/\mathrm{eV}{-}19.0)$ km.

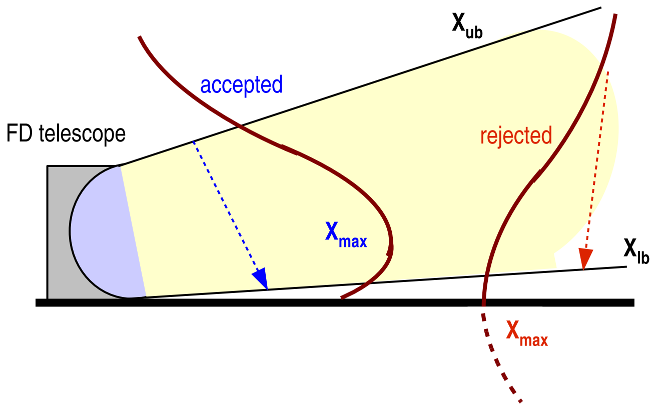

Figure 7.2: Sketch of the Fluorescence Detector field of view. Shown are the upper and lower boundaries, $X_{ub} = 30°$ and $X_{lb} = 1.5°$.

The last quality requirement for each event is that its observation should not be affected by the presence of a cloud in the telescope field of view. The anomalous scattering of light could in some cases bias the X_{max} reconstruction towards deeper values. An example of a rejected event is shown in Fig. 7.3.
For each candidate, a very accurate selection, based on the cloud monitoring information available for the corresponding event time, is performed[1]. The cross check using the information from different monitoring devices, if available, allows one to detect the presence of clouds more precisely along the reconstructed shower path. This reduces the number of rejected events as, in many cases, the cloud is in FOV but sufficiently behind the shower axis.
The applied cuts and relative efficiencies are summarised in Table 7.1. The distribution of the variables for the data sample after quality cuts, along with hadron and photon simulations, are given in Appendix B. The distributions of the cut variables requiring all cuts but the one plotted, the so called N-1 plots, are shown too.

7.2.3 Photon candidate distributions

The measured X_{max} distribution for all the events that meet the quality and fiducial cuts is shown in Fig. 7.4 left panel. After requiring no cloud disturbance, 58 events are selected in total. The X_{max} distribution for the final canditates sample is shown in figure 7.4 right panel, along with the calculated distribution from 10 EeV photons made on an event-by-event basis. Even the largest observed value of X_{max} , $\sim$ 900g cm^{-2} , is well below the mean value expected for photons at this energy (about $\sim$ 1000 g cm^{-2} , see Tab. 6.1).

---

[1] in collaboration with Michael Winnick, Pierre Auger group, University of Adelaide, Australia [123].

Table 7.1: Applied cuts, surviving events and cut efficiency for this analysis on the Auger Hybrid data sample (FD LosLeones and Coihueco February 2004 - March 2007. In total 221250 events).

Quality cuts	Surviving events	Surv eff. %
hybrid geometry:		
triggered FD pixels ≥ 6	135473	61
tank-axis distance < 1.5 km	85363	63
SD-FD time res < 300 ns	84129	99
profile reconstruction:		
observed X_{max}	41979	50
χ^2_{GH}/ndof <6	40726	97
$\chi^2_{GH}/\chi^2_{line} < 0.9$	23433	58
min view angle $> 15°$	15181	65
Energy $\geq$ 10 EeV	**194**	
Fiducial cuts:		
axis $\Theta > 35° + g_1(E)$	122	63
core distance < 24 km $+ g_2(E)$	72	59
Cloud check	58	81

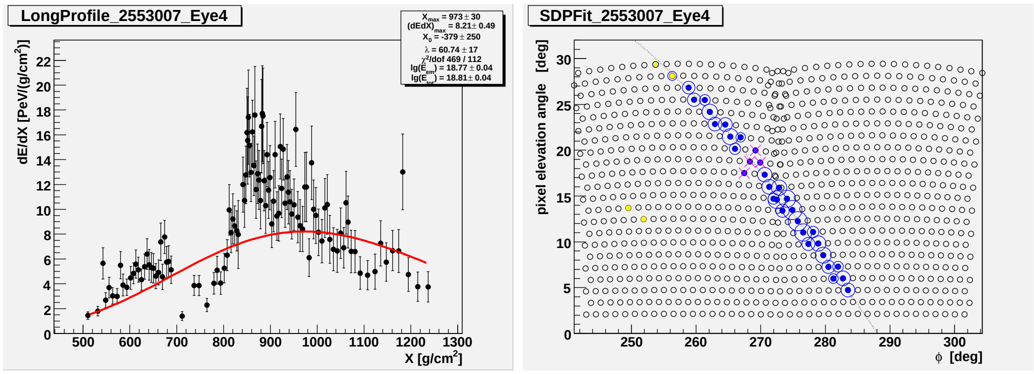

Figure 7.3: Left: example of an event rejected after the cloud check. The strong attenuation and the change in the shape of the light intensity curve is evident. The fit moves the shower maximum towards a deeper value. Right: event trace on the FD camera, the rejected pixels are marked by a pink cross .

7.3 Upper limit above 2 EeV

This analysis is performed using the Auger hybrid dataset, collected in the two fluorescence telescopes (Los Leones and Coihueco) between February 2004 and July 2007. The total number of recorded events is 270922

In the energy range above 10 EeV the hybrid detector is fully efficient and in principle only the relative acceptance ratio, for showers induced by photon and hadron primaries, must be taken into account. At lower energies, while the FD efficiency is still saturated, the SD trigger efficiency quickly falls. The response of the detector at threshold energies might even more significantly differ for different primaries species. The full simulation of the hybrid detector, is then a necessary step to place the upper limit to the photon fraction.

7.3.1 Detector efficiency study

A detailed simulation study[2] has been performed in order to know the relative acceptance of the hybrid detector for showers induced by hadron and photon primaries.

The CORSIKA hadron sample corresponds to the sample already described in section 6.1.1, ranging from 10^{17} eV to 10^{19} eV. The photon sample, 1000 showers per energy bin, same energy range, has been generated with CORSIKA 6.600, fluka and QGSJET-II [106]. The thinning factor is 10^{-6}, the options CURVED and PRESHOWER have been switched off[3]. The showers have been resampled 5 times and simulated in a 60 degree slice centered in Los Leones Bay 4. The usual dependency of generation area on energy has been adopted to reduce the trigger inefficiency. A corresponding correction, R_i^2 / R_{max}^2, is than applied to the number of events in the efficiency calculations.

The adopted simulation algorithm is the newest release (2.2p2-mojo) validated in [140].

---

[2] in collaboration with M. Settimo and L. Perrone, Pierre Auger group, University of Lecce, Italy.[120]

[3] due to problems with the ground particle timing occurred for photons simulations using the CURVED option, currently under investigation

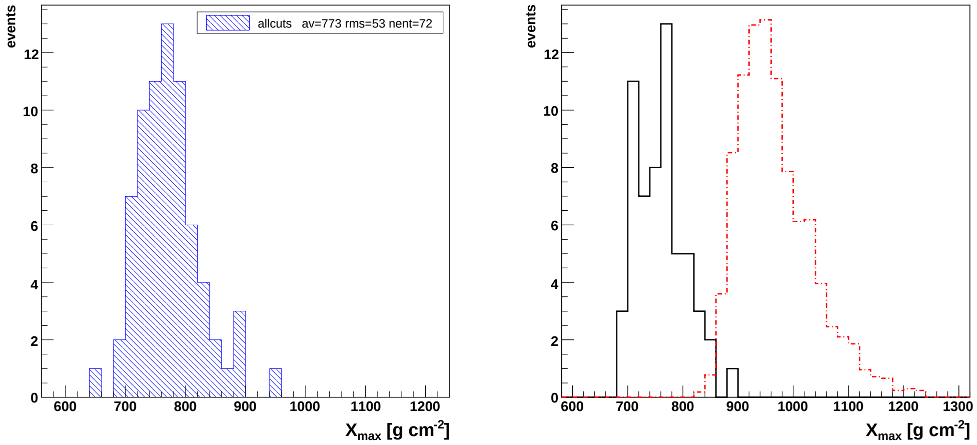

Figure 7.4: Left: distribution of depth of shower maximum for the events with energies above 10 EeV that passed the quality and fiducial cuts. Right: distribution of depth of shower maximum for the 58 candidate events selected applying the last cut (cloud coverage); the dashed red line shows a distribution for 10 EeV photons arriving over a range of zenith angles.

The simulation root output files have been transfered and processed locally. Assumptions for the atmosphere, detector calibration and fluorescence yield calculation have been made consistently throughout the simulation-reconstruction chain. The hybrid reconstruction quality requirements, defined in the previous section, have been applied to the Monte Carlo events in order to get the relative acceptance at different cut levels.
Fig. 7.5 shows the detector acceptance as a funcion of energy for the simulated primaries (photons, protons and iron nuclei) relative to protons at 10 EeV. The top panel gives the relative acceptance at hybrid trigger level, the center panel at quality cuts level, the bottom panel after applying the fiducial cuts. The number of surviving events at the different cut levels are summarised in Tab. 7.2. The values at 10 EeV agree, inside statistical error, to the study performed for [119]. The significantly lower detector efficiency for photons with respect to proton primaries, especially after the quality cuts, can be partially overcome by applying the fiducial requirements.

7.3.2 Photon candidates

The quality and fiducial cuts described in 7.2.2 have been applied to the data sample. A refined profile cut requiring the value of the difference $\chi^2_{lin}$and χ^2_{GH} to be larger than four, has been adopted. A cut on zenith angle ($\Theta < 64°$) has been introduced to be consistent with simulations.
An *a priori* cut, as already mentioned in 7.1.2, can be set for instance to the median or mean value of the photon simulation distribution. The cut efficiency is 0.5 for the median, and, due to the tails at large X_{max} , a bit smaller (~ 0.42) if we cut at the mean value of the photon distributions. The actual values of median, mean and fraction of events with X_{max} larger than the mean for the photon simulated distributions at different energies are summarised in Table 7.3. Fig. 7.6 shows the reconstructed depth of shower maximum

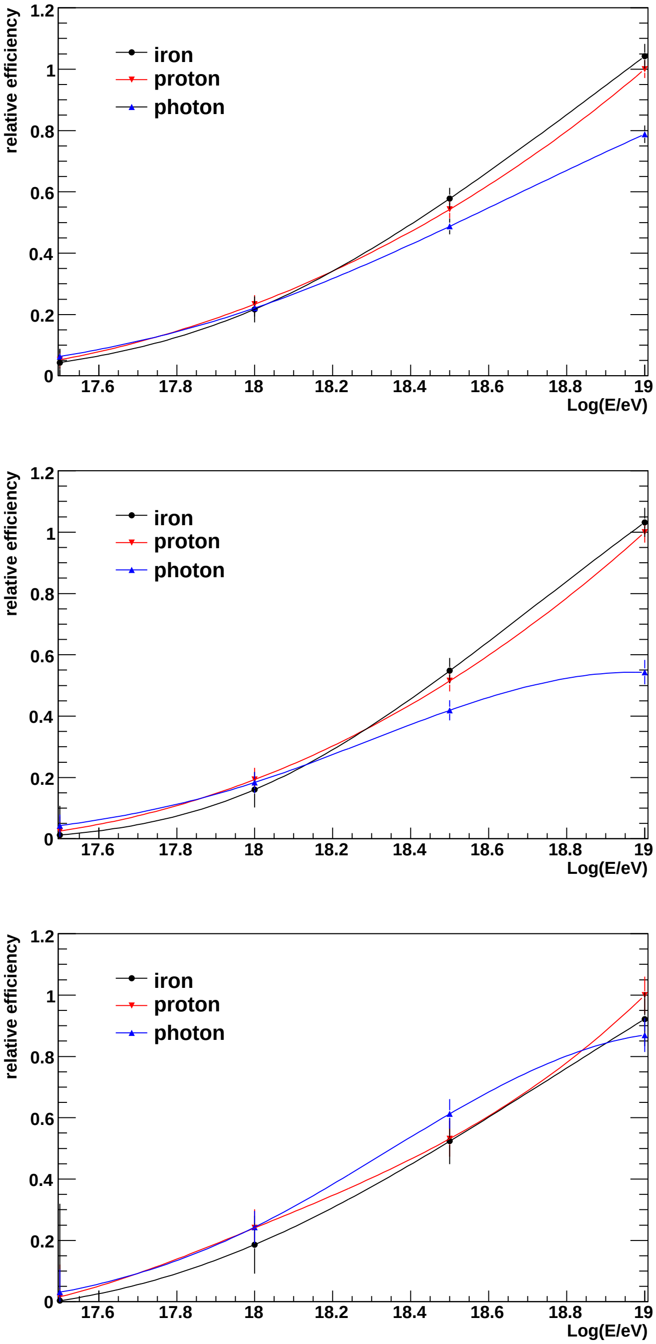

Figure 7.5: Detector efficiency for the simulated primaries relative to protons at 10 EeV. Top panel: hybrid trigger efficiency. Center panel: efficiency after applying the quality cuts. Bottom panel: efficiency after applying fiducial cuts. The values at 10 EeV agree, inside statistical error, to the study performed for [119].

Table 7.2: Generated entries, and number of events surviving the trigger, quality and fiducial cuts, for the simulated energy bins and primary particles.

Energy	Primary	generated	triggered	cut	fiducial
17.5	Pr	4243	1261	446	90
	Fe	2144	529	111	10
	Ph	4394	1580	783	181
18	Pr	3843	1124	677	270
	Fe	2059	559	301	112
	Ph	4999	1381	837	355
18.5	Pr	2878	1252	865	286
	Fe	1829	847	585	179
	Ph	3790	1480	927	434
19	Pr	3335	1187	865	277
	Fe	1685	625	451	129
	Ph	4486	1258	632	324

for data as a function of energy, for different energy thresholds, 2 and 10 EeV. The cut, marked with the red line, has been set to a value, derived from the fit of the mean value of the photon distribution for each energy, minus one sigma. In this way we perform a conservative but efficient pre-selection of candidates from the bulk of data. The selected events have been checked for cloud disturbance, in order to reject any spurious event. From this analysis we obtain a final set of six photon candidates. Their characteristic variables are summarised in Table 7.4.

A set of 1000 photon induced showers has been simulated for each event of the candidate list, with the same geometry and energy characteristics. A much more accurate selection can then be performed on event-by-event basis.

The measured depth of shower maximum (black bullets), along with the corresponding simulated photon distribution (shaded region), is shown for each candidate in Fig. 7.7. The dashed and the thick red lines indicate respectively median and mean of the simulated distribution.

Table 7.3: Median, Mean and corresponding Prob. value calculated for the shower maximum distribution of photons at different energies.

Log(Energy/eV)	Median	Mean	Prob
17	758	769	0.42
17.5	805	812	0.42
18	851	864	0.41
18.5	907	921	0.41
19	973	987	0.42

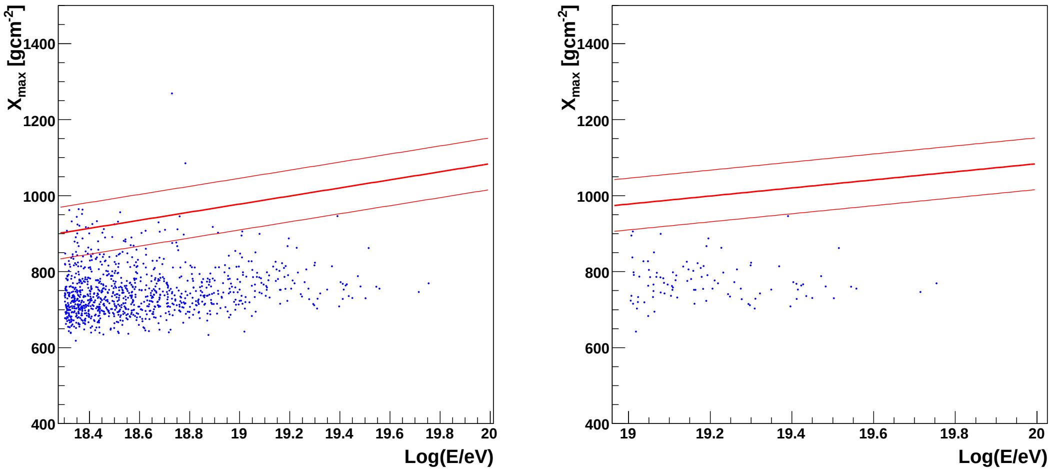

Figure 7.6: Measured depth of shower maximum as a function of energy threshold for data at different energy theresholds, 2 and 10 EeV. The thick red line shows the "elongation cut" based on a fit to the mean value of X$_{max}$ for photon simulations, the thin lines are placed at one sigma.

In Fig. 7.8 the longitudinal profile, SDP pixels, time fit, and a top view of the Auger area are displayed for one particular candidate, event sd_2051232. For this event a more detailed study has been performed in order to compare the measured shower longitudinal profile to the typical profiles obtained from photon and proton simulations. In addition to the dedicated photon sample, a set of 1000 proton induced showers with same energy and geometry configurations, has been generated. The CORSIKA files have been processed in the full detector sim-rec chain. Atmospheric and aerosols models and calibration parameters were set accordingly to the GPS time of the event.
Fig. 7.9, left panel, shows the reconstructed shower longitudinal profile for this event and the corresponding GH fit, along with typical GH profiles from the dedicated photon simulations. Fig. 7.9, right panel, shows again the data, now along with proton simulations. Typical photon profiles seem to agree much better with the data points, with respect to

Table 7.4: Characteristic variables for the six candidate events passing the photon cut.

sd_id	X_{max} [g cm^{-2}]	ΔX_{max} [g cm^{-2}]	**Energy** [EeV]	Θ [°]	Φ [°]
735338	924	23	3.2	52.4	134.3
2051232	921	16	2.3	32.1	-51.2
2201129	944	29	2.3	52.2	-124.2
2798252	932	31	2.7	48.2	127.1
3478238	964	10	2.3	38.1	24.0
3690306	925	31	2.6	41.3	-78.0

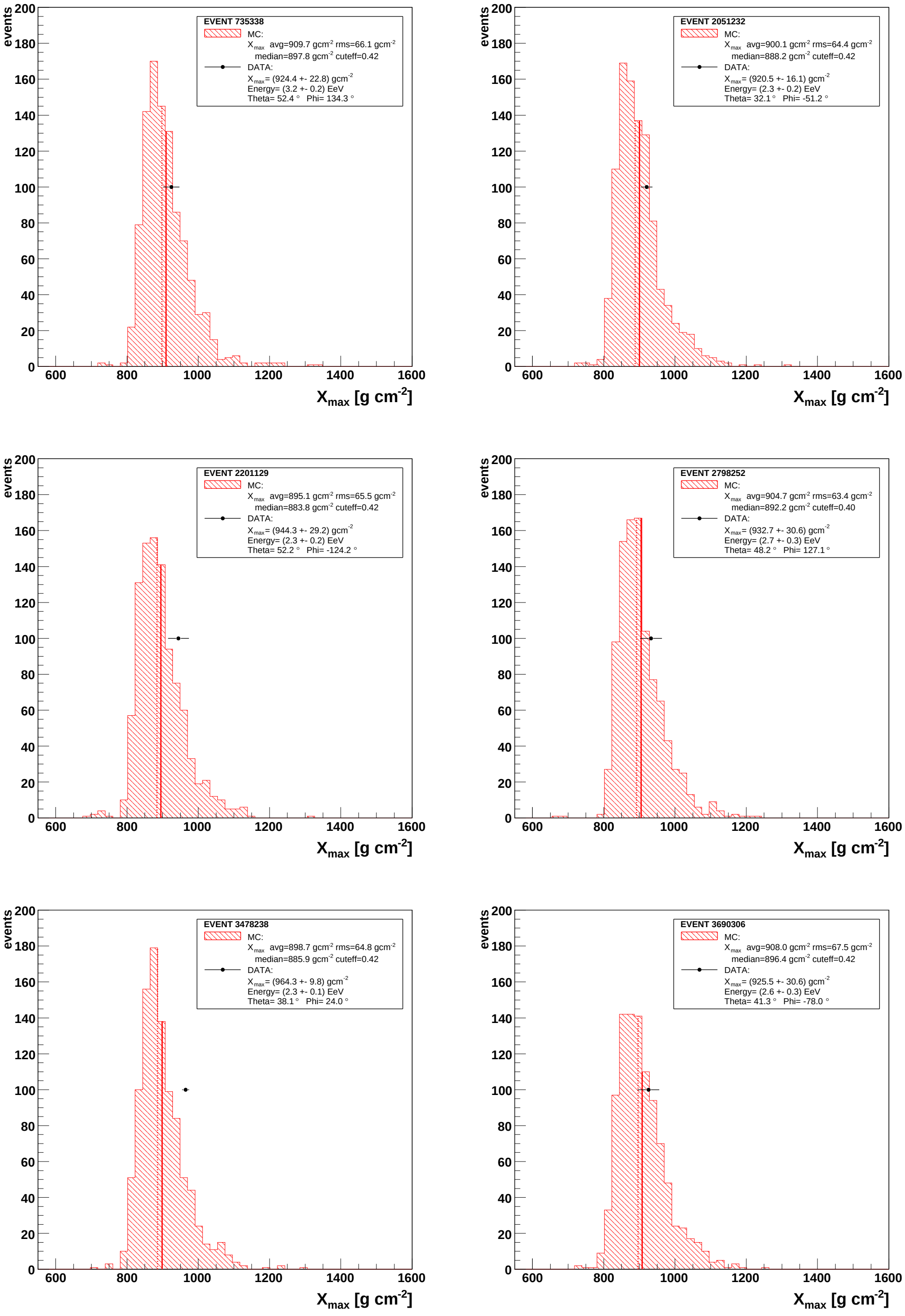

Figure 7.7: Events 1 to 6. Data point (black bullet) and statistical uncertainty superimposed to the relative simulation histogram (filled area). The thick and the dashed lines indicate respectively mean and median of the photon X$_{max}$ distribution.

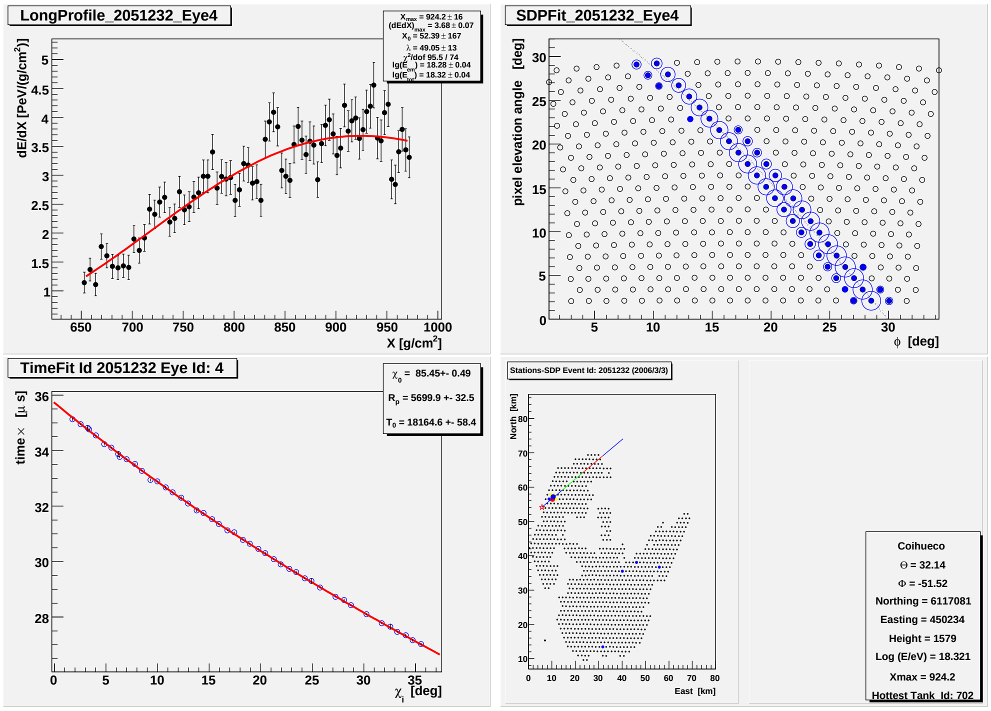

Figure 7.8: A photon candidate example: event sd_2051232. Top left: reconstructed profile; top right FD telescope view with pixel trace. Bottom left time fit, bottom right top-view of the Auger site.

proton ones. However, this is far from being a photon observation, as deep fluctuating protons are still the favoured source for this kind of events. To evaluate the correspondig proton background for this event one has to try to quantify the contamination fraction by loking at the tails of the proton X_{max} distribution.

In Fig. 7.10 the fraction of events with X_{max} above depth threshold X_{thr} as a function of X_{thr} for the proton simulations of this event is plotted (red solid line). The fraction of events above the photon candidate value (921 $\mathrm{g\,cm^{-2}}$), is below 2%. The fraction of proton contamination even if low, being this a particular selected case, is still significant. As discussed in 7.1.3, a detailed Monte Carlo study is necessary to evaluate the background contribution in order to put a stronger limit. However a raw estimate of the number of expected events from hadron tails with a X_{max} compatible with photons simulations can be given.

In Fig. 7.11 the fraction of events with X_{max} above a depth threshold X_{thr} is plotted as a function of X_{thr}, red line for showers induced by protons, black line for shower induced by iron nuclei at an energy of $10^{18.5}$ eV.

The median value of X_{max} for photons at this energy, see 7.3, is 907 $\mathrm{g\,cm^{-2}}$. This would give, in case of a pure proton composition, a fraction $\sim 3\%$ of events above the cut. Iron nuclei, with a shallower average X_{max} and smaller fluctuations give, as expected, a negligible fraction of events in the photon region. Since our proton simulation sample above $10^{18.5}$ eV, after applying all the cuts, contains ~ 240 events, it would mean 7 events above the threshold. This raw estimate is fully compatible with what we observe.

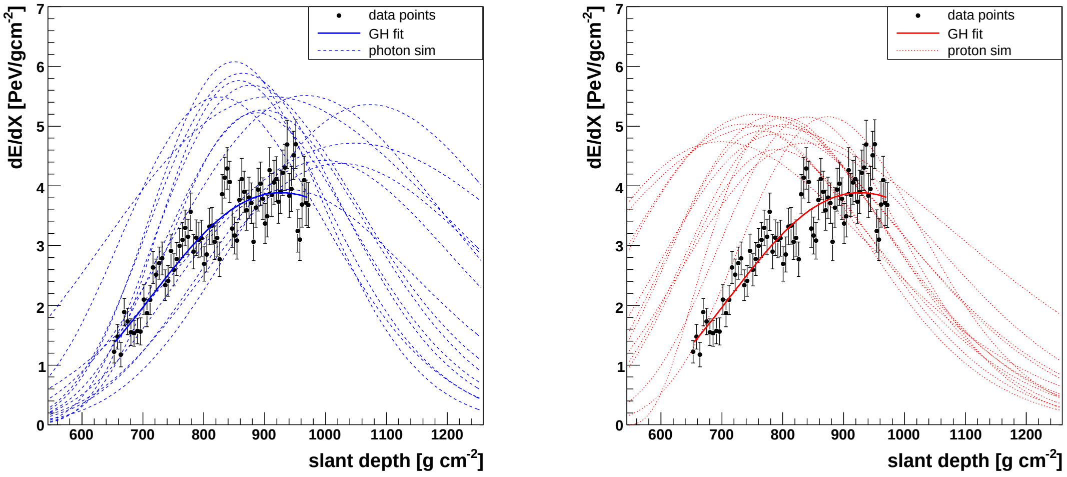

Figure 7.9: Left: measured shower longitudinal profile (black bullets with errors) along with GH fit (blue solid line) and some reconstructed longitudinal profiles (randomly selected) obtained from the dedicated photon simulations (blue dashed lines). Right: same with respect to proton induced showers (red lines).

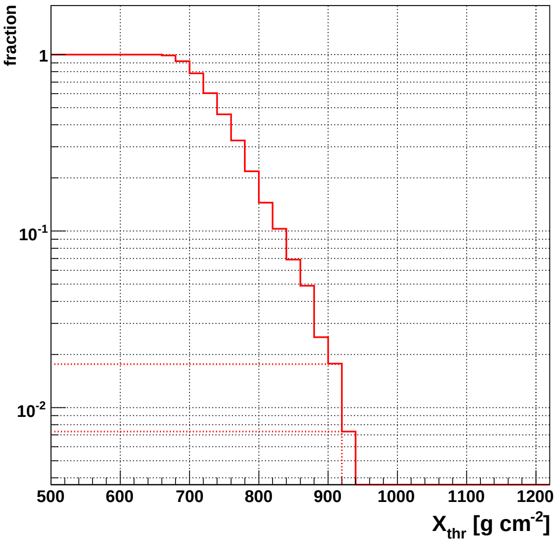

Figure 7.10: Fraction of events with X_{max} above depth threshold X_{thr} as a function of X_{thr} for the proton simulations of event sd_2051232. The fraction of events above the photon candidate value (921 g cm^{-2}) is below 2%.

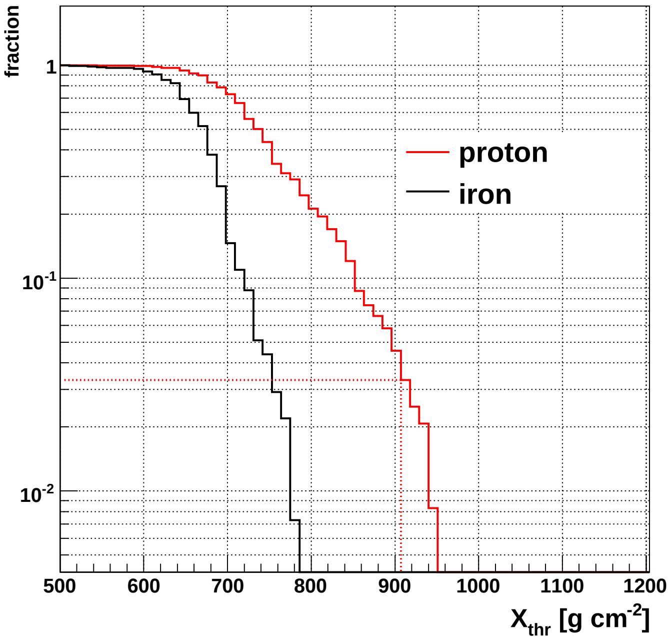

Figure 7.11: Fraction of events with X_{max} above depth threshold X_{thr} as a function of X_{thr} at an energy of $10^{18.5}$ eV. The red line is for showers induced by protons, the black line for shower induced by iron nuclei. The fraction of events above the photon mean (907 $\mathrm{g\,cm^{-2}}$) at the same energy is $\sim 3\%$ in case of protons, negligible for iron nuclei.

Table 7.5: Summary table for the integral upper limits to the photon fraction above 2, 3.16, 5, and 10 EeV. The number of photon candidates, the same at 95% c.l., the total number of events and the limits in % are displayed. A fraction of 16% has been subtracted to account for cloud coverage. The most conservative relative detector efficiency of 0.80 has been assumed. A factor 0.5, corresponding to the median cut efficiency has been taken into account.

E_{thr} [$\cdot 10^{18}$ eV]	n_γ obs	n_γ 95% c.l.	$n_{\bar{\gamma}} + n_\gamma$	f_γ^{ul}[%]
2	6	11.85	947	3.7
3.16	0	3.0	476	1.9
5	0	3.0	240	3.7
10	0	3.0	77	11.6

7.3.3 Conclusions: upper limits above 2, 3.16, 5, and 10 EeV

After the selection, a total number of 947, 476, 240, 77 events with reconstructed energy larger than 2, 3.16, 5 and 10 EeV respectively, survived. Table 7.5 summarises for each energy threshold the number of detected photon-like events, and expected at 95% confidence level, the total events ($n_{\bar{\gamma}} + n_{\gamma}$), and finally the derived integral upper limits to the photon fraction. An estimation for the fraction of cloud obscured events has been taken into account, the value assumed is 16%, as calculated for [110]. For the relative detector acceptance correction we conservatively assume the minimum value of $\epsilon = 0.80$, for the cut efficiency $f = 0.5$ corresponding to the cut at the median.

The derived upper limits are shown in Fig. 7.12 (blue markers), along with previous experimental limits and model predictions. Above 10 EeV the result is limited by statistics, but represents a independent confirmation of the Auger SD result, as already pointed out in [21]. The first bounds at lower enegy, above 5 EeV and 3.16 EeV, are instead significantly constraining the SHDM and TDs models, extending the Auger SD results. A factor ~ 10 more statistics is needed to reach sensitivity for testing the Z-Burst model predictions. The limit above 2 EeV is to high to constrain any model, but we underline that the calculation is very conservative, with respect to energy threshold, detector acceptance corrections and background subtraction.

Finally, the photon search with the hybrid data is expected soon to benefit from the significant increase of statistics, when taking into account the data recorded from the other two fluorescence telescopes, which were not yet in operation or fully calibrated.

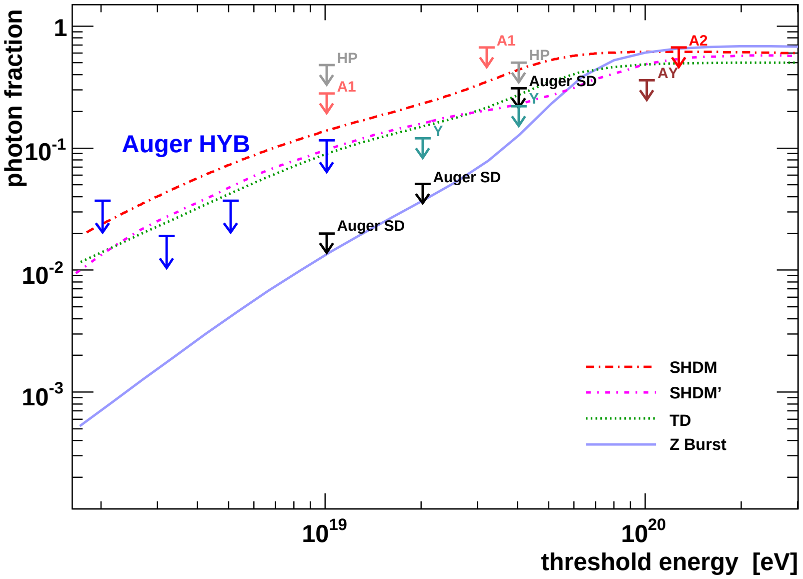

Figure 7.12: Upper limits to the photon fraction in the integral cosmic rays flux for different experiments: AGASA (A1, A2), AGASA-Yakutsk (AY), Yakutsk (Y), Haverah Park (HP), for references see Fig. 3.9 [132]. In black the limits from Auger surface array (Auger SD) [21] and finally in blue the limits above 2, 3.16, 5, and 10 EeV derived in this work (Auger HYB).

7.4 Impact of a photon contamination on the measurement of the p-air inelastic cross section

We shortly discuss here the impact of a photon contamination on the estimate of the inelastic proton air cross section σ^{inel}_{p-air} at the highest energies. This quantity can be derived experimentally from the measurement of the depth of shower maximum exploiting the correlation between X_{max} and the depth of the first interaction, as done for Fly's Eye in [17]. See [37] for a comprehensive fit of the Fly's Eye and AGASA [81] measurements with the accelerator data.
The procedure is however not straighforward, as the observed shower attenuation length depends highly on the rate of energy dissipation into the detected electromagnetic component. The probability of having an interaction at a depth X_{int} larger than X is decreasing exponentially as follows:

$$P\left(X_{int} > X\right) \propto \exp\left(-X/\lambda_{int}\right) \tag{7.13}$$

where $\lambda_{int\ (p,air)} = < m_{air} > / \sigma^{inel}_{p-air}$ and $< m_{air} >$ is the mean mass of the air nuclei (14.54 g/mol).
If we could neglect the instrinsic shower fluctuations, the correlation between X_{max} and X_1 would be perfect and the shape of the distributions preserved. Their effect can however be expressed by a multiplicative factor k, which includes interaction model features and detector response. The probability of having a value of X_{max} larger than X is:

$$P\left(X_{max} > X\right) \propto \exp\left(-X/\Lambda\right) \tag{7.14}$$

where $\Lambda = k \cdot \lambda_{int}$ is the shower attenuation length.
Given the k factor, the interaction length can be derived and the σ^{inel}_{p-air} measured, see also [26] for HIRES data, and [135] for a preliminary estimate with the Auger FD and Hybrid data.
As a matter of fact, the X_{max} distribution tail is not a single exponential, this introduces a large dependence of k on the fitted region. If the fit starting point is too close to the distribution peak the measurement would be, for instance, more sensitive to heavier elements contamination. At large X_{max} instead the statistical errors grow. The dependence of the slope value and fit error from the fit starting point is shown in Fig.7.13.
Accurate simulation studies with large statistics have been performed in [6]. The sensitivity of this measurement and the systematics have been recently re-discussed in [151].
To show how much could a photon contamination affect the estimate of the σ^{inel}_{p-air} a sample of 10000 CORSIKA[4] showers induced by protons of energy $10^{18.5}$ eV has been generated. In Fig.7.14 left panel, the distribution of the depth of shower maximum (thick red line) is shown with a fit of the slope 100 $\mathrm{g\,cm^{-2}}$ after the X_{max} . The distribution of depth of first interaction, shifted by 500 $\mathrm{g\,cm^{-2}}$ is shown too (dashed red line). Dealing with a real detector the uncertainty in the determination of the shower maximum has to be taken into account. The effect of a finite detector resolution on the X_{max} distribution is shown in Fig. 7.14, right panel. The smearing of the distribution results in a broader portion around the maximum, but the slope of the tails is only slightly affected. This demonstrates the proper choice of the X_{max} cut, in agreement with the previously cited work.

---

[4] uniform zenith distribution, thin 10^{-5}, high energy interaction model QGSJETII

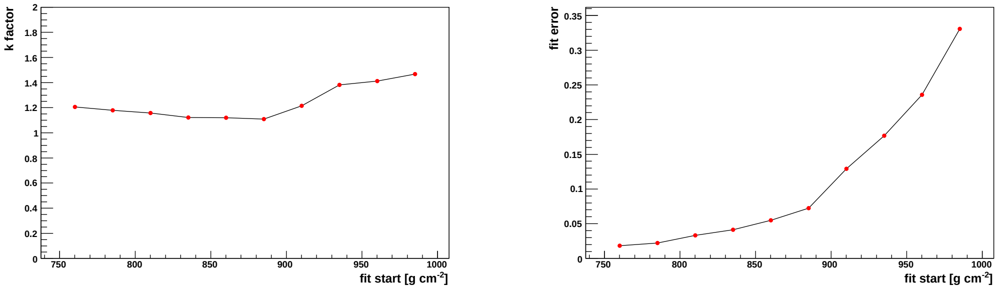

Figure 7.13: Dependence of the k factor and relative error from the fit starting point.

The effect of a contamination of 30% iron nuclei together with the finite detector resolution has also been tested. Again the effects combine in a broader region around the peak but the change in the slope is minimum if the fit is performed at a sufficient distance from the maximum. The contamination from lighter elements, for instance Helium nuclei, could preclude the σ^{inel}_{p-air} measurement itself, as has been stated recently in [150]. A better knowledge of the primary composition is necessary to overcome their correlation.
Given the limits derived in the previous section we show the effect of a photon contamination, of the order 2%, 3.5%, 5% and 10%, in our proton sample. Photons directly contribute to a bias towards deeper X_{max} , which can't be avoided restricting the fit range of the far tail of the distribution. The derived attenuation lenght is larger of a factor 8% 17%, 26% and 37% resulting in a corresponding reduction of the derived σ^{inel}_{p-air} .

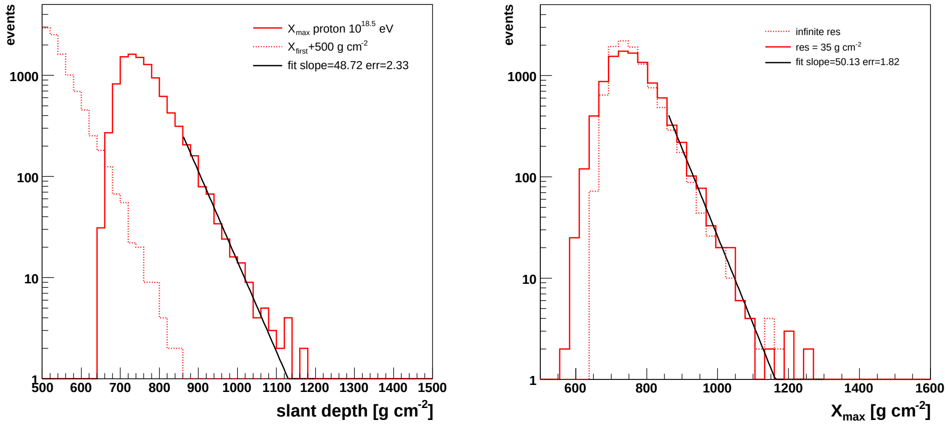

Figure 7.14: Left: distribution of depth of maximum for simulated showers induced by protons at $10^{18.5}$ eV (thick red line), along with distribution of depth of first interaction X_1 shifted by 500 g cm^{-2} . (dashed red line). Left: smearing effect of a finite detector resolution (thick red line) compared to infinite resolution (dashed red line). ΔX_{max} =35 g cm^{-2} as for HIRES [27], while the resolution for Auger is ∼20 g cm^{-2} [47]. An exponential fit to the slope of the tail 100 g cm^{-2} after peak is also shown.

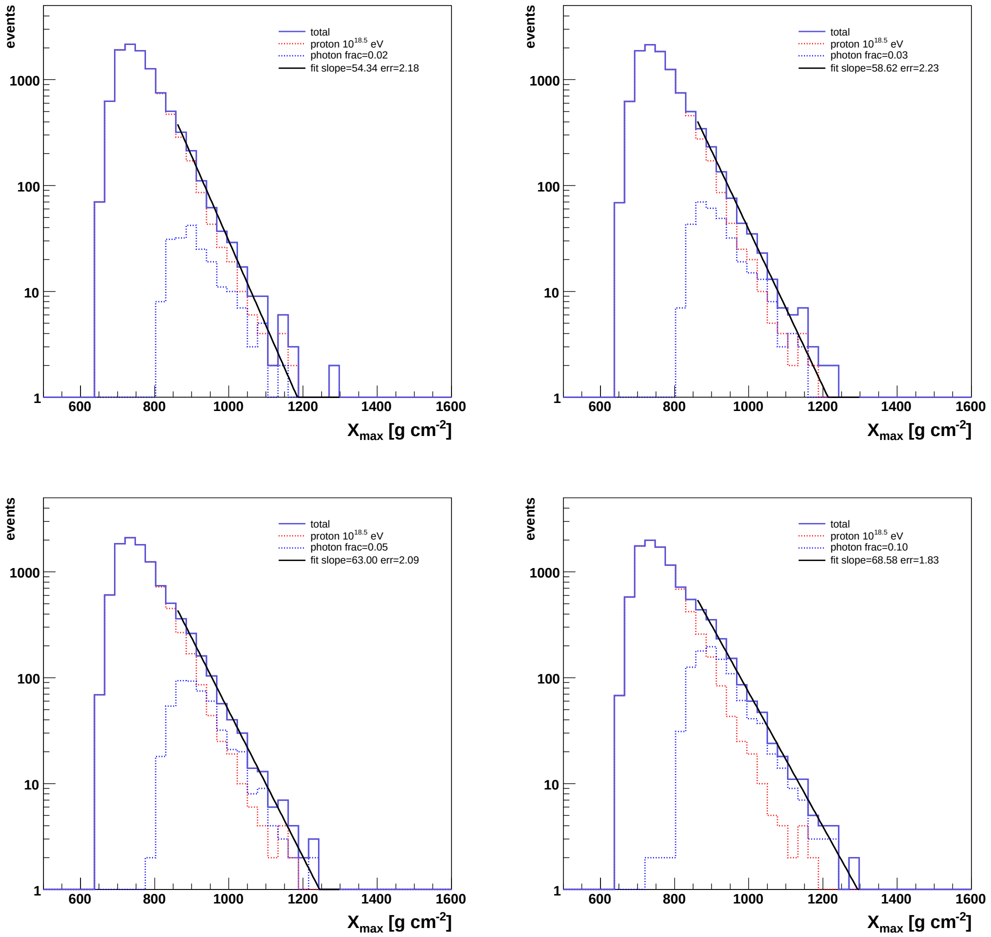

Figure 7.15: Effect of a photon contamination of 2%, 3%, 5% and 10%. The corresponding relative change in the slope is 8%, 17%, 26% and 37%. The cross section measurement would be reduced accordingly.

Summary and outlook

In this work the performance of the Pierre Auger Observatory has been studied in detail and a search for photons as cosmic ray primaries has been performed over a wide energy range.
Large photon fractions at ultra high energies are predicted by the non-acceleration models, based on decay or annihilation of exotic particles of GUT scale masses. Moreover, photons are predicted as product of the GZK processes in the interaction of nucleons with the cosmic microwave background. However no UHE photon detection has been claimed so far. Limits to the fraction of photons in cosmic rays have been set previously by ground experiments only.
The Pierre Auger Observatory, with its hybrid design, profits of an accurate determination of the geometrical parameters and of the direct observation of the shower longitudinal development. Moreover the detector provides a large exposure and full sky coverage, possibly opening a way for cosmic ray astronomy at the highest energies.
The main outcomes of this work are summarised as follows.

- The fluorescence telescopes of the Pierre Auger Observatory consist of a total of 11 000 optical modules. Half of them have been tested and qualified with a highly automatised test setup. Details on the experimental requirements and test results are presented in Section 4.3, (see [24]).

- The performance of the fluorescence detector (FD) reconstruction algorithm has been studied at different selection levels with dedicated simulations. In Chapter 5 the FD trigger efficiency and the geometry resolutions are calculated. A realistic estimate of the hybrid resolution of the physics observables (depth of shower maximum and energy) has been given, see [108].
  The extension of the reconstruction capabilities to the highest energies has been achieved after a detailed study of the FD saturation region (energy-distance). The FD electronics employs a double gain system which allows to cover a large signal dynamic range (15 bits) with 12 bits ADC converters A. A new technique has been implemented to recover events eventually exceeding the signal range of the high gain channels by using the low gain channels information, significantly improving the performance of the full simulation-reconstruction chain, see [136].

- Given a reliable reconstruction algorithm, we investigated the composition sensitivity of different parameters connected to the depth of shower maximum and the shape of the longitudinal shower profile, testing fits with different functional forms. A Principal Component Analysis (PCA) has been performed in order to improve the hadron-photon separation power of a simple X_{max} cut compared to the one achievable combining other sensitive observables, like for instance the width of the shower profile or the depth of the first interaction. A clear enhancement has been found, see [139]. The analysis on the reconstructed Monte Carlo sample, has been extended to quantify the sensitivity after full hybrid detector simulation.

- An update of the result reported in [119] (a limit to the fraction of photons in cosmic rays above 10 EeV), has been performed, based on the depth of shower maximum as discriminating observable. This analysis includes one more year of data. The current result above 10 EeV is 13% at 95% c.l., see [21].
  As a next step the analysis has been extended at lower the energies in order to benefit from a factor $\sim (E/10^{19})^{-3}$ larger statistics. The challenge is now to set the limit in a region where the hybrid detector efficiency may drop below 100%. This is only possible after a detailed study of the relative acceptance for hadron and photon primaries, via a full hybrid detector simulation.
  The Auger hybrid data collected between February 2004 and July 2007 in two of the four fluorescence telescopes are used in this analysis. An appropriate statistical method for dealing with a large data sample has been applied (section 7.1.2). The derived upper limits at 95% c.l. are 3.7%, 1.8%, 3.7% and 11.6% respectively above 2 EeV (6 candidate survived), 3.16, 5 and 10 EeV (0 candidates survived). These results are consistent with a raw estimate of the hadron background, see 7.3.

- The measurement of the proton air inelastic cross section at energies beyond man-made accelerators is one of the challenges of the cosmic rays experiments. The impact of a photon contamination on this measurement has been studied. The derived attenuation length is larger of a factor 8%, 17%, 26% and 37% resulting in a corresponding reduction of the derived σ_{p-air}^{inel} .

Final remarks

The figure shows the limits derived in this analysis plotted along with results from the previous experiments at higher energies. The limit confirms the strong constraints to the non-acceleration models (SHDM, SHDM' and TD) and in turn highly favor the astrophysical scenarios for the origin of UHE cosmic rays.
The PAO southern site will be completed by the beginning of 2008. Its large exposure will rapidly improve the hybrid detector sensitivity (a factor ~ 10 in ~ 2 years). Combining different observables connected to the shower development in the atmosphere is a crucial point, which could highly enhance the hadron-photon separation power as we stated in Chapter 6. Moreover the hybrid design of the Pierre Auger Observatory offers the unique opportunity to perform a combined study including the observables from the surface detection technique. This will be the natural next step of this work.

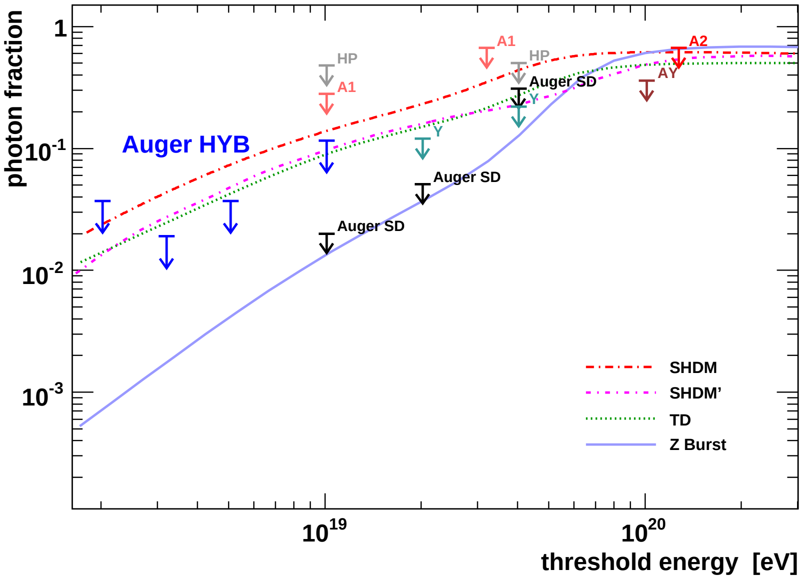

Upper limits to the photon fraction in the integral cosmic rays flux for different experiments, for references see Fig. 3.9. In black the limits from Auger surface array (Auger SD) [21] and finally in blue the limits above 2, 3.16, 5, and 10 EeV derived in this work (Auger HYB).

Appendix A

Fluorescence detector electronics: the virtual channel

A.1 The virtual channel working principle

The dynamic range of the fluorescence detector recorded signal runs from 3 to almost 10^5 photoelectrons/100ns, which means about 15 bits. An optimal solution to provide the dynamic range compression to the 12 bits analog to digital converters has been implemented in the analog electronics design, see [114, 11].

Each analog board carries 24 FADCs, 22 for the normal channel (high gain), 2 for the virtual channel (low gain). Exploiting the fact that channels don't trigger at the same time, but rather in a time sequence, the system can handle pulses with amplitudes beyond the saturation limit of the normal PMT readout.

Fig A.1 shows the sketch of the virtual channel electronics. Parallel to the normal readout, the virtual readout records the sum of 11 non adjacent even (or odd) normal channels belonging to the same column.

If a normal channel saturates, the information on the signal can be recovered looking at the virtual channel and subtracting time-bin wise the contribution of the not saturated PMTs. The signal of the i-th PMT can be retrieved through the following relation:

$$s_{n_i} = \left[\frac{s_v}{g_v} - \sum_{j \neq i} \left(\frac{s_{n_j}}{g_{n_j}} \right) \right] g_{n_i} \tag{A.1}$$

where s_v is the signal in the corresponding virtual channel, g_v is the virtual channel gain, the sum runs on the triggered PMTs contributing to the virtual trace in the same time-bin, s_{n_j} are the signals in the normal channels, g_{n_j} are the normal gain factors and g_{n_i} the gain of the i-th normal channel.

Fig A.2 shows the display of a simulated shower with saturation occurring in some of the normal channels. The camera sky view for the recorded event is shown in the left panel; the selected traces and the corresponding virtual trace are visualized in the right panel.

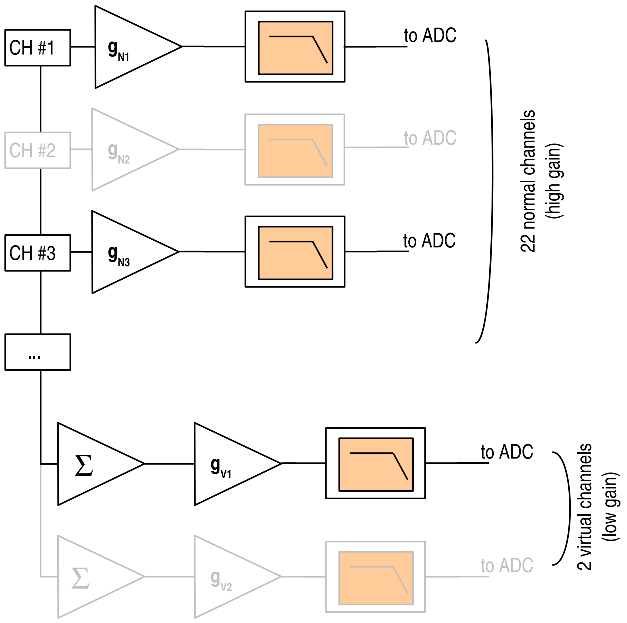

Figure A.1: Sketch of the analog electronics showing the working principle of the virtual channel. Parallel to the normal readout (high gain channels) the signals of 11 odd-numbered (and even-numbered) channels in a column are summed up and driven to the corresponding virtual channel (low gain channel). In case of saturation of the normal ADC, the information on the collected charge can be restored from the virtual.

A.2 Implementation in the simulation-reconstruction framework

The Fluorescence Detector simulation software FDSim has been described in [125]. The FdTriggerSimulator module has been modified in order to build the virtual traces from the corresponding normal channels and export them in the output file. The gain ratio can be set in the simulation datacard in order to study its impact on the reconstruction. FDSim has been lately integrated in the Offline [10], the complete simulation-reconstruction framework for the Pierre Auger Observatory.

The changes in the reconstruction sequence have been implemented at its first step, right before the end-to-end calibration constants are applied. The FdCalibrator module, responsible for extracting the photon traces from the raw ADC data, has been modified in order to read and store all the traces, including the virtual channels, belonging to the list of the triggered PMTs.

The first added method, *LoadADC()*, performs a bin-per-bin check on the PMT traces for ADC overflow. In the eventuality of saturation in one or more bins, the corresponding

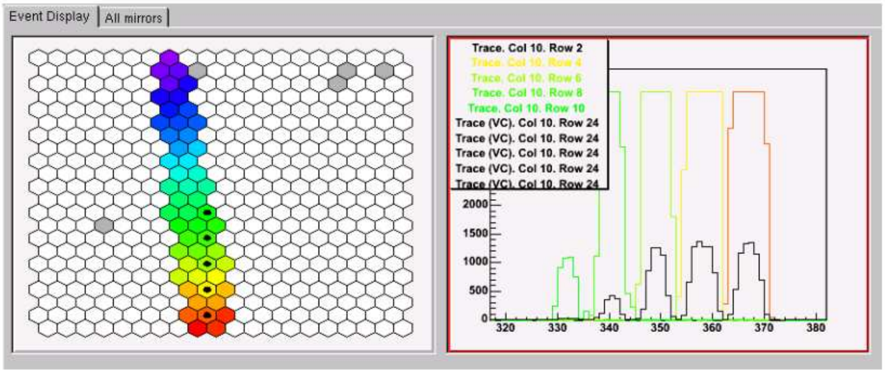
Event Display
All mirrors
Trace. Col 10. Row 2
Trace. Col 10. Row 4
Trace. Col 10. Row 6
Trace. Col 10. Row 8
Trace. Col 10. Row 10
Trace (VC). Col 10. Row 24
Trace (VC). Col 10. Row 24
Trace (VC). Col 10. Row 24
Trace (VC). Col 10. Row 24
Trace (VC). Col 10. Row 24
2000
1500
1000
500
0
320
330
340
350
360
370
380

Figure A.2: Display of a simulated event. Left panel: camera sky view with the pixels triggered by the shower; the color code reflects the time sequence from violet to red. Right panel: traces recorded in the selected pixels, four of which are saturated; in black the trace of the corresponding virtual channel.

channel flag is set to 1 and the first saturated bin (FSB) and last saturated bin (LSB) numbers are stored.
The calibration of the traces is performed as usual in case of no saturation. Instead, in case of positive flagged channel, the method *ADCReloaded()* is called to substitute the saturated trace bins (between the FSB and LSB) with the corresponding virtual channel bins scaling them by the relative gain ratio. The method performs also the subtraction of the contribution from other triggered pixels in the same virtual channel at the same time. The usual calibration constants can then be applied to the recovered traces, in order to get photons per 100ns time bin from the integer pixel ADC traces. In case of time overlap between saturated traces or saturation of the virtual channel itself, i.e. unrecoverable saturation, the module exits with a failure message.
Fig.A.3 left shows an example of a saturated photon trace (photons/100ns time bins) in a simulated event. The central plot shows the recovered photon trace and at the right plot the corresponding virtual channel raw trace (ADC/100ns time bins).

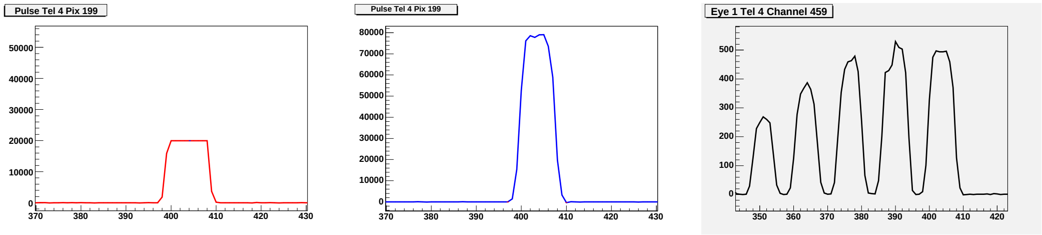

Figure A.3: Left the saturated trace in pixel 199 (photons/100ns vs time bins), center the photon trace after recovery. Timebins from 400 to 408 have been substituted according to A.1. The right plot shows the raw signals in the corresponding virtual channel 459 (ADC/100ns vs time bins) from which the ADC values have been reloaded.

The necessary modifications have been made to the *ChannelRecData* class belonging to the Framework/FEvent, which contains the ADC integer traces with pedestal.

The saturation flag and the relative setters and getters functions have been added to the code. The first and last saturated time bins are also saved here.

FdCalibratorWG: module settings

The FdCalibratorWG (Wuppertal Group) has been released together with a dedicated technical note (GAP-2006-104), and is part of the offline CVS repository. The module settings can be chosen via a xml file. The following options have been added to the existing FdCalibrator.xml parameters:

- <**fixedCalibConst**> value to be used as the fixed calibration constant when the database is switched off (default 5.0)
- <**saturationRecoveryMode**> saturation recovery mode (default active = 1)
- <**virtualRatio**> fixed value for the relative gain ratio (default 20.0)
- <**border**> time bins around the saturated part of trace to be also loaded from the virtual channel (default 0).

In the next future the monitoring database is being filled, on nightly base, with the operating values of the calibrations and the measured relative gain ratios. The baseline value and RMS noise of each channel will also be monitored and included in the recovery method.

Appendix B

Cuts and candidates

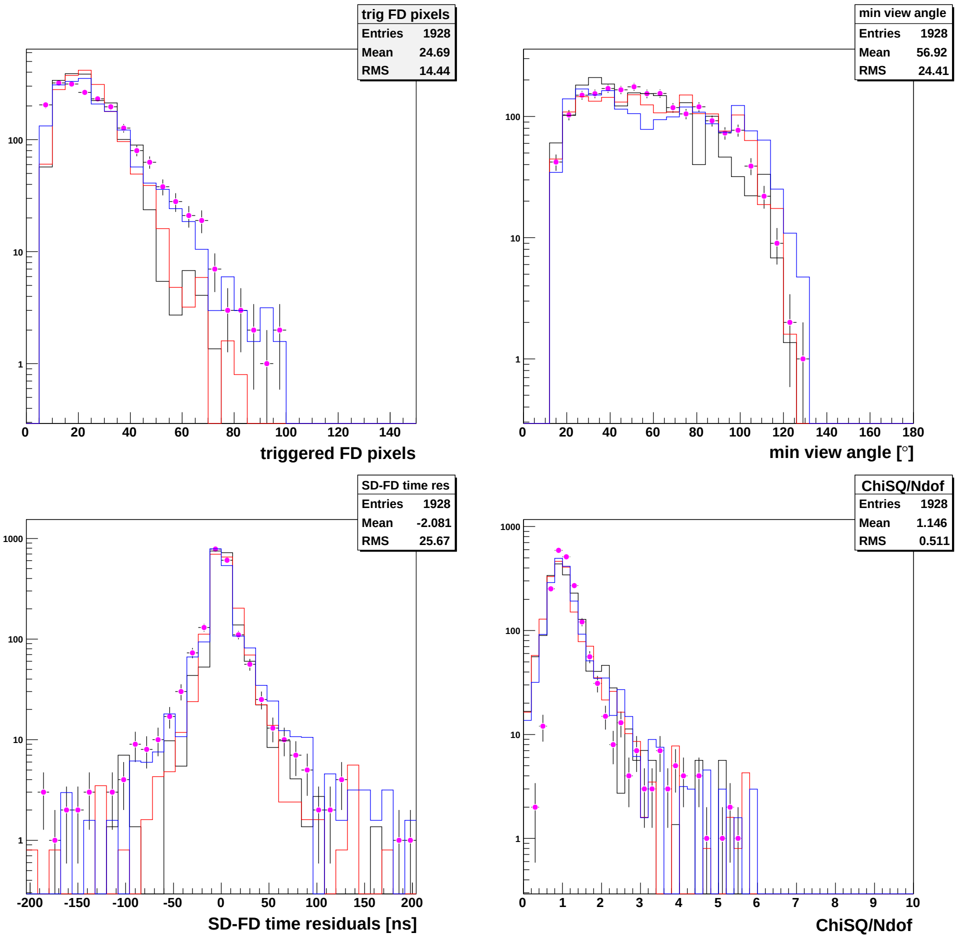

Figure B.1: Variables distributions after applying quality cuts for data (pink bullets), along with simulations for proton (red), iron(black) and photon (blue). Top panel: number of FD triggered pixels and minimum angle between FD pixel directions and shower axis. Bottom panel left: distribution of FD-SD time residuals (SD measured time and tank trigger time estimated from FD). Right: normalized Gaisser-Hillas χ^2 distribution.

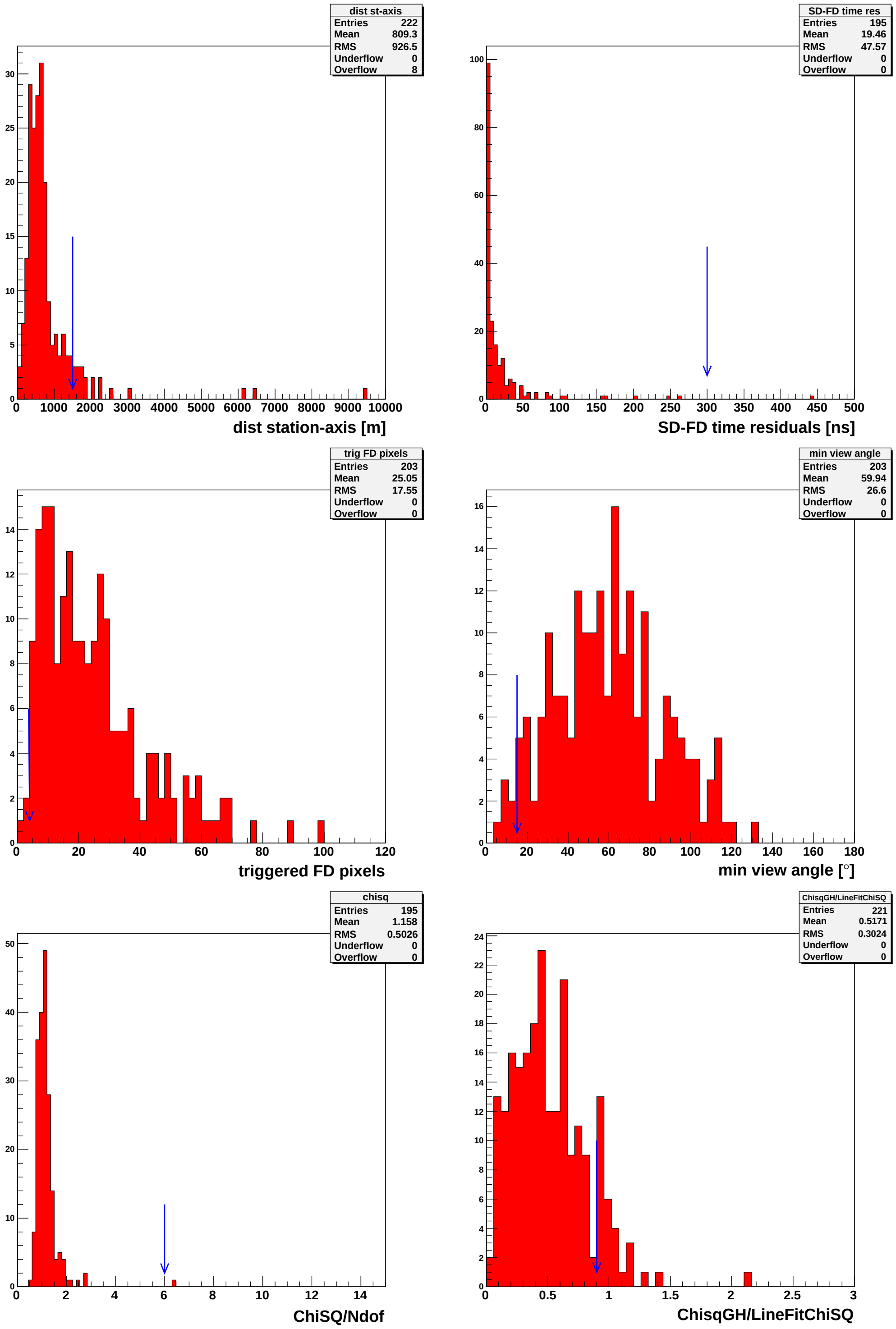

Figure B.2: N-1 plots, obtained with all quality cuts exluding the one on the plotted variable. Top panel: distance between shower axis and hottest SD tank and distribution of FD-SD time residuals (SD measured time and tank trigger time estimated from FD). Central panel: number of FD triggered pixels and minimum angle between FD pixel directions and shower axis. Bottom panel: normalized Gaisser-Hillas χ^2 distribution and χ^2GH / Lineχ^2.

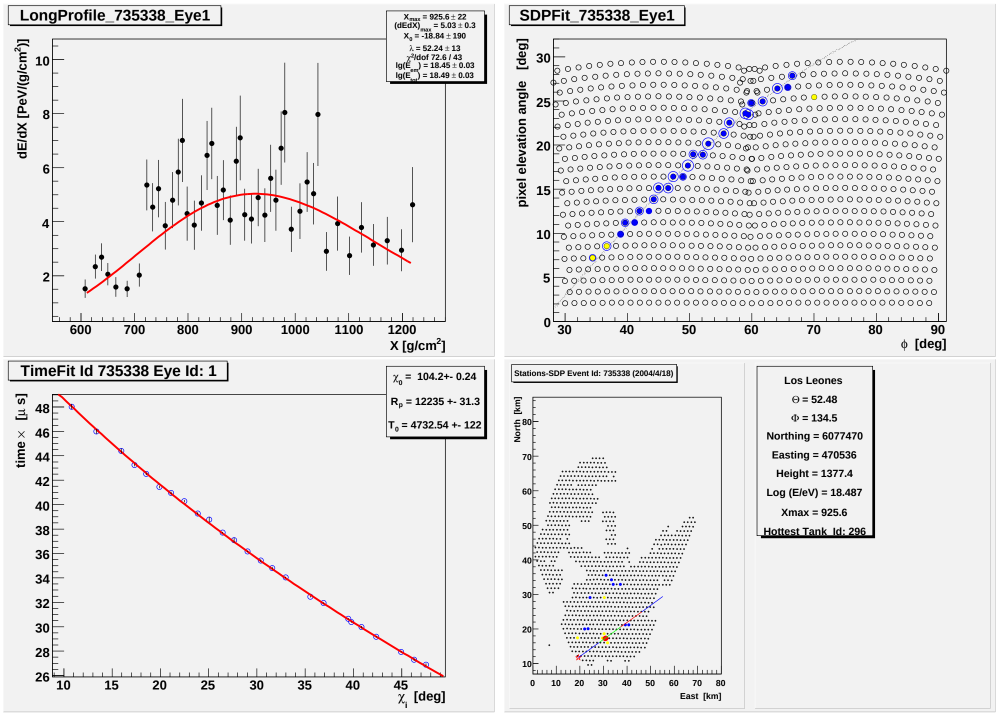

Figure B.3: Photon candidates above 2 EeV: event sd_735338

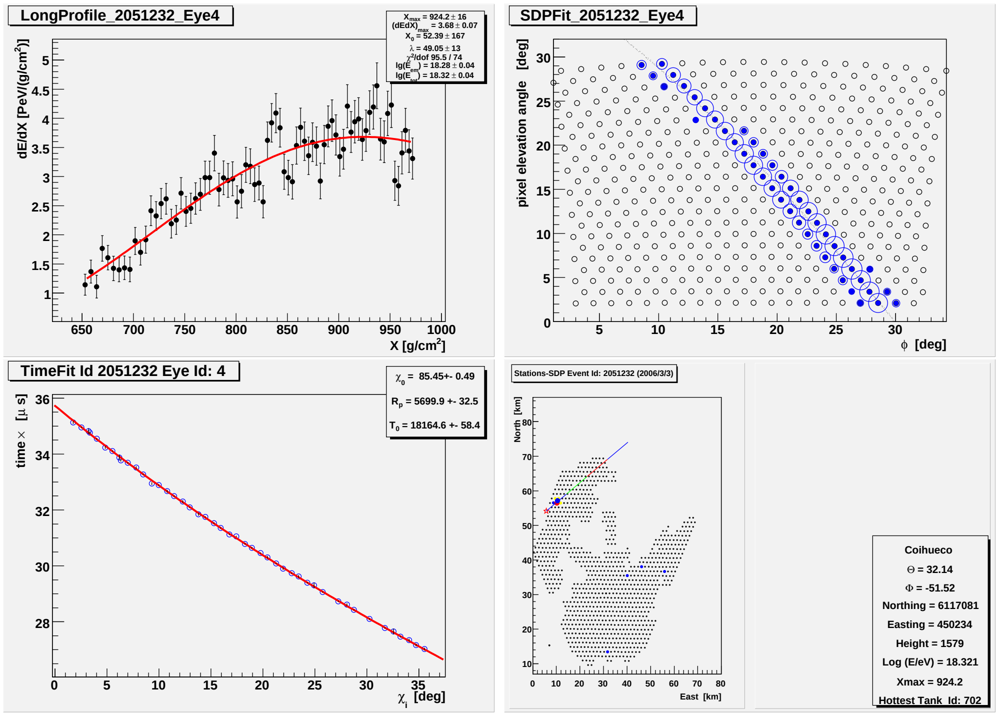

Figure B.4: Photon candidates above 2 EeV: event sd_2051232

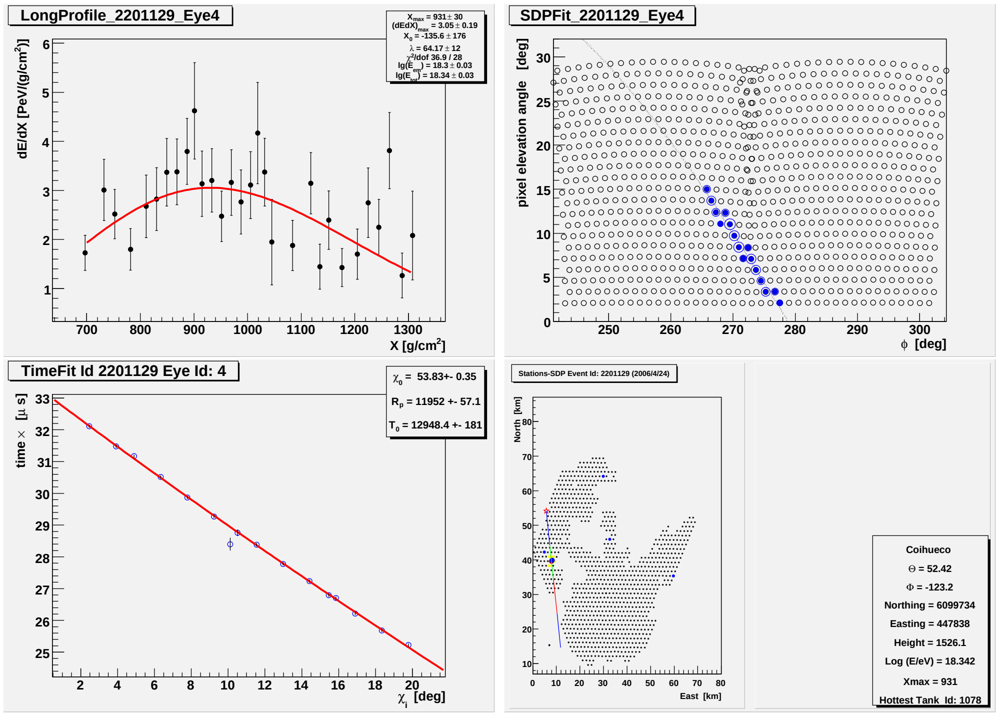

Figure B.5: Photon candidates above 2 EeV: event sd_2201129

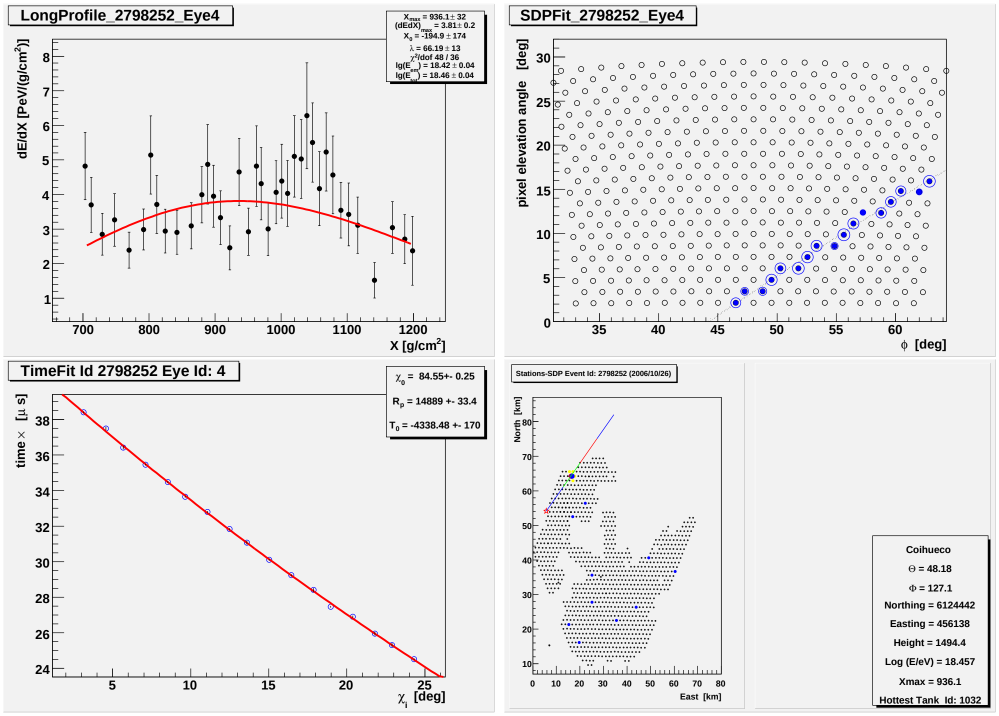

Figure B.6: Photon candidates above 2 EeV: event sd_2798252

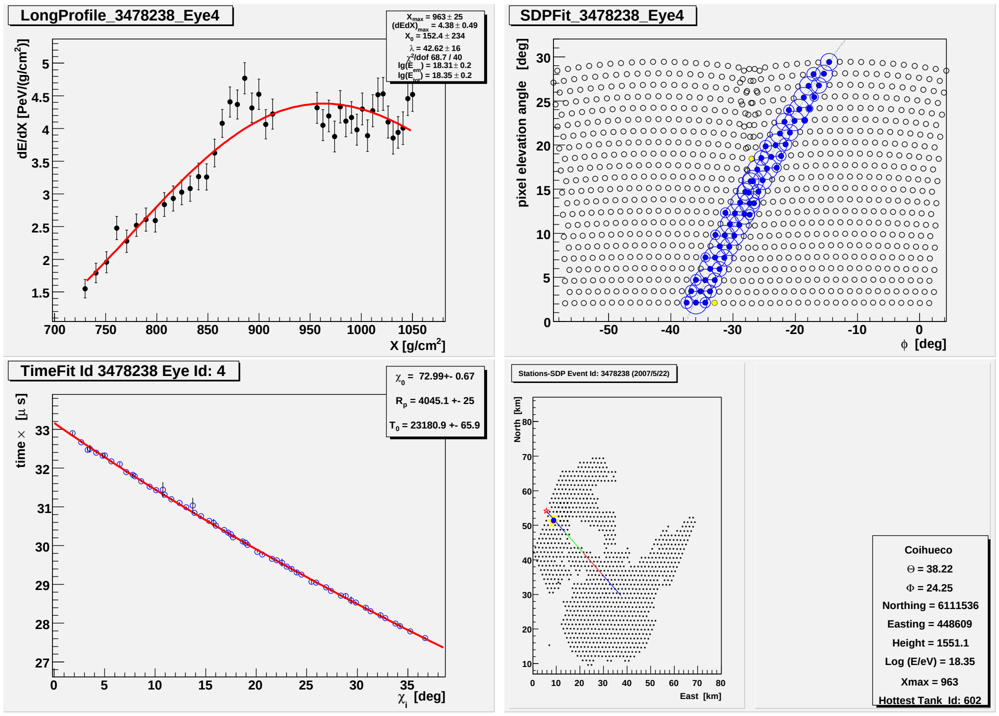

Figure B.7: Photon candidates above 2 EeV: event sd_3478238

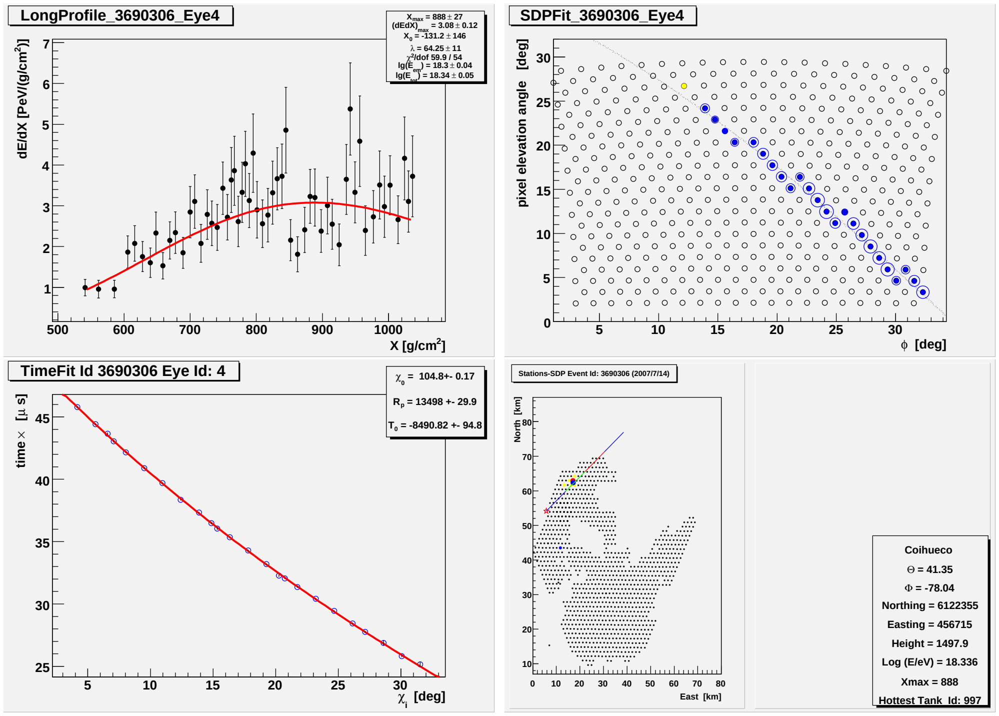

Figure B.8: Photon candidates above 2 EeV: event sd_3690306

Bibliography

[1] R. U. Abbasi for the HiRes collaboration, "Observation of the ankle and evidence for a high-energy break in the cosmic ray spectrum," *Phys. Lett.* **B619** (2005) 271–280, `astro-ph/0501317`.

[2] AGASA Collaboration, "The Anisotropy of Cosmic Ray Arrival Directions around 10^{18} eV," *Astroparticle Physics* **10** (1999) 303.

[3] D. Allard, E. Parizot, and A. V. Olinto, "On the transition from Galactic to extragalactic cosmic-rays: spectral and composition features from two opposite scenarios," *ArXiv Astrophysics e-prints* (Dec., 2005) `astro-ph/0512345`.

[4] P. Allison *et al.*, "Timing Calibration and Synchronization of Surface and Fluorescence Detectors of the Pierre Auger Observatory," in *International Cosmic Ray Conference*, vol. 8 of *International Cosmic Ray Conference*, pp. 307–+. 2005.

[5] R. Aloisio, V. Berezinsky, P. Blasi, and S. Ostapchenko, "Signatures of the transition from galactic to extragalactic cosmic rays," *ArXiv e-prints* **706** (June, 2007) `0706.2834`.

[6] J. Alvarez-Muñiz, R. Engel, T. K. Gaisser, J. A. Ortiz, and T. Stanev, "Influence of shower fluctuations and primary composition on studies of the shower longitudinal development," *Phys. Rev. D* **69** (May, 2004) 103003–+, `arXiv:astro-ph/0402092`.

[7] L. A. Anchordoqui and for the AUGER Collaboration, "The Pierre Auger Observatory: Science Prospects and Performance at First Light," *ArXiv Astrophysics e-prints* (Sept., 2004) `astro-ph/0409470`.

[8] L. Anchordoqui, T. Paul, S. Reucroft, and J. Swain, "Ultrahigh energy cosmic rays: The state of the art before the auger observatory," `hep-ph/0206072`.

[9] T. Antoni *et al.*, "Kascade measurements of energy spectra for elemental groups of cosmic rays: Results and open problems," *Astropart. Phys.* **24** (2005) 1–25, `astro-ph/0505413`.

[10] S. Argiro, S. L. C. Barroso, J. Gonzalez, L. Nellen, T. Paul, T. A. Porter, L. Prado, Jr., M. Roth, R. Ulrich, and D. Veberic, "The Offline Software Framework of the Pierre Auger Observatory," *ArXiv e-prints* **707** (July, 2007) `0707.1652`.

[11] S. Argiro *et al.*, "The analog signal processor of the auger fluorescence detector prototype," *Nucl. Instrum. Meth.* **A461** (2001) 440–448.

[12] G. A. Askaryan *Sov. J. Atom Energy* **2** (1957) 921.

[13] P. Auger, P. Ehrenfest, R. Maze, J. Daudin, and R. A. Fréon, “Extensive cosmic-ray showers,” *Rev. Mod. Phys.* **11** (Jul, 1939) 288–291.

[14] M. Ave, J. A. Hinton, R. A. Vazquez, A. A. Watson, and E. Zas, “Constraints on the ultra high energy photon flux using inclined showers from the haverah park array,” *Physical Review D* **65** (2002) 063007.

[15] M. Ave, J. A. Hinton, R. A. Vázquez, A. A. Watson, and E. Zas, “Composition sensitivity of the auger observatory through inclined showers,” *Phys. Rev. D* **67** (Feb, 2003) 043005.

[16] R. M. Baltrusaitis, R. Cady, *et al.*, “The Utah Fly’s Eye detector.,” *Nuclear Instruments and Methods in Physics Research A* **240** (1985) 410–428.

[17] R. M. Baltrusaitis, G. L. Cassiday, J. W. Elbert, P. R. Gerhardy, S. Ko, E. C. Loh, Y. Mizumoto, P. Sokolsky, and D. Steck, “Total proton-proton cross section at $s^{\frac{1}{2}} = 30$ tev,” *Phys. Rev. Lett.* **52** (Apr, 1984) 1380–1383.

[18] H. M. J. Barbosa, F. Catalani, J. A. Chinellato, and C. Dobrigkeit, “Determination of the calorimetric energy in extensive air showers,” *Astroparticle Physics* **22** (Nov., 2004) 159–166, `arXiv:astro-ph/0310234`.

[19] N. Barenthien, C. Bethge, K. Daumiller, H. Gemmeke, K.-H. Kampert, and C. Wiebusch, “The Slow Control System of the Auger Fluorescence Detectors,” in *International Cosmic Ray Conference*, vol. 2 of *International Cosmic Ray Conference*, pp. 895–+. July, 2003.

[20] P. R. Barker, W. E. Hazen, and A. Z. Hendel, “Radio pulses from cosmic-ray air showers,” *Phys. Rev. Lett.* **18** (Jan, 1967) 51–54.

[21] D. Barnhill, M. Healy, M. Risse, C. Roucelle, V. Scherini, B. Smith, and C. Wileman, “Search for Ultra-High Energy Photons with the Pierre Auger Observatory,” 30th ICRC, (Merida). 2007, #0602.

[22] P. Bauleo, J. Brack, L. Garrard, J. Harton, R. Knapik, R. Meyhandan, A. C. Rovero, A. Tamashiro, and f. D. Warner, “Absolute calibration of the auger fluorescence detectors,” 2005.

[23] K.-H. Becker, A. Behrmann, E.-M. El-Mechaouri, D. Fuhrmann, H. Geenen, C. Guse, S. Hartmann, K.-H. Kampert, V. Scherini, U. Weisher, and C. Wiebusch, “Photomultiplier tests for the fluorescence detectors of the Pierre Auger Observatory in Wuppertal.” Pierre Auger Collaboration Technical Note. GAP-04-053.

[24] K.-H. Becker *et al.*, “Qualification tests of the 11 000 photomultipliers for the Pierre Auger Observatory fluorescence detectors,” *Nuclear Instruments and Methods in Physics Research A* **576** (June, 2007) 301–311.

[25] J. Bellido, “Measuring the mean X_{max} as a function of the shower energy using the hybrid data.” Pierre Auger Collaboration Technical Note. GAP-07-019.

[26] K. Belov, “p-air inelastic cross-section at ultra-high energies,” in *International Cosmic Ray Conference*, vol. 7 of *International Cosmic Ray Conference*, pp. 343–+. 2005.

[27] K. Belov for the HIRES Collaboration, “A Measurement Technique of p-Air Inelastic Cross-Section above 10^{18} eV,” in *International Cosmic Ray Conference*, vol. 3 of *International Cosmic Ray Conference*, pp. 1567–+. July, 2003.

[28] S. Y. BenZvi, B. M. Connolly, J. A. J. Matthews, M. Prouza, E. F. Visbal, and S. Westerhoff, “Measurement of the Aerosol Phase Function at the Pierre Auger Observatory,” *ArXiv e-prints* **704** (Apr., 2007) `0704.0303`.

[29] V. S. Berezinsky and S. I. Grigor’eva, “A bump in the ultrahigh-energy cosmic ray spectrum,” *Astron. Astrophys.* **199** (1988) 1–12.

[30] H. Bethe and W. Heitler, “On the stopping of fast particles and on the creation of positive electrons,” *Proc. Roy. Soc. Lond.* **A146** (1934) 83–112.

[31] P. Bhattacharjee and G. Sigl, “Origin and propagation of extremely high energy cosmic rays,” *Phys. Rep.* **327** (Mar., 2000) 109–247, `arXiv:astro-ph/9811011`.

[32] D. J. Bird *et al.*, “Evidence for correlated changes in the spectrum and composition of cosmic rays at extremely high energies,” *Phys. Rev. Lett.* **71** (Nov, 1993) 3401–3404.

[33] D. J. Bird *et al.*, “The cosmic-ray energy spectrum observed by the Fly’s Eye,” *Astrophys. J.* **424** (Mar., 1994) 491–502.

[34] D. J. Bird *et al.*, “Detection of a cosmic ray with measured energy well beyond the expected spectral cutoff due to cosmic microwave radiation,” *Astrophys. J.* **441** (Mar., 1995) 144–150, `arXiv:astro-ph/9410067`.

[35] O. Blanch Bigas for the Pierre Auger Collaboration, “Limits to the diffuse flux of uhe tau neutrinos at eev energies from the pierre auger observatory,” `arXiv:0706.1658`.

[36] R. D. Blandford, “Acceleration of Ultra High Energy Cosmic Rays,” *Physica Scripta Volume T* **85** (2000) 191–+, `arXiv:astro-ph/9906026`.

[37] M. M. Block, F. Halzen, and T. Stanev, “Extending the frontiers - reconciling accelerator and cosmic ray p-p cross sections,” *Physical Review D* **62** (2000) 077501.

[38] S. Böser *et al.*, “Feasibility of acoustic neutrino detection in ice: First results from the South Pole Acoustic Test Setup (SPATS),” *ArXiv e-prints* **708** (Aug., 2007) `0708.2089`.

[39] N. M. Budnev for the Baikal Collaboration, “A prototype device for acoustic neutrino detection in lake baikal,” `astro-ph/0710.3113`.

[40] D. V. Camin *et al.*, “Fabrication of the first 150 head electronics units-results of the acceptance tests.” Pierre Auger Collaboration Technical Note. GAP-99-043.

[41] F. Catalani *et al.*, "Statistical methods applied to composition studies of ultrahigh energy cosmic rays," 30th ICRC, (Merida). 2007, #616. `astro-ph/0703582`.

[42] C. H. Christensen, "Principal Component Analysis in ROOT." http://cholm.home.cern.ch/cholm/root/principal/doc/.

[43] R. W. Clay *et al. Pub. Astron. Soc. Aust. 15* **334** (1998).

[44] S. Coleman and S. L. Glashow, "Evading the gzk cosmic-ray cutoff," `hep-ph/9808446`.

[45] J. W. Cronin, T. K. Gaisser, and S. P. Swordy, "Cosmic rays at energy frontier," *Scientific American* (1997).

[46] B. Dawson, "Amplitude Dynamic Range in Auger Fluorescence Electronics." Pierre Auger Collaboration Technical Note. GAP-97-064.

[47] B. Dawson for the Pierre Auger Collaboration, "Hybrid Performance of the Pierre Auger Observatory," *ArXiv e-prints* **706** (June, 2007) `0706.1105`.

[48] A. Donnachie and P. V. Landshoff, "New data and the hard pomeron," *Phys. Lett.* **B518** (2001) 63–71, `hep-ph/0105088`.

[49] J. Ellis, V. E. Mayes, and D. V. Nanopoulos, "Ultrahigh-energy cosmic rays particle spectra from crypton decays," *Phys. Rev. D* **74** (Dec., 2006) 115003–+, `arXiv:astro-ph/0512303`.

[50] R. Engel. Rapporteur talk at 30th ICRC, (Merida), HE 3, July, 2007.

[51] T. Erber, "High-energy electromagnetic conversion processes in intense magnetic fields," *Rev. Mod. Phys.* **38** (Oct, 1966) 626–659.

[52] P. Facal San Luis, "High energy cosmic rays at the auger observatory fluorescence detector," PhD thesis, Santiago de Compostela (Spain), April, 2005.

[53] P. Facal San Luis for the Pierre Auger Collaboration, "Measurement of the UHECR spectrum above 10 EeV at the Pierre Auger Observatory using showers with zenith angles greater than 60 degrees," *ArXiv e-prints* **706** (June, 2007) `0706.4322`.

[54] H. Falcke and P. Gorham, "Detecting radio emission from cosmic ray air showers and neutrinos with a digital radio telescope," *Astroparticle Physics* **19** (July, 2003) 477–494, `arXiv:astro-ph/0207226`.

[55] A. Fassò, A. Ferrari, J. Ranft, and B. E. Sala, "FLUKA: a multi-particle transport code," *CERN-2005-10, INFN/TC_05/11, SLAC-R-773.*

[56] G. J. Feldman and R. D. Cousins, "Unified approach to the classical statistical analysis of small signals," *Phys. Rev. D* **57** (Apr, 1998) 3873–3889.

[57] E. Fermi, "On the origin of the cosmic radiation," *Phys. Rev.* **75** (Apr, 1949) 1169–1174.

[58] B. Fick for the Pierre Auger Collaboration, "The central laser facility at the pierre auger observatory," *JINST* **1** (2006) P11003.

[59] Z. Fodor, S. D. Katz, and A. Ringwald, "Relic neutrino masses and the highest energy cosmic rays," *Journal of High Energy Physics* **6** (June, 2002) 46–+, `arXiv:hep-ph/0203198`.

[60] T. K. Gaisser and A. M. Hillas, "Reliability of the Method of Constant Intensity Cuts for Reconstructing the Average Development of Vertical Showers," vol. 8 of *Proc. 15th ICRC, (Plovdiv)*, p. 353. 1977.

[61] M. Galaverni and G. Sigl, "Lorentz Violation in the Photon Sector and Ultra-High Energy Cosmic Rays," *ArXiv e-prints* `0708.1737`.

[62] H. Geenen, "Reconstructing the primary energy spectrum from fluorescence telescope data of the auger observatory," PhD thesis, Bergische Universität Wuppertal (Germany), oct, 2007.

[63] G. Gelmini, O. Kalashev, and D. V. Semikoz, "GZK Photons as Ultra High Energy Cosmic Rays," *ArXiv Astrophysics e-prints* (June, 2005) `astro-ph/0506128`.

[64] M. Giller, A. Kacperczyk, J. Malinowski, W. Tkaczyk, and G. Wieczorek, "Similarity of extensive air showers with respect to the shower age," *Journal of Physics G Nuclear Physics* **31** (2005) 947–958.

[65] A. V. Glushkov *et al.*, "Constraining the fraction of primary gamma rays at ultra-high energies from the muon data of the Yakutsk extensive-air-shower array," *ArXiv Astrophysics e-prints* (Jan., 2007) `astro-ph/0701245`.

[66] D. S. Gorbunov, G. I. Rubtsov, and S. V. Troitsky, "Towards event-by-event studies of the ultrahigh-energy cosmic-ray composition," *Astroparticle Physics* **28** (Sept., 2007) 28–40, `arXiv:astro-ph/0606442`.

[67] P. W. Gorham, C. L. Hebert, K. M. Liewer, C. J. Naudet, D. Saltzberg, and D. Williams, "Experimental Limit on the Cosmic Diffuse Ultrahigh Energy Neutrino Flux," *Physical Review Letters* **93** (July, 2004) 041101–+, `arXiv:astro-ph/0310232`.

[68] K. Greisen, *Progress in Cosmic-Ray Physics*, vol. 3. Interscience Publishers, Inc., New York, 1956.

[69] K. Greisen, "End to the cosmic-ray spectrum?," *Phys. Rev. Lett.* **16** (Apr, 1966) 748–750.

[70] D. Harari, S. Mollerach, and E. Roulet, "The toes of the ultra high energy cosmic ray spectrum," *Journal of High Energy Physics* **8** (Aug., 1999) 22–+, `arXiv:astro-ph/9906309`.

[71] D. Heck *et al.*, "CORSIKA: A Monte Carlo Code to Simulate Extensive Air Showers," *Report FZKA 6019* (1998).

[72] W. Heitler, *Quantum Theory of Radiation.* Oxford University Press, 1944.

[73] V. Hess, "Über Beobachtungen der durchdringenden Strahlung bei sieben Freiballonfahrten," *Physik. Zeitschr.* **13** (1912) 1084–1091.

[74] A. M. Hillas, "The origin of ultrahigh-energy cosmic rays," *Ann. Rev. Astron. Astrophys.* **22** (1984) 425–444.

[75] A. M. Hillas, "Cosmic Rays: Recent Progress and some Current Questions," *ArXiv Astrophysics e-prints* (July, 2006) `astro-ph/0607109`.

[76] HiRes Collaboration, "A measurement of the average longitudinal development profile of cosmic ray air showers between 10^{17} and 10^{18} eV," *Astroparticle Physics* **16** (2001) 1–11, `astro-ph/0008206`.

[77] HiRes Collaboration, "Shower Longitudinal Development Study with CORSIKA," vol. 2 of *Proc. 27th ICRC (Hamburg)*, p. 490. 2001.

[78] HiRes Collaboration, "Observation of the GZK Cutoff by the HiRes Experiment," *ArXiv Astrophysics e-prints* (Mar., 2007) `astro-ph/0703099`.

[79] J. R. Hoerandel, "Models of the knee in the energy spectrum of cosmic rays," *Astroparticle Physics* **21** (2004) 241.

[80] P. Homola, D. Góra, D. Heck, H. Klages, J. PeĶala, M. Risse, B. Wilczyńska, and H. Wilczyński, "Simulation of ultra-high energy photon propagation in the geomagnetic field," *Computer Physics Communications* **173** (Dec., 2005) 71–90, `arXiv:astro-ph/0311442`.

[81] M. Honda, M. Nagano, *et al.*, "Inelastic cross section for p-air collisions from air shower experiments and total cross section for p-p collisions up to $\sqrt{s} = 24$ TeV," *Phys. Rev. Lett.* **70** (Feb, 1993) 525–528.

[82] T. Huege for the LOPES Collaboration, "Radio detection of cosmic ray air showers with lopes," *BRAZ.J.PHYS.* **36** (2006) 1157.

[83] N. N. Kalmykov and S. S. Ostapchenko, "The nucleus-nucleus interaction, nuclear fragmentation, and fluctuations of extensive air showers," *Physics of Atomic Nuclei* **56** (1993) 346–353.

[84] K. Kamata and J. Nishimura, "The Lateral and the Angular Structure Functions of Electron Showers," vol. 6 of *Progr Theor. Phys. Suppl.*, pp. 93–155. 1958.

[85] K.-H. Kampert. priv. communication.

[86] T. Karg, J. Auffenberg, T. Gaisser, K. Helbing, and A. Karle, "A radio air shower detector as an extension for icecube and icetop," 30th ICRC, (Merida). 2007, #0293.

[87] KASCADE-Grande Collaboration, "Investigating the 2nd knee: The KASCADE-Grande experiment," *ArXiv Astrophysics e-prints* (Aug., 2005) `astro-ph/0508286`.

[88] B. Keilhauer *et al.*, "Impact of varying atmospheric profiles on extensive air shower observation: atmospheric density and primary mass reconstruction," *Astroparticle Physics* **22** (Nov., 2004) 249–261, `arXiv:astro-ph/0405048`.

[89] B. Keilhauer *et al.*, "Impact of varying atmospheric profiles on extensive air shower observation: Fluorescence light emission and energy reconstruction," *Astroparticle Physics* **25** (May, 2006) 259–268, `arXiv:astro-ph/0511153`.

[90] B. Keilhauer for the Auger Collaboration, "Atmospheric profiles at the southern pierre auger observatory and their relevance to air shower measurement," *INDIA* **7** (2005) 123, `arXiv:astro-ph/0507275`.

[91] J. Knapp *et al.*, "Extensive air shower simulations at the highest energies," *Astroparticle Physics* **19** (Apr., 2003) 77–99, `arXiv:astro-ph/0206414`.

[92] W. J. Krzanowski, "Princiles of Multivariare Analysis. A user's Perspective." Oxford statistical science series, 22, 2000. http://books.google.com/.

[93] D. Kuempel, "Geometry Reconstruction of Fluorescence Detectors Revisited," Diploma thesis, Bergische Universität Wuppertal (Germany), 2007.

[94] D. Kuempel, K. . Kampert, and M. Risse, "Geometry reconstruction of fluorescence detectors revisited," *ArXiv e-prints* `0708.3976`.

[95] J. Linsley, "Evidence for a primary cosmic-ray particle with energy 10^{20} ev," *Phys. Rev. Lett.* **10** (Feb, 1963) 146–148.

[96] J. Matthews, "A Heitler model of extensive air showers," *Astroparticle Physics* **22** (Jan., 2005) 387–397.

[97] A. B. Migdal, "Bremsstrahlung and Pair Production in Condensed Media at High Energies," *Physical Review* **103** (Sept., 1956) 1811–1820.

[98] M. Mostafà, "The Hybrid Activities of the Pierre Auger Observatory," *Nucl. Phys. B Proc. Suppl.* **165** (Mar., 2007) 50–58, `astro-ph/0608670`.

[99] M. Mostafà and D. Thomas, "I saw the first *quadriple* event. Cantè pri!." Pierre Auger Collaboration Technical Note. GAP-07-066.

[100] M. Nagano *et al.*, "Energy spectrum of primary cosmic rays between $10^{14.5}$ and 10^{18} eV.," *Journal of Physics G Nuclear Physics* **10** (1984) 1295–1310.

[101] M. Nagano *et al.*, "Energy spectrum of primary cosmic rays above 10^{17} ev determined from extensive air shower experiments at akeno," *Journal of Physics G: Nuclear and Particle Physics* **18** (1992), no. 2, 423–442.

[102] R. Nahnhauer, "Alternative Detection Methods for Highest Energy Neutrinos," *Nuclear Physics B Proceedings Supplements* **143** (June, 2005) 387–394, `arXiv:astro-ph/0411715`.

[103] J. Neyman, "Outline of a Theory of Statistical Estimation Based on the Classical Theory of Probability," *Royal Society of London Philosophical Transactions Series A* **236** (Aug., 1937) 333–380.

[104] N. Nierstenhöfer, "Untersuchung systematischer Rekonstruktionsunsicherheiten der Fluoreszenzdetektoren des Pierre Auger Observatoriums anhand experimenteller Daten," Diploma thesis, Bergische Universität Wuppertal, D, June, 2007.

[105] D. Nitz for the Pierre Auger Collaboration, "The Northern Site of the Pierre Auger Observatory," *ArXiv e-prints* `0706.3940`.

[106] S. Ostapchenko, "QGSJET-II: results for extensive air showers," *ArXiv Astrophysics e-prints* (Dec., 2004) `astro-ph/0412591`.

[107] A. A. Penzias and R. W. Wilson, "A measurement of excess antenna temperature at 4080 mc/s.," *Astrophys. J.* **142** (July, 1965) 419–421.

[108] L. Perrone *et al.*, "Validation of the real and simulated data of the Pierre Auger fluorescence telescopes," `astro-ph/0507486`.

[109] L. Perrone for the Pierre Auger Collaboration, "Auger FD: Detector Response to Simulated Showers and Real Event Topologies," *Nuclear Physics B Proceedings Supplements* **136** (Nov., 2004) 407–414.

[110] L. Perrone for the the Pierre Auger Collaboration, "Measurement of the UHECR energy spectrum from hybrid data of the Pierre Auger Observatory," *ArXiv e-prints* `0706.2643`.

[111] S. Petrera *et al.*, "Fluorescence and hybrid detection aperture of the pierre auger observatory," `astro-ph/0507103`.

[112] Photonis, "Xp-3062, high phr, 8-stage, 40 mmm (1.5") hexagonal tube." product specification - additional specifications. 2001, Photonis.

[113] T. Pierog *et al.*, "Impact of Uncertainties in Hadron Production on Air-Shower Predictions," *ArXiv Astrophysics e-prints* (Feb., 2006) `astro-ph/0602190`.

[114] Pierre Auger Collaboration, "The Pierre Auger Observatory Technical Design Report," 2001.

[115] Pierre Auger Collaboration, "Properties and performance of the prototype instrument for the Pierre Auger Observatory," *Nuclear Instruments and Methods in Physics Research A* **523** (May, 2004) 50–95.

[116] Pierre Auger Collaboration, "Correlation of the highest energy cosmic rays with nearby extragalactic objects," *Science* **318** (2007) 938–943.

[117] Pierre Auger Collaboration, "Measurement of Aerosols at the Pierre Auger Observatory," *ArXiv e-prints* **706** (June, 2007) `0706.3236`.

[118] Pierre Auger Collaboration, "The Absolute, Relative and Multi-Wavelength Calibration of the Pierre Auger Observatory Fluorescence Detectors," *ArXiv e-prints* **708** (Aug., 2007) `0708.1924`.

[119] Pierre Auger Collaboration, "An upper limit to the photon fraction in cosmic rays above 10^19 ev from the pierre auger observatory," *Astropart. Phys.* **27** (2007) 155–168, `astro-ph/0606619`.

[120] Pierre Auger group, Università di Lecce and INFN, Italy.
http://auger.le.infn.it/group.html.

[121] Pierre Auger group, Università di Roma II "Tor Vergata" and INFN, Italy.
http://statistics.roma2.infn.it/ auger/welcome.html.

[122] Pierre Auger group, Università di Torino and INFN, Italy.
http://www.auger.to.infn.it/lidar/.

[123] Pierre Auger group, University of Adelaide, Astralia.
http://www.physics.adelaide.edu.au/astrophysics/pierre.

[124] Pierre Auger Observatory. http://www.auger.org/.

[125] L. Prado Jr. *et al.*, "Simulation of the fluorescence detector of the Pierre Auger Observatory," *Nucl. Instr. Meth.* **A 545** (2005) 632–642.

[126] R. J. Protheroe, "Acceleration and interaction of ultra high energy cosmic rays," in *Topics in Cosmic-Ray Astrophysics*, M. A. Duvernois, ed., pp. 247–+. 1999.

[127] R. J. Protheroe and A. P. Szabo, "High energy cosmic rays from active galactic nuclei," *Phys. Rev. Lett.* **69** (Nov, 1992) 2885–2888.

[128] J. Rautenberg for the Pierre Auger Collaboration, "Online Monitoring of the Pierre Auger Observatory," 30th ICRC, (Merida). 2007, #0717.

[129] M. Risse *et al.*, "Primary particle type of the most energetic fly's eye air shower," *Astroparticle Physics* **21** (2004) 479.

[130] M. Risse *et al.*, "Upper limit on the photon fraction in highest-energy cosmic rays from agasa data," *Physical Review Letters* **95** (2005) 171102.

[131] M. Risse *et al.*, "Photon air showers at ultra-high energy and the photonuclear cross-section," *Czechoslovak Journal of Physics* **56** (2006) A327.

[132] M. Risse and P. Homola, "Search for ultra-high energy photons using air showers," *Mod. Phys. Lett. A* **22** (2007) 749, `astro-ph/0702632`.

[133] M. Roth for the Auger Collaboration, "Measurement of the UHECR energy spectrum using data from the Surface Detector of the Pierre Auger Observatory," *ArXiv e-prints* `0706.2096`.

[134] G. Rubtsov *et al.*, "Upper limit on the ultrahigh-energy photon flux from AGASA and Yakutsk data," *Phys. Rev. D* **73** (Mar., 2006) 063009–+, `arXiv:astro-ph/0601449`.

[135] F. A. Sánchez, "The performance of the fluorescence detector ot the Pierre Auger Observatory for the ultra high energy cosmic rays," PhD thesis, Università degli Studi di Milano, 2006.

[136] V. Scherini, "Performance of the Pierre Auger Fluorescence Detector at the highest energies," Proc. 20th ECRS, (Lisboa). 2006.

[137] V. Scherini, H. Geenen, K.-H. Kampert, L. Perrone, and S. Robbins, "Study of the FD saturation region and influence of the virtual channel gain settings." Pierre Auger Collaboration Technical Note. GAP-05-110.

[138] V. Scherini, H. Geenen, K.-H. Kampert, L. Perrone, and S. Robbins, "The Virtual Channel Reloaded." Pierre Auger Collaboration Technical Note. GAP-06-104.

[139] V. Scherini, F. Schüssler, R. Engel, K.-H. Kampert, M. Risse, and M. Unger, "Simulation study of shower profiles from ultra-high energy cosmic rays," 30th ICRC, (Merida). 2007, #561.

[140] M. Settimo, L. Perrone, and I. De Mitri, "Performance of a hybrid simulation/reconstruction chain at low energy: quality cuts, resolutions and impact on detector aperture." Pierre Auger Collaboration Technical Note. GAP-06-105.

[141] K. Shinozaki *et al.*, "Upper limit on gamma-ray flux above 10^{19} ev estimated by the akeno giant air shower array experiment," *Astrophys. J.* **571** (June, 2002) L117–L120.

[142] P. Sommers, "Capabilities of a giant hybrid air shower detector," *Astroparticle Physics* **3** (Aug., 1995) 349–360.

[143] C. Song, Z. Cao, B. R. Dawson, B. E. Fick, P. Sokolsky, and X. Zhang, "Energy estimation of UHE cosmic rays using the atmospheric fluorescence technique," *Astroparticle Physics* **14** (2000) 7–13, `astro-ph/9910195`.

[144] F. W. Stecker, C. Done, M. H. Salamon, and P. Sommers, "High-energy neutrinos from active galactic nuclei," *Phys. Rev. Lett.* **66** (May, 1991) 2697–2700.

[145] T. Suomijarvi for the Pierre Auger Collaboration, "Performance of the Pierre Auger Observatory Surface Detector," *ArXiv e-prints* **709** (Sept., 2007) `0709.1823`.

[146] M. Takeda *et al.*, "Energy determination in the akeno giant air shower array experiment," *Astroparticle Physics* **19** (2003) 447.

[147] M. Teshima *et al.*, "Telescope array for advanced studies of cosmic rays at the highest and TEV energies," *Nuclear Physics B Proceedings Supplements* **28** (Nov., 1992) 169–175.

[148] The Auger Observer. http://augerobserver.fzk.de.

[149] The Pierre Auger Collaboration, "Anisotropy studies around the galactic centre at EeV energies with the Auger Observatory," *ArXiv Astrophysics e-prints* (July, 2006) `astro-ph/0607382`.

[150] R. Ulrich, J. Blümer, R. Engel, F. Schüssler, and M. Unger, "On the relation between the proton-air cross section and fluctuations of the shower longitudinal profile," *ArXiv e-prints* `0706.2086`.

[151] R. Ulrich, J. Blümer, R. Engel, F. Schüssler, and M. Unger, "On the measurement of the proton-air cross section using longitudinal shower profiles," *ArXiv Astrophysics e-prints* (Dec., 2006) `astro-ph/0612205`.

[152] M. Unger, "Measurement of $<X_{max}>$ as a function of energy." Pierre Auger Collaboration Technical Note. GAP-07-005.

[153] M. Unger, R. Engel, F. Schüssler, and R. Ulrich, "Longitudinal Shower Profile Reconstruction from Fluorescence and Cherenkov Light," *ArXiv e-prints* `0706.1501`.

[154] M. Unger *et al.*, "Study of the Cosmic Ray Composition above 0.4 EeV using the Longitudinal Profiles of Showers observed at the Pierre Auger Observatory," *ArXiv e-prints* `0706.1495`.

[155] A. M. van den Berg for the Pierre Auger Collaboration, "Radio detection of high-energy cosmic rays at the Pierre Auger Observatory," *ArXiv e-prints* `0708.1709`.

[156] V. Verzi for the Pierre Auger Collaboration, "The Fluorescence Detector of the Pierre Auger Observatory," *Nuclear Physics B Proceedings Supplements* **165** (Mar., 2007) 37–44.

[157] W. Wagner for the AMANDA collaboration, "New capabilities of the amanda-ii high energy neutrino detector," vol. 2 of *Proc. 28th ICRC, (Tzukuba)*, pp. 1365–1368. 2003.

[158] E. Waxman and J. Miralda-Escude, "Images of Bursting Sources of High-Energy Cosmic Rays: Effects of Magnetic Fields," *Astrophys. J.* **472** (Dec., 1996) L89+, `arXiv:astro-ph/9607059`.

[159] E. Waxman and J. Bahcall, "High energy neutrinos from cosmological gamma-ray burst fireballs," *Phys. Rev. Lett.* **78** (Mar, 1997) 2292–2295.

[160] L. Wiencke for the Pierre Auger collaboration, "Extracting first science measurements from the southern detector of the pierre auger observatory," *Nucl. Instrum. Meth.* **A572** (2007) 508–510, `astro-ph/0607449`.

[161] T. Yamamoto for the Pierre Auger Collaboration, "The UHECR spectrum measured at the Pierre Auger Observatory and its astrophysical implications," *ArXiv e-prints* `0707.2638`.

[162] G. T. Zatsepin and V. A. Kuz'min, "Upper limit of the cosmic-ray spectrum," *Zh. Eksp. Teor. Fiz., Pis'ma Red.* **4** (1966), no. 3, 114–17.

Acknowledgement

First of all I want to thank Prof. K.-H. Kampert who gave me the opportunity to work in this exciting experiment with the support of a large and active group. A particular mention is reserved to Markus Risse who brought me new ideas and gave me advices. Special thanks to Mariangela Settimo and Lorenzo Perrone from the Auger Lecce group for the joint effort, suggestions and help. For fruitful discussions and cooperation I want to thank the groups in Adelaide, Karlsruhe, L'Aquila, Milano, Roma and Torino.

Thanks to all the members of the Pierre Auger Collaboration and to the technical and amministrative staff down there in Malargüe. Thanks to all my colleagues of Ebene-11 especially the heroes of bzflag and my room mates for sharing the pains and the joys of this work. A grateful thought goes to Frau Schaarwächter for kindness and constant support. A special thank goes to Daniel Camin who introduced me to the Pierre Auger Observatory. This story began inside the huts of KASCADE-Grande and I want to thank Andrea Chiavassa, Piera Ghia and Gianni Navarra.

Thanks to my family, especially to the little one who has joined us lately
thanks to all the people who helped me every day
even just with a word or a thought
and finally thanks to the dawn today

Hiermit versichere ich, dass ich diese Arbeit nur unter Zuhilfenahme der angegebenen Quellen und Hilfsmittel selbständig angefertigt habe.

Wuppertal, October 2007 Viviana Scherini